STUDIES OF LASER INDUCED BREAKDOWN PHENOMENA

IN

LIQUID WATER

by

PETER A. BARNES

B.A.Sc., University of Waterloo, 1963
M.Sc., University of Waterloo, 1964

A DISSERTATION SUBMITTED IN PARTIAL FULFILLMENT
OF THE REQUIREMENTS FOR THE DEGREE OF
DOCTOR OF PHILOSOPHY

in the Department

of

Physics

SIMON FRASER UNIVERSITY
November 1969

APPROVAL

Name: Peter Alexander Barnes

Degree: Doctor of Philosophy

Title of Thesis: Studies of Laser Induced Breakdown Phenomena In Liquid Water

Examining Committee:

K. E. Rieckhoff
Senior Supervisor

R. H. Enns
Examining Committee

J. C. Irwin
Examining Committee

A. J. Alcock
External Examiner
Associate Research Officer
Laser & Plasma Physics Section
Division of Pure Physics
National Research Council of Canada
Ottawa, Ontario

Nov 14/69

ABSTRACT

This thesis describes some of the gross features of the dielectric breakdown which can occur when the intense radiation of a Q-switched ruby laser is focused into water.

A complete description of the passively Q-switched, mode selected ruby laser used in this experimental study is presented. The laser was capable of delivering powers up to 90 MegaWatts in a single longitudinal mode with a beam divergence of less than 1 milliradian. Further mode selection allowed for operation in the lowest order transverse mode.

In order to obtain reproducible and predictable data, it was necessary to cleanse the water samples studied of all suspended particulate matter. A closed-cycle filtering system capable of removing particles as small as 10^{-6} cm is described.

The breakdown threshold power in water was found to be $(5 \pm 4) \times 10^{11}$ Watts/cm^2. Stimulated Brillouin scattering with its lower threshold power than the breakdown threshold, always accompanied the breakdown process. As much as 50% of the incident laser power was converted to the first Stokes stimulated Brillouin wave.

Time integrated photographs indicated the breakdown region to be composed of individual breakdown plasmas separated by approximately 0.4mm and spread along the direction of

propagation over a region of 5 to 10mm. A model involving the introduction of spherical aberration into the focal plane by the focusing lens appears to adequately describe this phenomenon.

Measurements of the scattering characteristics, spectrum, and surface temperature of the breakdown region are presented. It is shown that the scattering behaviour of laser induced breakdown underwater, reflects the character of the shock wave accompanying breakdown and not the breakdown plasma. The breakdown plasma revealed a black body like spectrum with a temperature of 15,000°K. Shock velocities exceeding 10^6cm/sec were produced leading to pressures approaching 10^6 bars.

TABLE OF CONTENTS

LIST OF TABLES

LIST OF ILLUSTRATIONS

ACKNOWLEDGEMENTS

The research reported in this thesis was supervised by Dr. K. E. Rieckhoff, who provided a well equipped laboratory in which to work, for which I am grateful. I have profited greatly, during the course of my work and the writing of this thesis, from discussions with Dr. J. C. Irwin and Dr. R. H. Enns, and I am grateful for their assistance. Many thanks are due also to my external examiner, Dr. A. J. Alcock of the National Research Council of Canada who undertook the arduous task of reading the final manuscript and who made many useful comments.

Several colleagues in the Physics Department and Science Workshop have helped considerably. In particular Drs. J. F. O'Hanlon, J. G. McCallum and J. Conradi, and Messrs. K. R. Lyall, A. A. Fife, D. J. McMillin, and F. Wick.

I am grateful to Mr. D. J. McMillin who transformed my crude sketches to the excellent drawings appearing in this thesis, and to Miss Lynda Bale who cheerfully typed several revised versions of this thesis.

Finally I thank my wife Patsie for her editorial help with the early drafts of this thesis, and, more important her patience and understanding during the entire period of study devoted to this thesis.

The research reported here was financed by the Defense Research Board of Canada. The financial support of the National Research Council of Canada in the form of studentships for the years 1965-66, 1966-67 and 1967-68 is gratefully acknowledged.

CHAPTER 1

INTRODUCTION

1-1 Historical Perspective

Dielectric breakdown and the subsequent plasma formation in optically transparent materials was one of the first and most extensively studied areas of the interaction of intense, Q-switched laser radiation with matter. The first observation of laser induced breakdown occurred in a gas (air) and was reported in 1963[1]. A profuse number of experiments followed this initial observation. (See for example the excellent review article by Raizer[2]).

Early attempts to explain the laser-induced breakdown of gases were based on the effects of the radiation field on individual gas atoms. Gold and Bebb[3] developed a theory of multiphoton absorption leading consequently to ionization, but detailed calculation[4] indicated that this process could not provide a sufficient number of electrons at the power levels involved.

Meyerand and Haught[5] suggested inverse bremsstrahlung (the absorption of a photon by an electron in the neighbourhood of an atom or ion) as a possible mechanism. Wright[6] and Browne[7] treated the breakdown mechanism theoretically as an electron cascade originating in the inverse bremsstrahlung

process. Browne[7] showed that the gas atoms in the focal volume would be completely ionized via this process in times much less than the duration of the laser pulse, while Tozer[8] concluded from a probabilistic model that multiphoton ionization could account for the initiating few electrons.

This area of study has yet to be fully understood. Breakdown studies in gases are persued vigorously at the National Research Council, Ottawa where newly observed effects such as self-focusing occurring during breakdown in air[9] and breakdown generated with a single picosecond pulse[10] have still to be adequately explained.

Laser induced breakdown in transparent solids has received far less study, due in part to the destructive nature of the breakdown process. Hercher[11] reported dielectric breakdown and the resulting fracture in glasses irradiated with a Q-switched ruby laser. Breakdown has also been reported, in the case where a non Q-switched (pulsed) ruby laser was the source of radiation[12]. In this case the peak power is small but the total energy in the pulse is large and sufficient energy to cause mechanical damage may be absorbed in the focal volume as a consequence of residual linear absorption of the medium[12].

For a Q-switched laser pulse, the peak power is many orders of magnitude higher while the total energy in the pulse is usually very much smaller than the pulsed case and the residual linear absorption is too small to account for the

energy removed from the laser beam. Sharma[13,14] has shown that dielectric breakdown in this case originates in multiphoton absorption which induces a photoconductivity releasing electrons which are accelerated in the field of the laser leading to a fully developed electronic cascade in a few nanoseconds. A very complete study related to the initiation processes leading to irreversible damage in several transparent glasses when they are irradiated with a Q-switched ruby laser may be found in Sharma's dissertation[13].

Dielectric breakdown induced in liquids using a Q-switched laser has received very little attention. In fact breakdown in liquids is usually given only passing mention as a "nuisance" phenomena occurring while trying to measure other nonlinear optical properties of the liquids such as Stimulated Brillouin scattering[15].

The only work appearing to date regarding specific measurements of the breakdown phenomena in liquids has been related to the shock wave resulting from the cavitation accompanying breakdown. Bell and Landt[16] report that shock velocities leading to pressures greater than 250kbars occurred during the first 300 nsec following the onset of breakdown. Carome and coworkers have performed preliminary experiments which measure the frequency components of the intense acoustic waves[17], and shadow graph studies[18] of the expanding shock wave at times greater than 3μsec after the initiation of breakdown.

Barnes and Rieckhoff[19] have reported preliminary results regarding the radiation flux density, the spectrum, and the temporal behaviour of the laser induced underwater breakdown plasma.

1-2 Scope of this study

Theories describing the initiation process leading to breakdown in gases have only been successful in describing breakdown in the noble (monatomic) gases at low pressures. Under these conditions the assumption that the radiation field interacts with the gas atoms on an individual basis is valid, and the ideal gas law can be used for the equation of state.

By comparison the processes occurring during the ionization of water are extremely complex. Ionization induced in water vapour using electron beam excitation indicates the presence of at least seven species of ions as well as electrons[20]. Further, in the liquid state, water molecules interact strongly and the breakdown initiation process involves dissociation, ionization and a change of phase. Thus the discussion to follow does not consider the initiation process leading to laser induced breakdown in water, due to its complexity. Instead we direct our attention to the properties of the breakdown plasma following the initial formation period.

During the early stages of this study it was determined that it was difficult to obtain reproducible data pertaining

to laser induced breakdown phenomena in water. The problem stemmed from two sources: (1) instrumentation involving the mode structure of the laser and the detection techniques used to record results and (2) problems related to a lack of reproducible water samples due to microscopic, suspended particulate matter which occurs in all liquids.

Consequently this thesis has two aims. Firstly, a complete description is given of the experimental techniques used. This includes the design and operating characteristics of the single mode laser together with accurate measurement techniques, and the methods used to cleanse the liquids of foreign material. Secondly, the characteristics of the laser induced underwater breakdown are discussed.

The design and operating characteristics of a single frequency Q-switched ruby laser are presented in Chapter 2 and Appendix A. In Appendices B and C we present the techniques used to accurately attenuate and detect the laser beam and the plasma radiation.

The preparation of liquids cleansed of suspended particulate matter is described in Chapter 3.

Chapters 4 and 5 describe the laser induced underwater breakdown plasma and where possible compare it to the more clearly understood breakdown plasma occurring in air.

Finally, in Chapter 6, we summarize the results of this

thesis and offer suggestions for further work related to the laser induced underwater spark.

CHAPTER 2

SINGLE FREQUENCY PASSIVELY Q-SWITCHED RUBY LASER

2-1 Introduction

In this chapter a description of the passively Q-switched ruby laser used in this experimental study is presented. The pertinent wave theory of the laser resonant cavity is considered[21]. This theory is restricted to the plane-parallel and plano-concave[22,23] resonant cavities with circular mirrors and apertures. The techniques of longitudinal and spatial mode selection of these two resonant cavity configurations are discussed. Pumping schemes using linear lamps to excite the ruby cylinder are described. Finally the measured parameters of the laser are presented and compared with the theoretical derivations.

Derivations of the theoretical results presented below appear in Appendix A. We draw freely from Appendix A in the following discussion.

2-2 Description of Laser - Gross Features

If accurate comparisons between experimental results and theoretical calculations are desired in non-linear optical experiments, a single frequency laser is required. The laser frequencies are discussed in terms of longitudinal and spatial modes. A longitudinal mode refers to the standing wave distribution along the resonator axis between the resonator mirrors.

A spatial mode refers to the electromagnetic field distribution across the output mirror.

Hercher described a simple Q-switched ruby laser which operated in a single longitudinal cavity mode using a cryptocyanine dye-cell resonant reflector combination to select the single longitudinal cavity mode[24]. To further refine the laser to select a single spatial mode requires the use of apertures within the resonant cavity[25]. It is the purpose of this section to define the various terms used and to describe the single frequency selection techniques.

To obtain the desired mode selection, two resonant cavities have proven useful. In one cavity the high reflectivity mirror was a dielectric-coated 99% reflectivity spherical mirror with a 10m radius of curvature located approximately 1m behind the output mirror. The other cavity was similar to the first except the dielectric mirror was replaced with a high quality Brewster angle input face roof prism and the output mirror was only 40 cm in front of the prism. Details of the resonant cavity layout are shown schematically in Fig. (2-1). The pumping cavity was in both cases located such that the ruby was 25 cm from the high reflectivity mirror with the Q-switching dye cell (cryptocyanine in methanol) located 15 cm behind the ruby on the high reflectivity mirror side of the pumping cavity. The output mirror was a resonant reflector composed of 1 or 2 glass or sapphire optical flats. A small

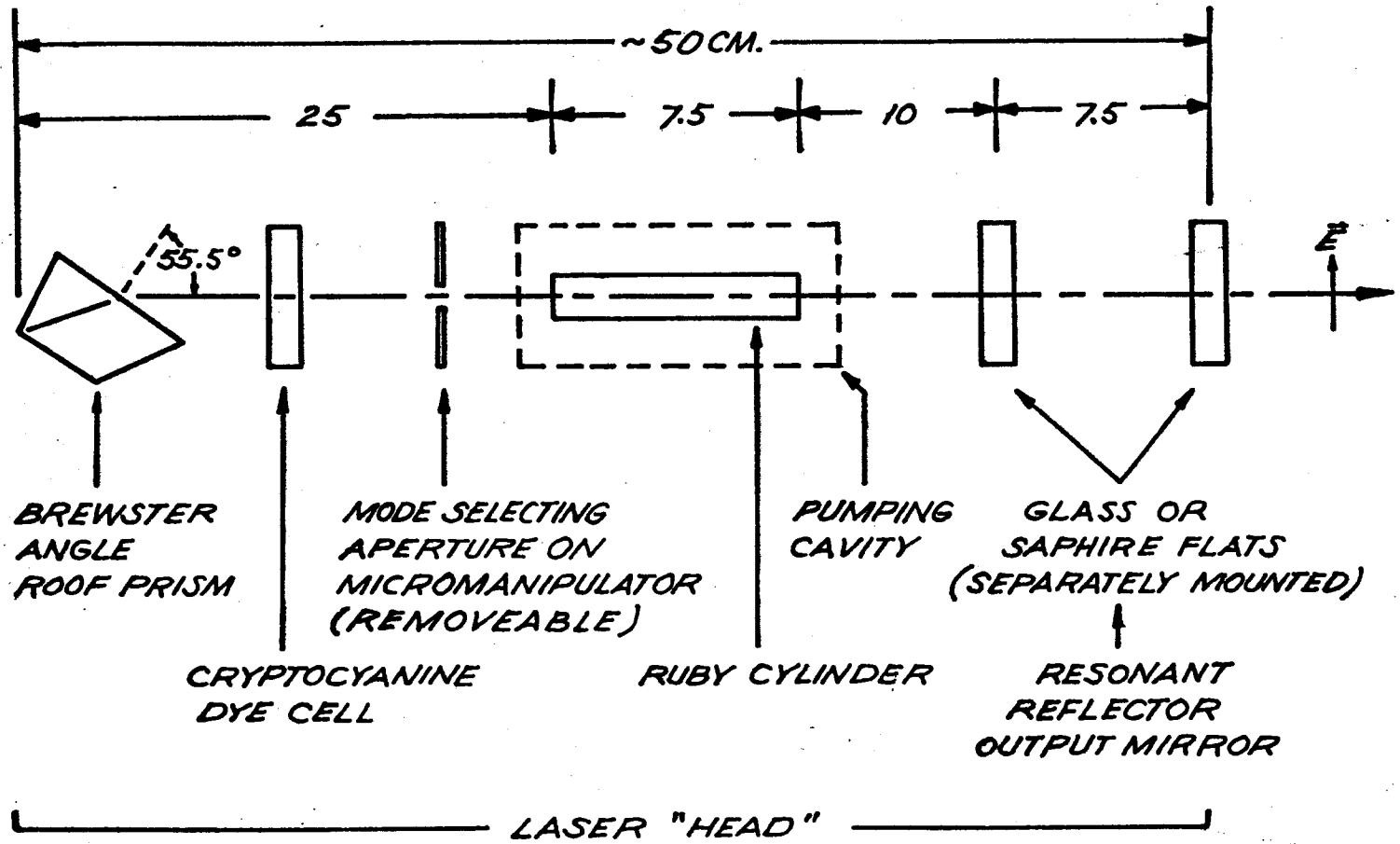

FIG (2-1) LAYOUT OF LASER OPTICAL RESONATOR.

circular aperture placed between the ruby and the dye-cell Q-switch introduced transverse mode selection when desired.

2-3 Ruby Quality

The ruby used was a production quality Linde 76mm x 9.5mm diameter, sand blasted exterior flat-flat cylindrical rod with the C-axis oriented at 60° to the cylinder axis. The Cr^{+3} concentration was 0.05% by weight and the cylinder faces were flat to 1/10 wave and parallel to 2 arc seconds. The ruby faces were AR coated. Static divergence tests[26] were performed on the ruby with a Spectra-Physics Model 115 He-Ne gas laser operating at 632.8nm in the TEM_{ooq} mode to determine the ruby optical quality. Observations were made of the far field patterns of the gas laser beam transmitted through the ruby. Photographs were taken in the intermediate field of both the Ne-Ne laser beam alone and the beam transmitted through the laser rod. Neutral density filters were inserted into the beam to show the variation of radiant intensity with angle.

It was apparent from these photographs that the ruby introduced a detectable but very small amount of distortion to the gas laser beam and a negligible reduction in the peak radiance. Bortfield et al[26] have shown that such static optical quality is a determining factor in dynamic beam divergence, radiance, and energy extraction, from mode selected ruby lasers. For example Union Carbide rates laser rods as Select

Grade if after passing through the laser rod 80% of the gas laser energy is contained within 0.1 mr per inch of rod length.

2-4 Pumping Cavity and Lamp Driver Circuit

The ruby was pumped by two linear PEK XE15-2172-2 flash-lamps with a 75mm arc length and 10mm arc diameter.

The lamps were approximately impedance matched to a 4 stage pulse forming network so that a rectangular light pulse of about 600μsec duration pumped the ruby cylinder. The pulse forming network used to drive the lamps is shown in Fig. (2-2) together with a typical light pulse, measured with a suitably attenuated 929 vacuum photodiode preceded by 2 cm of saturated $CuSO_4$ solution. The lamps were triggered with a 15 kilovolt pulse applied to the metal pumping cavity wall. The trigger pulse appears as the lower trace in Fig.(2-2).

Two pumping cavities were used. Early in this study an Optics Technology Model 130 Laser pumping cavity was used in which the lamps and ruby were placed in the so-called close coupling configuration in which the two lamps and the ruby lie in close proximity to one another as shown in Fig. (2-3a). The reflectivity of the pumping cavity walls has little importance in this configuration. Later a double cylinder pumping cavity was adopted with the flashlamps located at the focal positions and the ruby located at the common centre of this double arrangement as in Fig. (2-3b). If the ruby was removed,

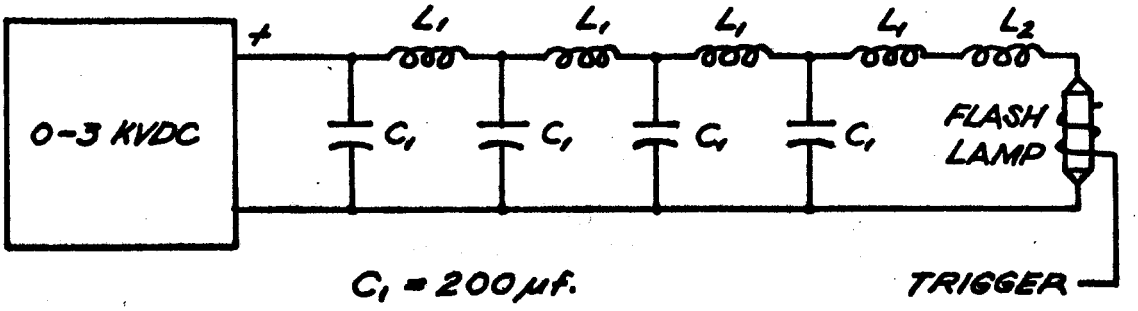

$C_1 = 200\,\mu f.$

$L_1 = 15\,\mu h.$

$L_2 = 60\,\mu h.$ (CIRCUIT INDUCTANCE)

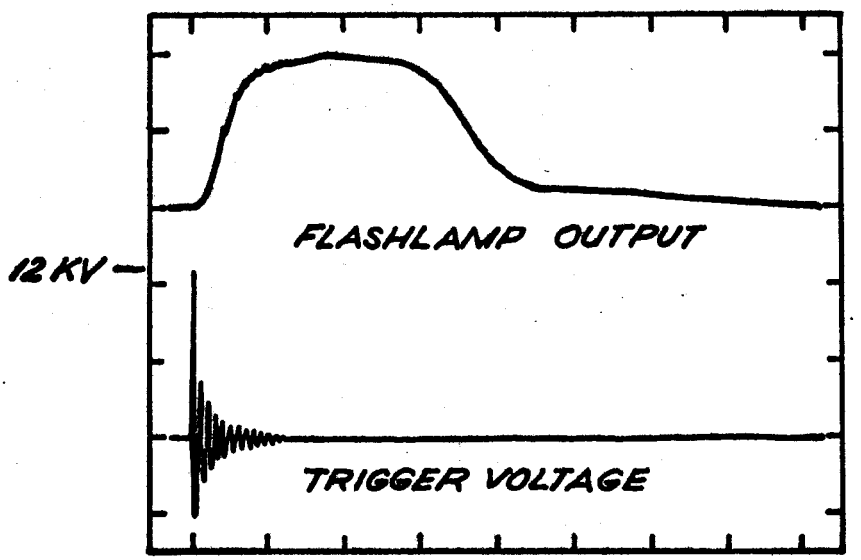

FIG(2.2) PULSE FORMING NETWORK AND RESULTING LIGHT PULSE.

a) CLOSE COUPLING GEOMETRY

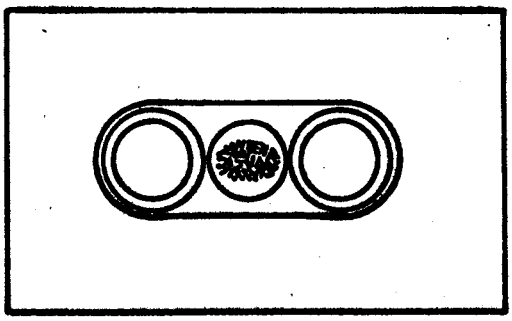

b) DOUBLE CYLINDER GEOMETRY

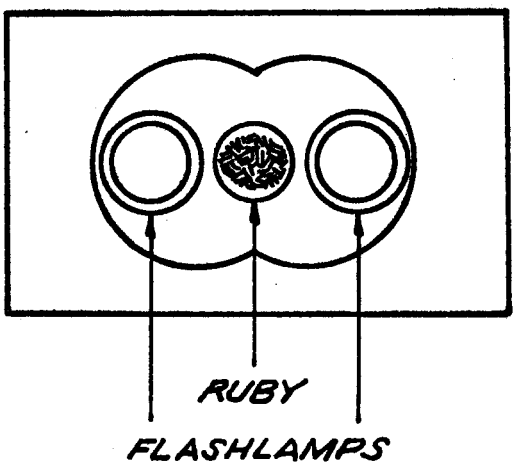

SHADING SHOWS FLUORESCING REGION

SCALE FULL SIZE

FIG(2.3) PUMPING GEOMETRY AND RESULTING RUBY FLUORESCENCE.

a single image of the two lamps was seen reflected from the pumping cavity into the position previously occupied by the ruby. The c-axis of the ruby was aligned in the same plane as that containing the flash lamps. Fluorescence photographs of the ruby with a 5 cm focal length lens stopped down to f/100 indicated that the double-cylinder cavity illuminated the ruby much more uniformly than the close coupling cavity. The shape of the fluorescence in the ruby is shown in Fig. (2-3) by the shaded area on the ruby cross-section. The technique of photographing the fluorescing ruby is described by Lampis et al[27].

2-5 Longitudinal Mode Selection and Laser Alignment

It was first shown theoretically by Sooy[28], that a passive Q-switch with some form of mode selection was preferable to an active Q-switch for production of a narrow line width with Q-switched ruby lasers. This effect had been noted experimentally by McClung and Weiner[29]. It was explained as being due to the basic difference in the operating characteristic of the two types of switches, the passive type (slow switch) taking several hundred complete transits of the cavity to open compared with several tens for a spinning mirror, Kerr cell or Pockels cell (fast "active" switch).

Sooy[28] has shown that to achieve a factor of 10 suppression of one longitudinal mode relative to another in an active type switch, requires a factor of 1.07 between the loss terms per transit.

However for a passive switch the required factor drops to 1.0032 which is obviously easier to attain experimentally.

Shortly after the publication of Sooy's calculations Hercher[24] published results claiming a linewidth of less than 60MHz (.001Å) and peak powers of about 5MW with a multi-plate reflector of simple design. The reflector consisted of two thin (1.7mm) flint glass plates (Schott SF6) of high refractive index, ($n \sim 1.79$) with an air spacing of about 25mm. The exact maximum possible reflectance given by such a system can be calculated from the formula[30]

$$R_{max} = \left\{ \left[1 - \left(\tfrac{1}{n}\right)^{2N} \right] \Big/ \left[1 + \left(\tfrac{1}{n}\right)^{2N} \right] \right\}^2 \qquad (2\text{-}1)$$

where $N = 2$ is the number of plates. For Hercher's resonant reflector this leads to $R_{max} \sim 0.67$. It should be pointed out however that this maximum reflectivity requires that the end plates be either identical or differ by an exact number of half-wavelengths in thickness. If one plate is $\lambda/4$ greater than the other, the peak reflectance drops to $R \sim 0.48$[31].

The exact treatment of resonant reflectors has been discussed in considerable detail by Watts[31]. However, if the spacing between the plates is much greater than the thickness of the plates, an approximate result calculated from simple interference theory can be used, provided the $\lambda/4$ condition mentioned above does not occur.

The resonant reflector used in this study consisted of two 9.5mm thick borosilicate glass flats with a refractive index $n \sim 1.5$. The flats were parallel to 2 arc seconds and flat to $\lambda/10$ over a 20 mm aperture. The spacing between the inside surfaces of the flats was approximately 75mm. The flats were mounted separately in individual mirror mounts (see Fig. (2-1)).

The resonance condition for plane waves travelling perpendicular between plates separated by distance h is that in one round trip an integral number of wavelengths fit into the distance 2nh to yield constructive interference i.e. $2nh = p\lambda$, p being very large and integral. If we increase the wavelength by $\Delta\lambda$ until constructive interference occurs again, p will be reduced to $(p - 1)$[30], i.e. $2nh = (p - 1)(\lambda + \Delta\lambda)$ or $\Delta\lambda = \lambda/(p - 1)$. Thus if $(p - 1) \approx p$ we find the resonance condition is given approximately by

$$\Delta\lambda \simeq \frac{\lambda^2}{2nh} \qquad\qquad \Delta\nu \simeq \frac{c}{2nh}$$

Thus, the resonance condition for the glass plates ($2nh = 2.85$cm) is $\Delta\nu = 10.5$GHz ($\Delta\lambda = 0.17$Å) and between the inner surfaces ($2h = 15$cm) $\Delta\nu = 2$GHz ($\Delta\lambda = 0.032$Å).

The maximum possible reflectivity for our resonant reflector is calculated using Eq.(2-1) to be $R_{max} \sim 0.45$. A schematic sketch of these results is shown in Fig.(2-4). In this same Figure the ruby laser fluorescent line width at 300°K

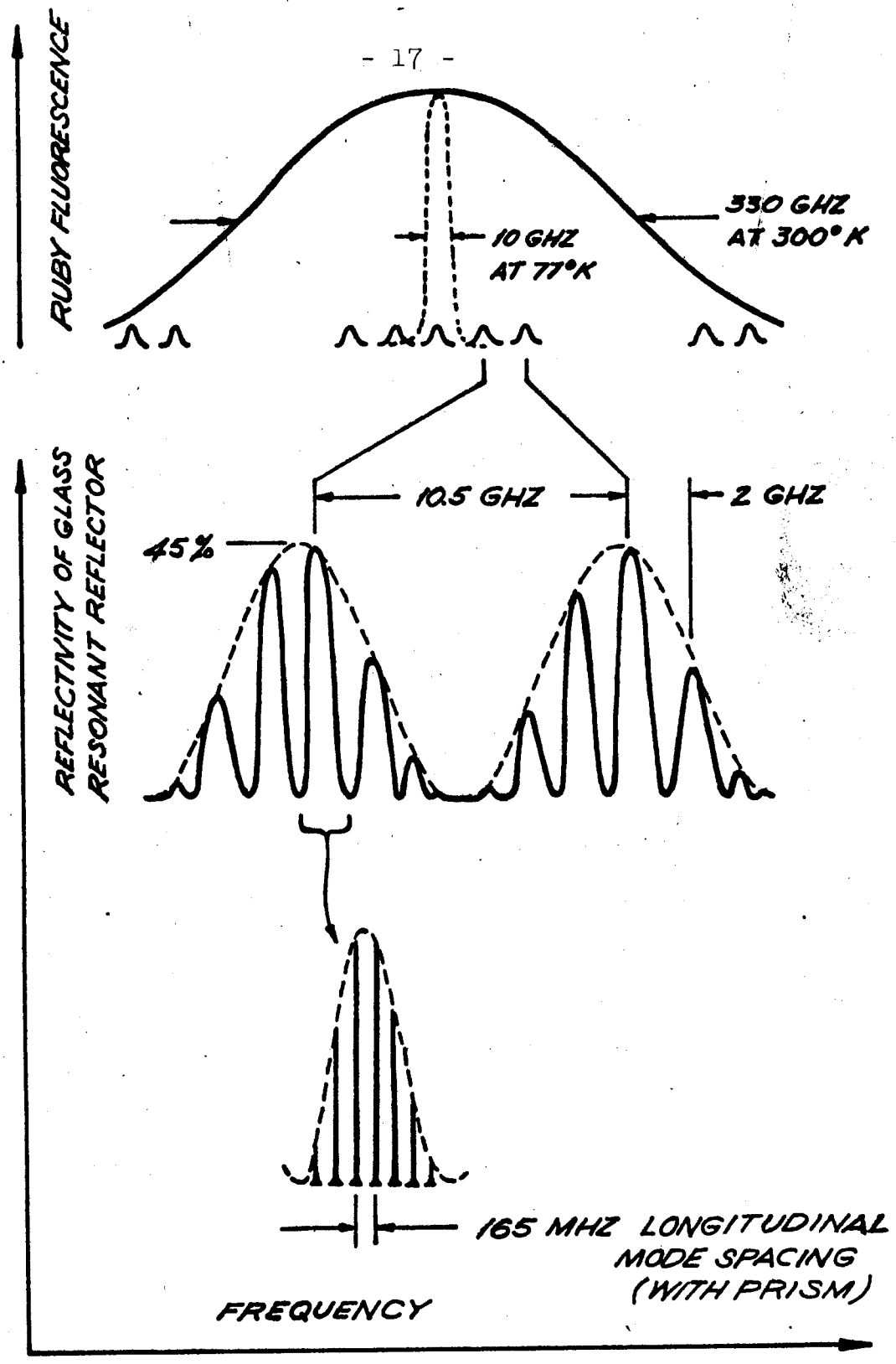

FIG(2.4) RUBY FLUORESCENT LINEWIDTH AND ALLOWED MODES OF RESONANT REFLECTOR.

is shown, together with a schematic representation of the laser axial modes. As shown in the Figure there are about 30 resonator peaks fitted under the laser fluorescence line at room temperature. The fine structure within the resonator peaks (due to the air space) is shown on an expanded scale. The bandwidth of this fine structure is determined from the finesse of the resonator ($F \approx 1$ or 2) to be about 1000 MHz and thus only about 6 laser axial modes ($\Delta\nu_L$ = 165MHz) will fit within a given peak. The laser axial mode spacing was determined by the actual resonator length of approximately 40 cm in air which yields an optical length, $d_{opt} = d_o + d_L(n_L - 1)$ where d_o is the resonator length in air, d_L the length of the ruby rod and n_L(= 1.76) the index of refraction of the ruby rod. Note that when using a prism reflector the spacing between longitudinal modes is $c/4L$. That is, the mode spacing is one-half the value it would be if a dielectric mirror was substituted for the prism. This can easily be seen by tracing a ray through the laser cavity and realizing that the ray must return upon reflection to its point of origin. Since the gain is greatest near the centre of the fluorescent line width, it is obvious that approximately 1 or 2 modes reflected by the reflector maximum closest to this peak in the ruby gain will be the first to achieve threshold in the stimulated emission process. Hence these high gain modes will bleach the dye cell first which will further select the highest gain mode of the few reaching threshold.

Thus, provided the laser rod is not pumped too hard a single axial mode should be produced. This is indeed the case provided the pump energy does not exceed 1.3x threshold.

The passive Q-switch was cryptocyanine dissolved in methanol and placed in a pyrex 1mm path length Opticell. The cell was not AR-coated. The low intensity absorption of the stock solution was adjusted to approximately 40% transmission at 694.3nm in a Cary 14 spectrometer. This relatively high absorption was required to ensure single mode operation. When a 1cm path length cell was used and adjusted to the same 40% transmission, stimulated Brillouin scattering occurred in the methanol and the output pulse was badly distorted and multiple frequencies occurred. Similar observations were reported by Bjorkholm and Stolen[25].

The alignment of the resonant cavity and the components within it was found to be critical if stable single mode operation was desired. The alignment technique used is that of Rothrock and Wilder[32], the theory of which was described by Bergman and Thomson[33]. The procedure is shown schematically in Fig. (2-5) and proceeds as follows. A gas laser is placed approximately 2 meters or more away from the laser head and directed toward it through a 2mm hole in a screen. (The lens L in Fig.(2-5) is not in place at this time). The rear reflector M1 is then placed in position and manipulated until the returned beam covers the 2mm hole in the screen

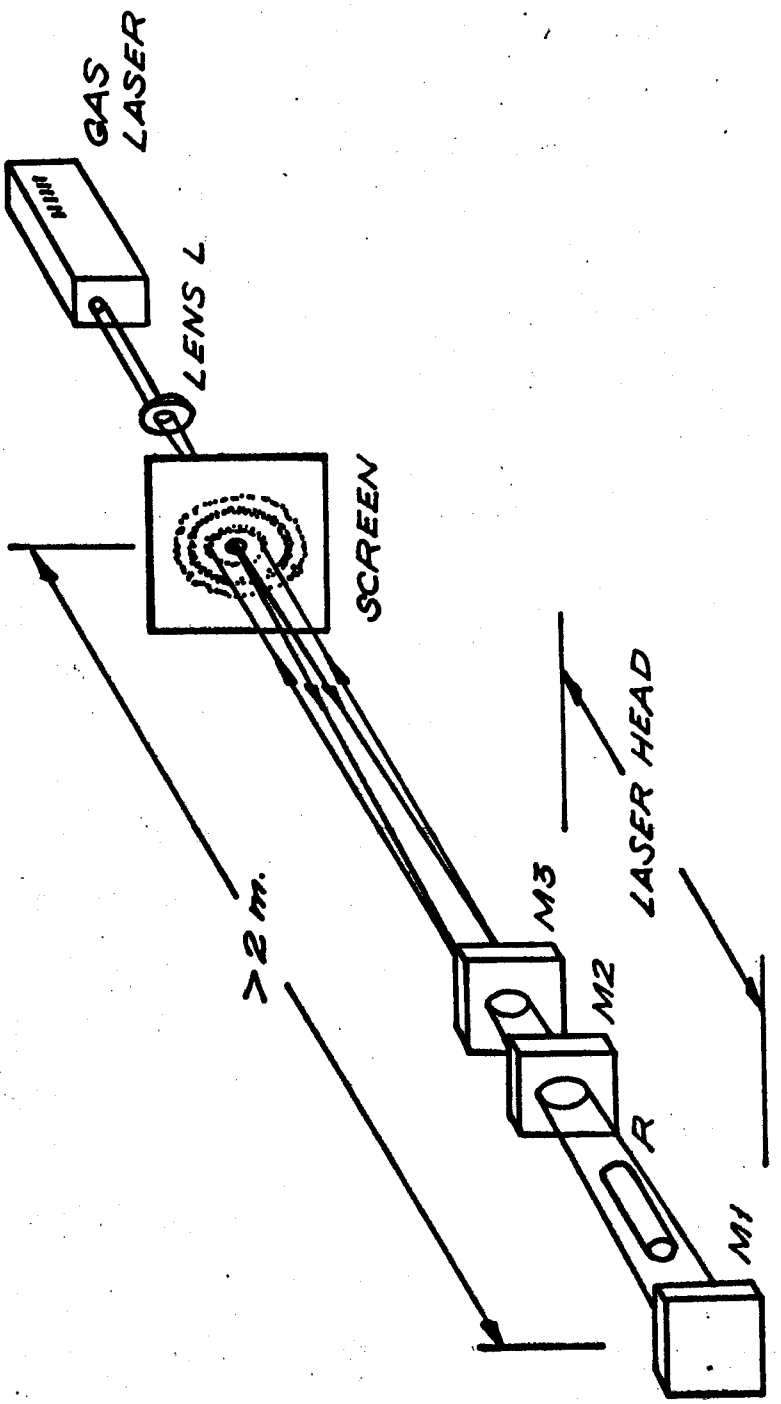

FIG(2.5) LASER HEAD ALIGNMENT.

symmetrically. Then the ruby R in its pumping cavity is mounted and with the back mirror covered the very faint spots reflected from the two ruby surfaces are superimposed on the 2mm hole.

Next one optical flat M2 is mounted and aligned. At this point the lens L is inserted. Its purpose it to diverge the beam to approximately a 2cm dia at the output mirror. A faint ring system displaced from the centre of the screen should be observed. The mirror M2 is now gently adjusted to centre this ring system, due to the ruby and the optical flat, on the screen. Now the back mirror M1 is uncovered and a very sharp system of closely spaced rings will appear due to the two mirrors. The back mirror M1 (prism) is now adjusted to centre this ring system. Two ring systems are now centred on the screen. Finally the second optical flat M3 is mounted and roughly aligned with the lens L removed and an opaque screen added between the ruby and the first flat. With the lens L replaced the ring system due to the two flats (output mirror resonant reflector) is centred. With the opaque screen removed a complicated series of ring systems appears on the screen but all are centred. When the Q-switch cell is added it is only roughly aligned and is tilted slightly so as not to spoil the interference pattern on the screen.

The theoretical paper of Bergman and Thomson[33] claims that the angular deviation of the surfaces from plane parallel is given by

$$\alpha = \frac{d\delta}{s(s-d)} \times 10^5 \qquad \text{arc seconds}$$

where d is the mirror spacing, s is the distance from the screen to the back mirror and δ is the deviation of the centre of the ring system from the hole in the screen. All parameters were measured in cm. Thus with d = 50cm, s = 250cm and δ measurable to 0.1cm we find $\alpha \approx 10$ arc seconds. However in aligning the resonant reflector d = 7.5cm and s = 208cm so that $\alpha \approx 2$ arc second. In single mode operation the theoretical divergence of the laser is of the order 20 arc seconds assuming ideal alignment. The accurate alignment procedure described is therefore mandatory.

The longitudinal mode structure of the laser using a Brewster-angle roof prism for the high reflector with the resonant-reflector output mirror described above was measured by taking Fabry - Perot pictures and simultaneously looking for longitudinal mode beating in a fast detector. The Fabry - Perot interferometer used 10mm and 25mm spacers, and was focused onto the film plane with a 100cm lens. The finesse of the elaton with the 25mm spacer was measured to be 16 when the light source was a spectra Physics Model 119 single mode gas laser. Thus with 25mm spacers the inter-order spacing was 6000MHz ($0.20cm^{-1}$) and the resolution (bandwidth) was 375MHz ($0.0125cm^{-1}$).

The fast detector used was a coaxially mounted ITT F4000 biplanar photodiode impedance matched to the 125 ohm input impedance of a Tektronix 519 travelling wave oscilloscope. The overall risetime of the diode-oscilloscope combination was 0.35 nsec. (3db frequency, 10^9Hz).

Data is presented in Fig. (2-6) showing the results of these measurements.

The longitudinal mode spacing of the laser was 165MHz when using a prism reflector (see Appendix A and next section for more details). If two modes are selected the beat between the modes will occur at $^{nc}/_{4L}$ where n is an integer and $^{c}/_{4L}$ is the frequency spacing between adjacent longitudinal modes (see Appendix A). Thus for $n \leq 8$ ($^{nc}/_{4L} < 1300$MHz) the beat frequency will appear as a sinusoidal modulation of the normal single mode output on the diode signal displayed on the oscilloscope. We have rarely seen more than two modes in our laser and the values of n were usually 4 or 8. Single mode operation is indicated in Fig. (2-6).

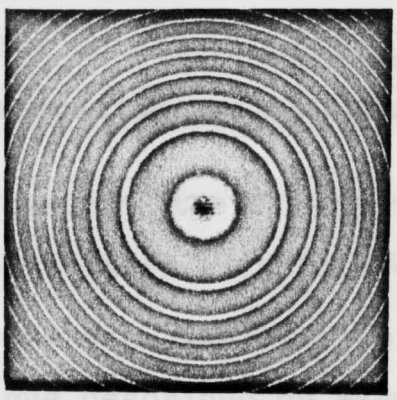

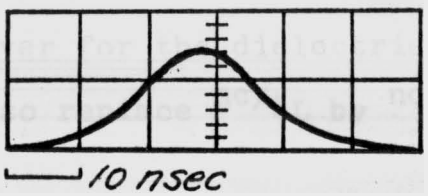

A. SINGLE MODE

FIG (2.6) DISPLAY OF LASER LONGITUDINAL MODE.

Occasionally both n = 4 and n = 8 mode frequencies appeared. This rare observation occurred when the dye-cell solution required changing.

Although the data presented here applies to the prism high reflector, similar results were obtained with the dielectric coated 10m spherical mirror. However for the dielectric mirror the mode spacing was 330 MHz. (Also replace $^{nc}/_{4L}$ by $^{nc}/_{2L}$).

To measure the divergence of the laser, far field photographs were taken with Polaroid type 55P/N film. About 8% of the beam was sampled with a pellicle beam splitter using a technique described by Waynant et al[34]. Two photographs were used to determine the full width beam divergence at the half power points. First the pattern was photographed such that the negative was not overexposed. Second, the pattern was photographed with a 50% glass attenuator inserted into the beam, keeping all other laser parameters constant. The peak of the second shot indicated the 50% level of the first image. Then the photometer trace of the distance X between half-power points in the focal plane is transcribed to angle via the focal length F of the lens: $2\theta = {}^{x}/_{F}$.

When operating in a single longitudinal mode the minimum

half-cone divergence angle measured was θ = 0.7 milliradians in the plane perpendicular to the plane containing the lamps. The ratio of the divergence in this plane to that in the plane containing the lamps was $^{3}/_{5}$ for the close coupling geometry and $^{6}/_{7}$ in the double cylinder pumping geometry.

It is obvious from the above discussion that a resonant reflector with thin flats of high index of refraction but the same air spacing should improve the mode selective properties of the resonant reflector. Such a reflector was constructed using high quality 3mm sapphire flats ($n \approx 1.76$) with the c - axis of the sapphire parallel to the ruby rod axis. This yielded a maximum reflectivity of $R_{max} \sim 66\%$ with the spacing between reflection maxima increased to $\Delta\nu$ = 30.1GHz from 10.5GHz and the fine structure due to the air-space remained the same. As expected, this reflector lowered the pump threshold slightly. If linewidth improvement occurred in the laser emission it could not be observed due to instrument limiting of the interferometer (~ 375MHz linewidth).

2-6 Transverse Mode Selection

We have shown in Appendix A that the transverse mode structure for a laser with cylindrical symmetry has a radial intensity distribution of allowable circularly symmetric TEM_{pl} modes given by

$$I \sim |\psi_{pl}|^2 = \left(\frac{2r^2}{w^2}\right)^{l}\left[L_p^{l}\left(\frac{2r^2}{w^2}\right)\right]^2 \exp\left(-\frac{2r^2}{w^2}\right) \qquad (2\text{-}2)$$

where as shown in Appendix A, r is the radial coordinate in the transverse plane and w is the spot size of the fundamental Gaussian beam defined as the radius at which the intensity of the TEM_{oo} mode is $1/e^2$ of its peak value on the axis. L_p^{ℓ} is the generalized Laguerre polynomial of order p and index ℓ.

The intensity distributions of the three lowest order modes described by Eq. (2-2) are plotted in Fig. (2-7).

Theoretically, the spot size of the modes $w_{p\ell}$ is defined as the radius at which the intensity is $1/e^2$ (≈ 0.135) of the outermost peak of that mode. These radii are plotted in Fig. (2-7) where the constants C_{mn} indicate the ratio of the radii of the different modes with respect to that of the lowest order mode C_{oo}. The values of these constants are $C_{oo} = 1.0$ $C_{o1} = 1.5$ and $C_{10} = 1.9$. It is evident from Fig. (2-7) that the TEM_{ooq} mode can be selected by introducing a circular aperture into the cavity which is adjusted to introduce large diffraction losses to the next higher order mode (TEM_{ol*q}) while allowing the TEM_{ooq} mode to oscillate with negligible loss.

With the above points in mind we can calculate the cavity parameters using the theory of the lowest transverse mode developed in Appendix A. According to Eq. (A-18) the TEM_{ooq} mode has a scalar electric field distribution given by

$$\frac{E(r,z)}{E_o} = \frac{w}{w_o} \exp\left[-j(kz - \varphi) - r^2\left(\frac{1}{w^2} + \frac{jk}{2r}\right)\right]$$

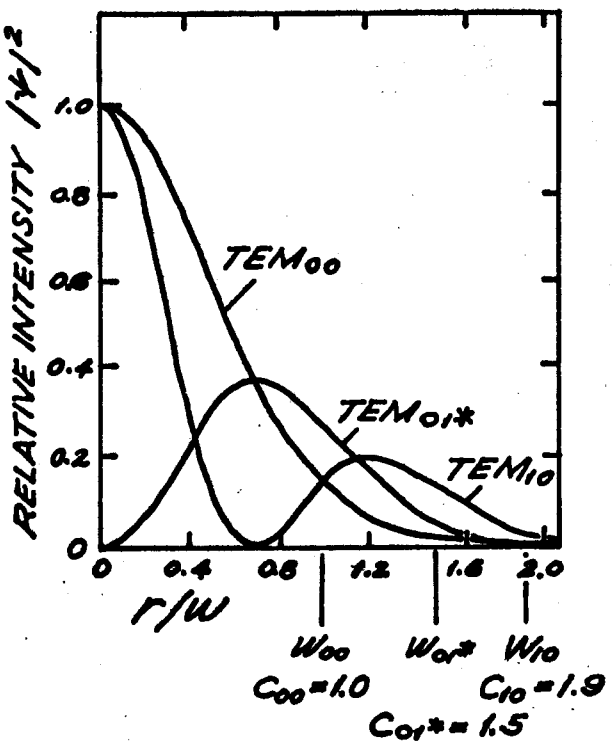

$$|\psi(\xi)|^2 = (2\xi^2)^m [L_m^n(2\xi^2)]^2 \exp(-2\xi^2)$$

FIG (2.7) RADIAL INTENSITY DISTRIBUTION OF THE THREE LOWEST ORDER TRANSVERSE MODES.

where $$\varphi = \arctan\left(\frac{\lambda z}{\pi w_0^2}\right)$$

The amplitude of this Gaussian beam is given by

$$|E(r,z)| = E_0 e^{-r^2/w^2} / (1+\xi^2)^{1/2}$$

where E_0 is the constant peak amplitude on the axis ($r = 0$). The radial and longitudinal intensity distribution is given by (neglecting absorption)

$$S(r,z) = S_0 e^{-2r^2/w^2} / (1+\xi^2) \qquad (2\text{-}3)$$

The variation of the spot radius w with distance z from the beam waist is given by

$$w^2 = w_0^2 (1+\xi^2) \qquad (2\text{-}4)$$

where $$\xi = z/z_0 = \lambda z/\pi w_0^2 \qquad (2\text{-}5)$$

and $$w_0^2 = 2z_0/k = \lambda z_0/\pi \qquad (2\text{-}6)$$

In terms of the radius of curvature R of the mirrors we have shown (Eq. A-30) that for one spherical mirror and one plane mirror a distance d apart,

$$z_0^2 = d(R-d)$$

while for the parallel-plane cavity approximated by two

curved mirrors with very large radius R (Eq. A-29)

$$z_o^2 = \frac{(2R-d)d}{4}$$

Defining the beam angle at r = w by $\delta = dw/dz$ one finds

$$\delta = \theta_o \xi / (1+\xi^2)^{1/2} \qquad (2\text{-}7)$$

where θ_o is the far field diffraction angle defined by

$$\theta_o = \lim_{z\to\infty} \frac{w(z)}{z} = \frac{w_o}{z_o} = \frac{\lambda}{\pi w_o} \qquad (2\text{-}8)$$

See Fig. (2-8) for a pictorial representation of the parameters just defined. For further explanation of the equations in this section the reader is referred to Appendix A.

Table (2-1) summarizes the relevant beam parameters of the laser optical resonators used in this study; δ is calculated at a distance of 100cm from the output mirror. For the plane-parallel optical resonator, the flat mirror surfaces were assumed to have curvature such that the difference between the edge of the mirror and the centre had sagittal depth $\Delta = r^2/2R \approx \lambda/10$ i.e. equivalent to the usual surface figure of the flats. Thus $R = r^2/2\Delta$ where r is the radius of the useful aperture of the mirror. The flats used had a useful aperture of r = 5mm and a surface figure of $\lambda/10$ leading to $R \approx 180$ meter.

Finally the frequency separation for the plane parallel mirror was estimated from Eq. (A-29) with R = 180m and using d = 50cm, to yield

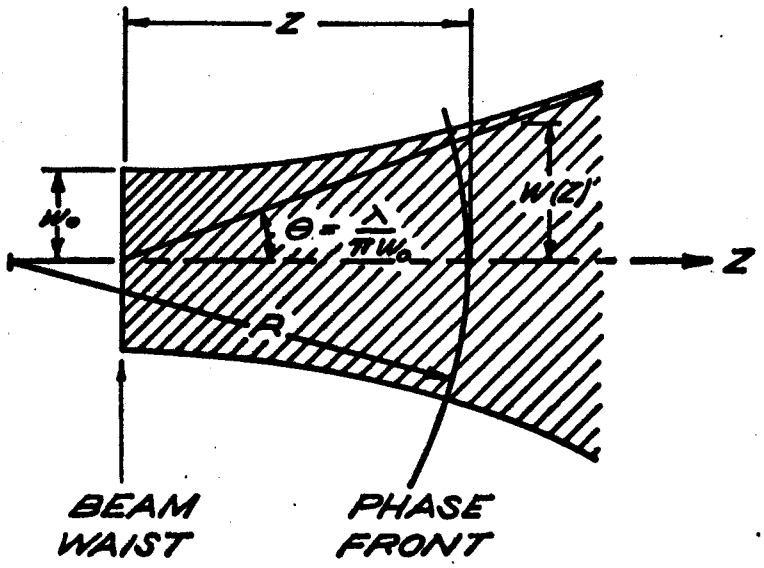

FIG (2.8) CONTOUR OF A GAUSSIAN BEAM.

	RESONATOR TYPE	R (m)	d (m)	Z_o (m)	w_o (cm)	θ_o (r)
A	PLANE - PARALLEL (DIELECTRIC MIRRORS)	180	0.50	6.70	.122	1.82×10^{-4}
	PLANE - PARALLEL (1 PRISM REFLECTOR)	180	0.50	9.47	.144	1.52×10^{-4}
B	PLANO - CONCAVE	10	0.50	2.18	.0695	3.18×10^{-4}
C	PLANO - CONCAVE	10	1.00	3.00	.0815	2.71×10^{-4}

PLANE - PARALLEL (d = .50m DIELECTRIC MIRRORS)	$\Delta\nu = 300\ \Delta q + 7.12(2\Delta p + \Delta \ell)$ MHz
PLANE - PARALLEL (d = .50m, 1 PRISM REFLECTOR)	$\Delta\nu = 150\ \Delta q + 5.0(2\Delta p + \Delta \ell)$ MHz
PLANO - CONCAVE (d = .50m)	$\Delta\nu = 300\ \Delta q + 21.5(2\Delta p + \Delta \ell)$ MHz
PLANO - CONCAVE (d = 1.00m)	$\Delta\nu = 150\ \Delta q + 15.4(2\Delta p + \Delta \ell)$ MHz

TABLE (2-1) LASER RESONATOR BEAM PARAMETERS

$$\Delta\nu = 300\Delta q + 7.12(2\Delta p + \Delta l) \quad \text{MHz}$$

Note that when using a prism as the high reflector while maintaining the same mirror spacing, the above frequencies would have to be divided by 2. Further, the spatial mode separation has the minimum value of 7.1MHz as compared to 1.23MHz estimated from microwave theory. This shows the failure of analytic solutions as applied to the plane parallel resonator. For the plano-concave resonator with $R_1 = 10\text{m}$ $R_2 = \infty$ we find from Eq.(A-30)

$$\Delta\nu = 300\Delta q + 21.5(2\Delta p + \Delta l) \quad \text{MHz} \quad ; \quad d = 50\,\text{cm}$$

$$\Delta\nu = 150\Delta q + 15.4(2\Delta p + \Delta l) \quad \text{MHz} \quad ; \quad d = 100\,\text{cm}$$

As can be seen from Fig. (2-7) and Table (2-1) the fundamental mode (TEM_{oo}) diameter, $2W_{oo}$, is about 2mm with the next high mode (TEM_{ol*}) requiring $2W_{ol*} \approx (1.5)(2W_{oo})$. Thus a circular aperture drilled with a number 47 drill (~2.0mm) was used to select the TEM_{oo} mode of the resonators summarized in Table 2-1. This aperture was mounted on a micromanipulator between the ruby and the cryptocyanine dye cell. By scanning in a plane parallel to the ruby face several points in the ruby were found to operate in the TEM_{oo} mode using the same aperture in all three resonators. The plano-concave resonator yielded single mode operation over more regions of the ruby than the parallel-plane mirror resonator. However the plano-

concave resonator was more difficult to align and quite often the next higher mode (TEM_{01*}) oscillated instead of the TEM_{00} mode. Also the divergence was found to be larger and the power in the TEM_{00} mode lower. In all three cavities the dye-cell was adjusted to about 40% low intensity transmission at 694.3nm and the laser aligned to operate in a single longitudinal mode. Then the aperture was added, the pump energy increased by 50% (typically to 1600Joules) and the the aperture scanned across the plane of the ruby face until single mode operation occurred. Without spatial mode selection the laser delivered approximately 90MW of power in a 25 nanosecond pulse (FWHM). When the aperture was added the TEM_{00} mode delivered a highly reproducible power output varying in intensity from 0.3MW to 2.8MW depending upon which part of the ruby the aperture selected. The FWHM remained at 25 nsec.

This large variation in output power depending upon which part of the ruby was selected is obviously dependent on local inhomogeneities in the ruby rod.

The results shown in Fig. (2-9) were obtained by scanning the beam 1m from the output mirror with a photodiode mounted behind a 30 micron pinhole[25]. Since each point on the diagram represents a separate laser firing for a given resonator the overall scan attests to the repeatability of the spatially mode selected laser. This repeatability is also evident from fast detector - 519 oscilloscope measurements. Points labelled

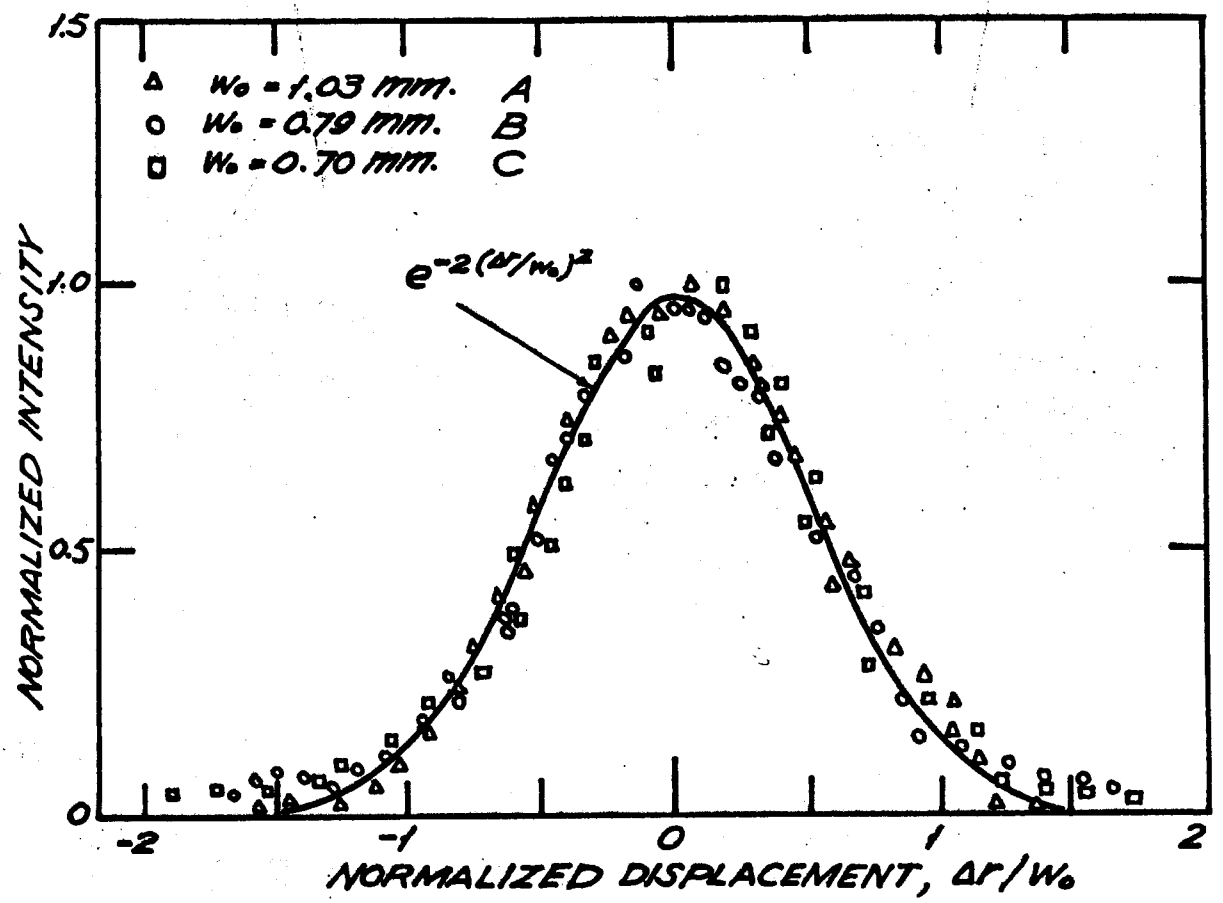

FIG (2.9) NORMALIZED INTENSITY OF TEM_{00} MODE.

A are due to the parallel-plane resonator with d = 50cm and those labelled B and C the plano-concave resonator with d = 50cm and 100cm respectively.

Eq. (2-2) was recast into normalized form to plot Fig. (2-9) with W_o as an adjustable parameter[25]. The values of W_o used are shown in Fig. (2-9) and are in fair agreement with the theoretical values presented in Table 2-1. Values of the half-angle beam divergence calculated using Eq. (2-7) and the experimentally determined spot size are (A) $\theta_o = 2.18 \times 10^{-4}$ (B) $\theta_o = 2.80 \times 10^{-4}$ and (C) $\theta_o = 3.16 \times 10^{-4}$ again in fair agreement with the theory.

Note added in proof: The data of curve A corresponds to the plane-parallel resonator with a prism for the high reflector.

CHAPTER 3

SAMPLE CLEANLINESS AND ITS EFFECT ON DIELECTRIC BREAKDOWN

3-1 Introduction: The Reasons for Requiring Clean Liquids

Early attempts to measure stimulated Brillouin scattering (SBS) in water as a function of laser input power were highly non-reproducible due to dielectric breakdown occurring sporadically and unpredictably near the threshold for SBS. This breakdown occurred for laser powers of 5 MW and above when the beam divergence (half cone angle at half-power) was 2.0 mr or less and the beam was focussed with a 5 cm focal length lens. Fig. (3-1a) is a photograph of the water filled cell containing as-received distilled water which had been exposed to the laboratory atmosphere several times and for undetermined periods of time during handling. The peak laser power was 30 MW, the beam divergence was 1 mr (half cone angle at half power) and the photograph was taken through a Corning 4-71 filter with Polaroid 410 film. Note the intense scattering along the entire focal cone on the laser side of the breakdown region. Also note what appears to be self-trapping[35] of the focussed laser beam and the strong absorption made evident by the lack of scattered radiation to the right of the focal region. Finally this dielectric breakdown and the resulting cavitation of the liquid generated a shock wave of sufficient strength that it shattered the sturdy glass cell at the lower corners with an audible "click".

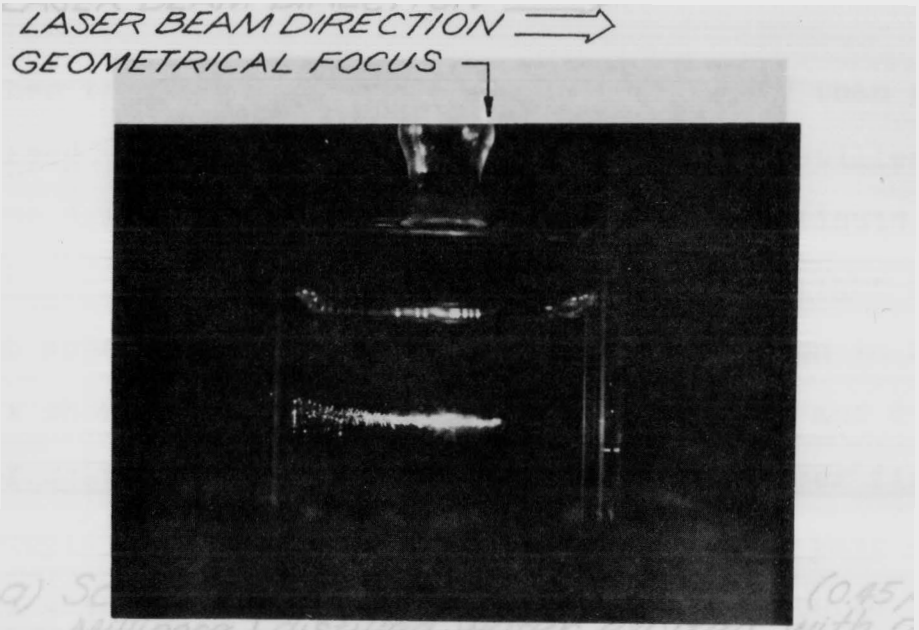

a) Breakdown in unfiltered distilled water (30 MW, 5 cm lens).

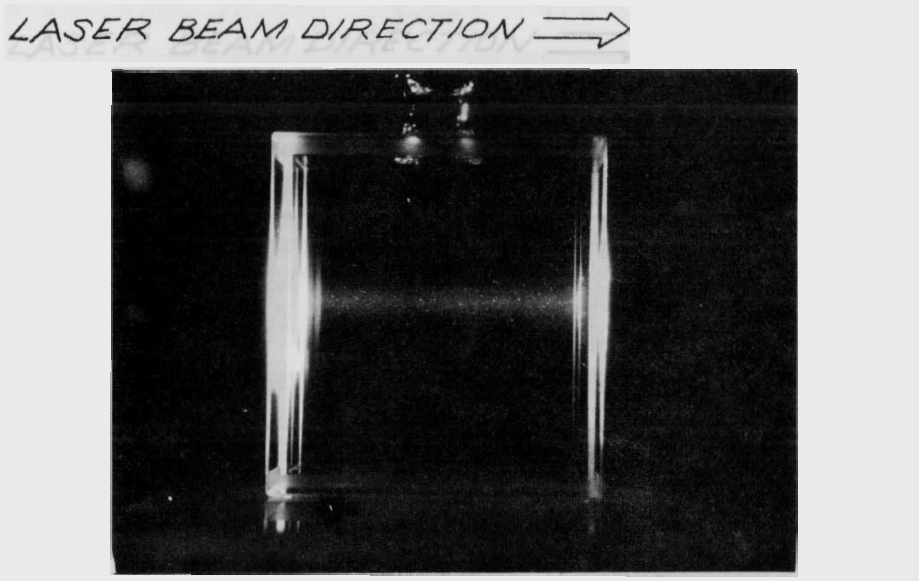

b) Scattered white light from unfiltered distilled water excited with a collimated laser beam (100 MW).

FIG(3.1) SCATTERING PHOTOGRAPHS OF FOCUSED AND COLLIMATED LASER BEAM IN UNFILTERED DISTILLED WATER (SCALE 1:1).

LASER BEAM DIRECTION ⟹

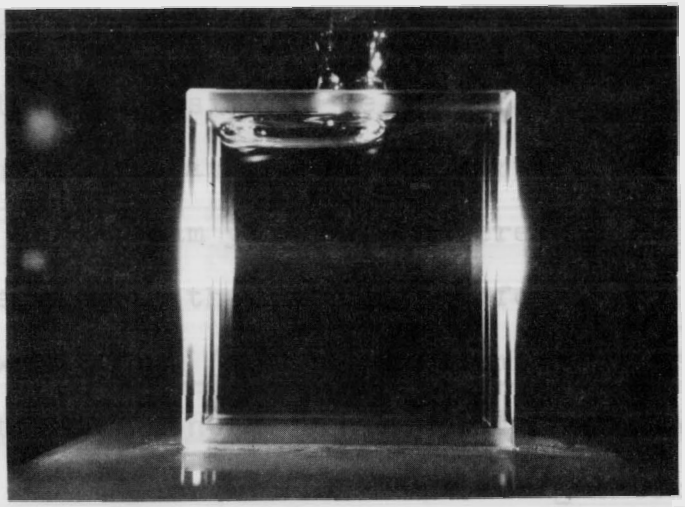

a) Scattered white light from filtered (0.45 μ Millipore) distilled water excited with a collimated laser beam (recorded on Polaroid 410 film through a 4-71 filter).

LASER BEAM DIRECTION ⟹

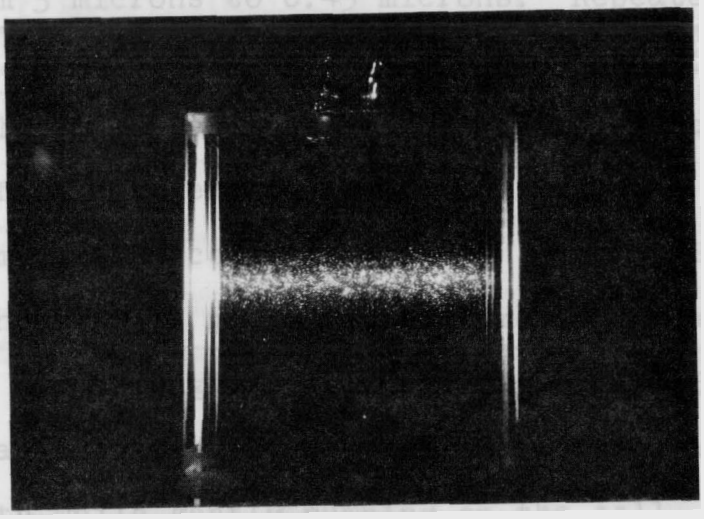

b) Scattered white light from dissolved O_2 in filtered (0.45 μ Millipore) distilled water excited with a collimated laser beam (Polaroid 410 film, filter removed).

FIG (3.2) SCATTERING PHOTOGRAPHS OF LASER EXCITED FILTERED WATER (SCALE 1:1).

When the laser beam was collimated (rather than focussed) and passed through a similar cell containing distilled water from the same source as above, the part of the liquid in the path of the laser beam yielded scattered white light similar to that appearing to the left of the focal region in Fig. (3-1a). This is shown in Fig. (3-1b). The number, size and distribution of scattering centres changed with each laser firing. No macroscopic cavitation with its resulting shock wave occurred in this case. When the distilled water was filtered into the cell through a Millipore filter attached to a hand pumped wash bottle, the intensity of the scattered radiation was sharply reduced as shown in Fig. (3-2a). The Millipore filters ranged in size from 3 microns to 0.45 microns. Repeated filtering of the same water sample and careful cleaning of the water cell with the filtered water reduced the scattered radiation further, so that it failed to expose the film with laser powers of up to 125 MW/cm^2 in the collimated beam. Fig. (3-2b) was photographed with the 4-71 glass filter removed and after bubbling filtered O_2 gas through the filtered water for 5 minutes. If the water was outgassed by heating the cell in an ultrasonic cleaning bath while gently pumping on the cell, this scattered radiation disappeared also.

3-2 Photodetection of a Broadband Luminescence

To investigate this phenomena further the apparatus of Fig. (3-3) was used. The laser operated in a single longitudinal

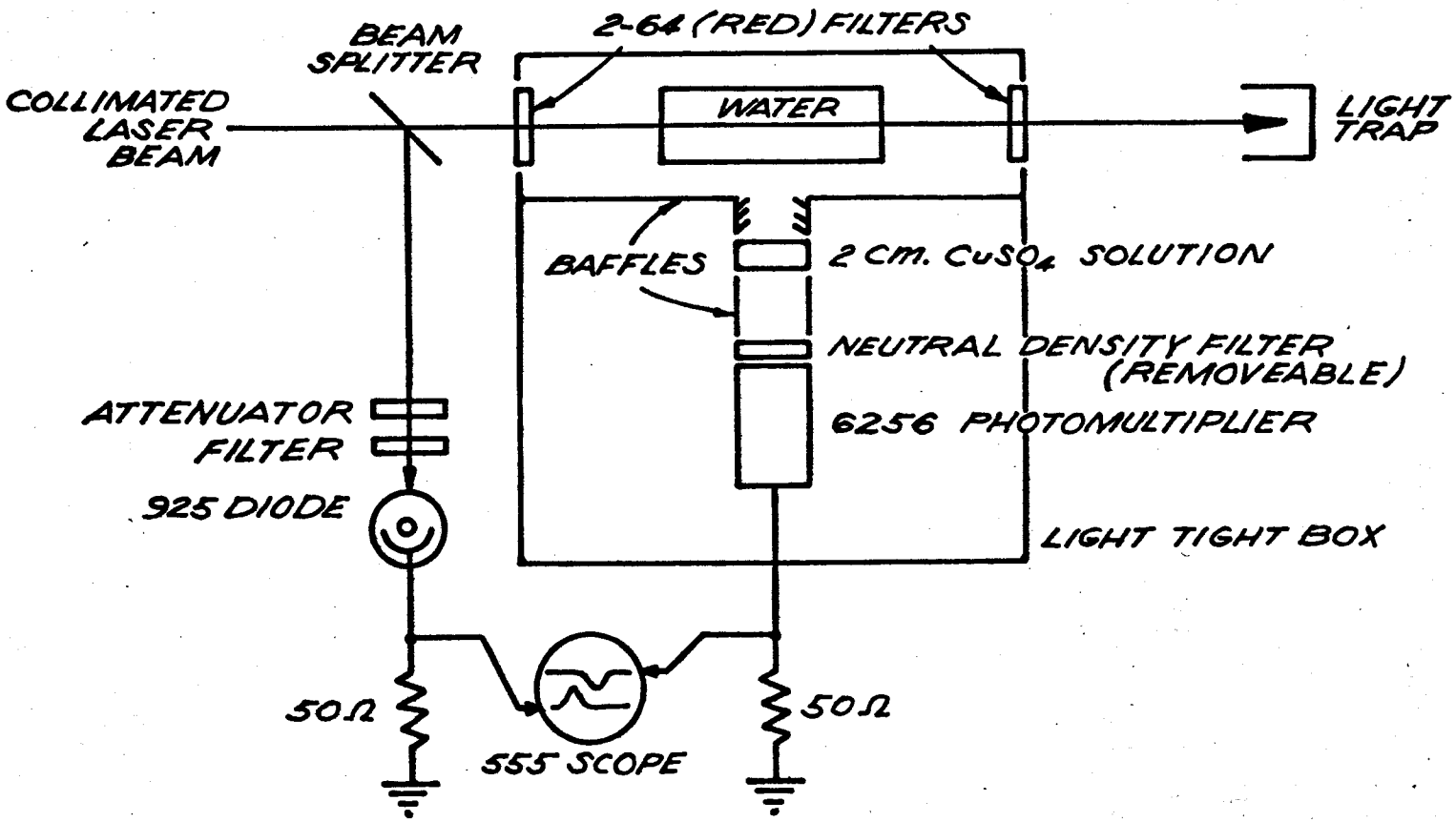

FIG (3.3) APPARATUS TO DETECT LUMINESCENCE FROM LASER EXCITED DISTILLED WATER.

mode and delivered powers up to 125 MW/cm^2 with a cross-sectional diameter of 1 cm inside the liquid cell. The laser emission was linearly polarized in the vertical plane. For complete details pertaining to the experimental apparatus refer to section (4-2) ahead. For the experiment described here the optical isolator and focussing lenses L_1 and L_2 of Fig. (4-1) were removed and the light box and photomultiplier (PM) were added as shown in Fig. (3-3). The photomultiplier (EMI 6256B, S-13 photocathode) responded linearly to 0.100 amps when biased above 1000 volts provided signals did not exceed 800 microseconds in duration. The maximum PM current gain was 2.5×10^7 when biased at 1550 volts. The optics preceding the PM were (a) 2 cm of concentrated $CuSO_4$ solution (O.D. = 16 at 694.3 nm) which passes the visible spectrum from 350 nm to 550 nm (see Appendix B) and (b) a removeable calibrated neutral density filter to prevent saturation of the PM photocathode and the resulting nonlinear response. The optical distance from the collimated laser beam in the water cell to the PM photocathode was 23 cm. When a red Corning 2-64 glass filter plus an interference filter centred at 694.3 nm with 3.0 nm passband were added behind the $CuSO_4$ solution, no signal could be detected from unfiltered liquids excited with the maximum available laser power and with the PM gain and oscilloscope set to their most sensitive scales. Thus signals received by the PM were not due to scattered laser light. The baffles and light tight box eliminated scattered light in the

cell, and room lights respectively. The input and output windows of the light tight box were red Corning 2-64 glass filters. Both monitor and PM operated into 50 ohm coaxially mounted loads which operated into 1A1 plug-in units of a Tektronix 555 oscilloscope with an overall system rise time of 12 nsecs.

Fig. (3-4a) shows a typical signal delivered by the PM (upper trace-signal increasing downward) and the laser monitor (lower trace). The PM signal shown was detected from a water sample which had been filtered once through a 1.2 microns pore size filter, with laser excitation of 50 MW. The ragged nature of the pulse smooths out and the pulse width narrows in more carefully filtered liquids, but the general shape remains the same[36].

Fig. (3-4b) shows data taken by Dowley et al[37] in which the absorption of a pulsed white light source was measured. This white light source was located on the opposite side of the water cell to the PM in our Fig. (3-3). Dowley triggered the pulse of white light from the triggering network of his Pockels Q-switched laser, so that it occurred during the time the laser beam was traversing the liquid cell[38]. Note the similar time dependence occurring in emission and absorption, particularly during the later time interval (>100 nsec).

The total luminescence detected through the $CuSO_4$ filter is plotted in Fig. (3-5) as a function of incident laser power, for two different water samples. The data labelled A was

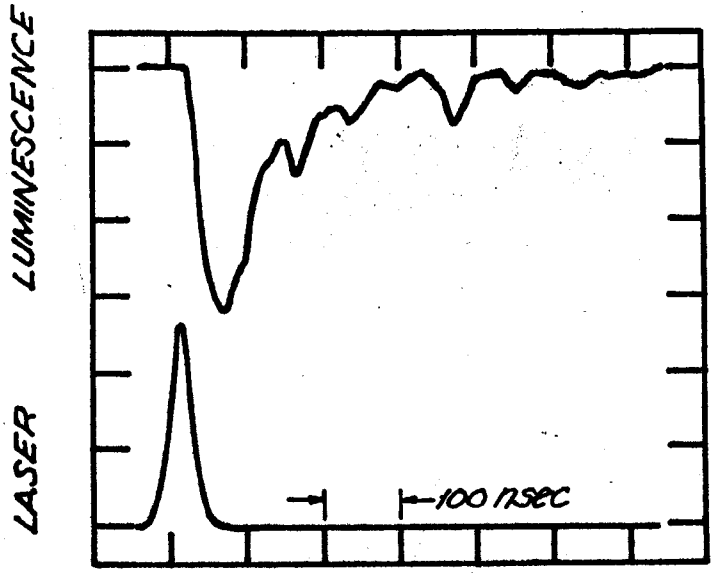

a) Luminescence emission (upper trace, increasing downward) and laser pulse (lower trace).

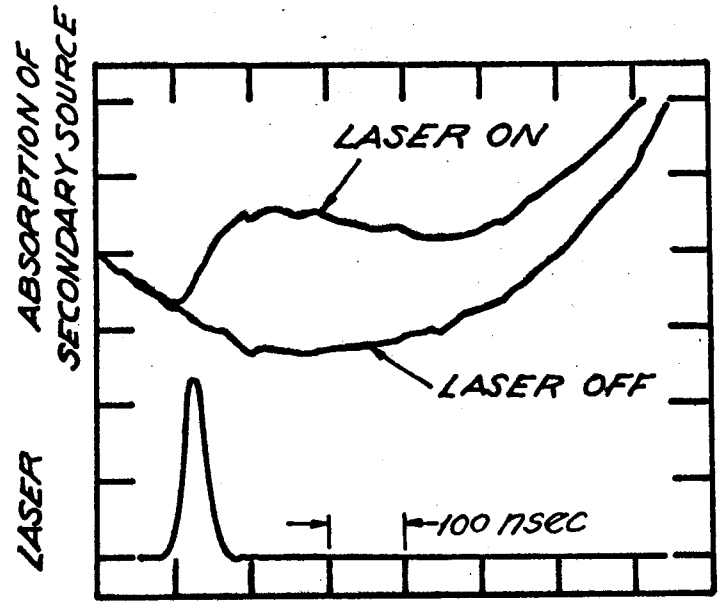

b) Absorption of secondary light beam (absorption increasing upward). Upper trace is a double exposure indicating the absorption of white light source (after Dowley[37]).

FIG(3.4) EMISSION AND ABSORPTION OF BROADBAND (WHITE) RADIATION IN LIQUIDS CONTAINING SUSPENDED PARTICULATE MATTER.

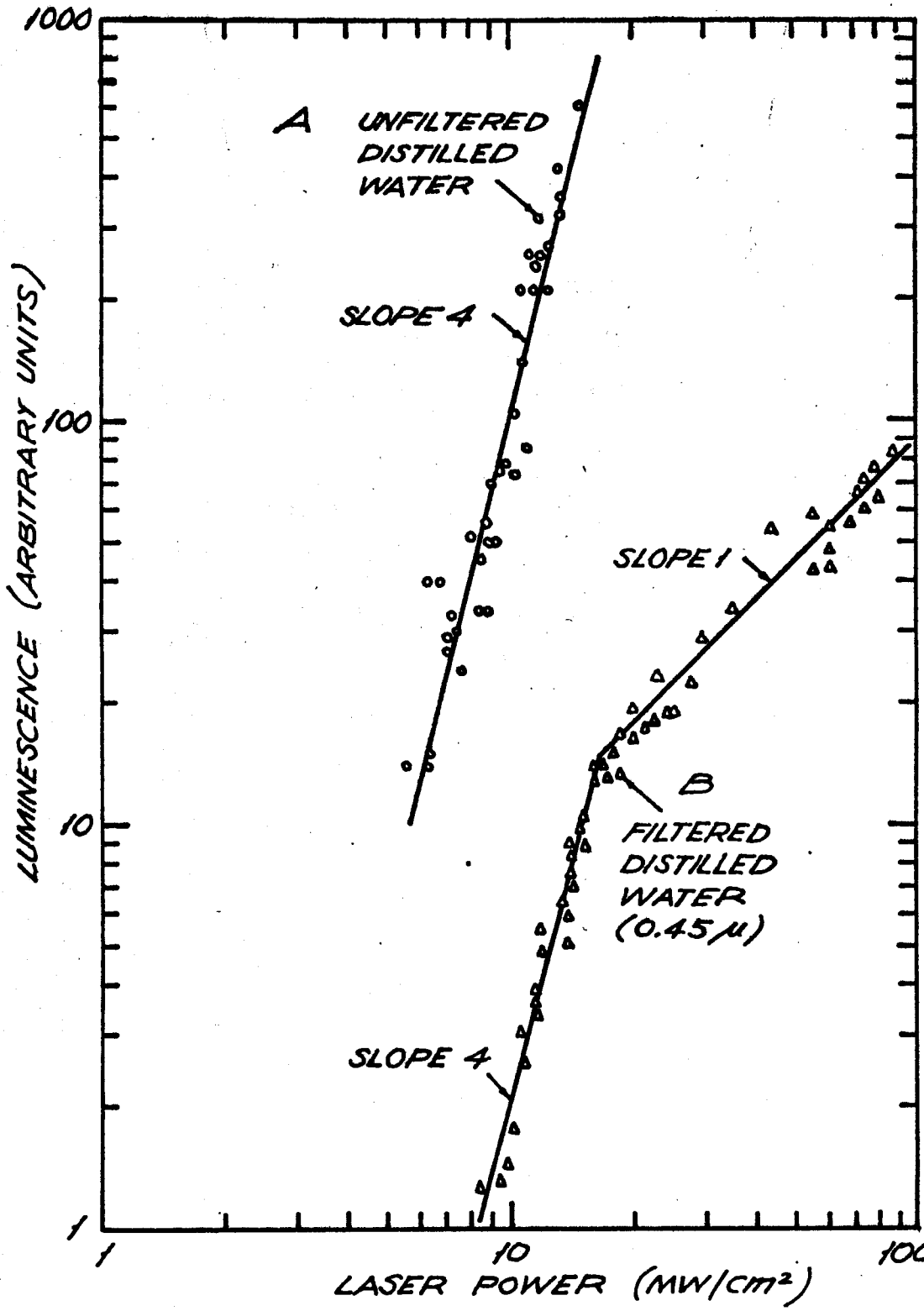

FIG(3.5) LASER POWER vs. LUMINESCENCE FOR UNFILTERED AND FILTERED WATER.

measured from unfiltered, as-received distilled water. The data labelled B was measured from distilled water that had been filtered once through a 0.45 microns Millipore filter. As the incident laser power, P, was increased in both samples the luminescence, L, increased with an approximately slope 4 dependence ($L \alpha P^4$). In the filtered sample the luminescence saturated above some ill-defined input power after which it increased linearly with increasing laser power. A sharply defined threshold was not apparent for this change. Further, if the data of both samples was plotted on linear graph paper the luminescence intensity appeared to be approaching zero asymptotically as the laser power was reduced toward zero. That is, there was no sharply defined threshold for the onset of the luminescence either. This result is in sharp contrast to the previously mentioned work of Dowley et al[37] in which a threshold for the luminescence in water "doped" with 15.0 nm Ludox silicate spheres was observed.

3-3 Discussion

The model we propose for this broadband emission is linear absorption of laser energy by the colloidally suspended particles which are heated well above the boiling point of water, leading to local ionization on a microscopic scale.

An exact solution to the problem of heating and ionization of small solid particles irradiated with optical radiation is most complex[39,40]. We present below a simple phenomenological

argument which appears to describe our observations adequately.

During the initial stages of heating an estimate of how much time is required to raise the temperature of the particle above the boiling point of the water in contact with it can be obtained from the heat conduction equation[41]

$$\frac{\partial^2 u(t,x)}{\partial x^2} - \frac{1}{\alpha}\frac{\partial u(t,x)}{\partial t} = 0$$

with the temperature $u = 0$ when $t \leq 0$ and the boundary condition

$$-K\frac{\partial u}{\partial x} = f(t)$$

when $x = 0$. Here, x is the depth of penetration into the solid measured from the irradiated surface, $f(t)$ is the flux of heat (laser beam) incident upon the surface expressed in watts/cm^2., α is the thermal diffusivity in cm^2/sec and K is the thermal conductivity in watts/cm-^{o}K[42]

The solution to the above equations yielding the surface temperature $u(t,0)$ assuming the particles to be immersed in a uniform flux (the collimated laser beam) and large enough to be considered semi-infinite in extent is easily shown to be[41]

$$u(t,0) = K^{-1}(\alpha/\pi)^{1/2}\int_0^t \tau^{-\frac{1}{2}} f(t-\tau)\,d\tau \qquad (3\text{-}1)$$

The uniform flux approximation is valid because the particles are small compared to the diameter of the collimated laser beam. The validity of treating the particles as semi-infinite may be estimated as follows. A rough criterion is that at the time of observation t, the extent of the lateral diffusion of energy into the particle from its surface and away from the particle into the water should be smaller than the thickness of the particle. In a time t this diffusion length is approximately $(\alpha t)^{1/2}$ where α is the diffusivity. We shall show shortly that this diffusion length is less than 10^{-4} cm.

To estimate how rapidly the particle heats up using Eq. (3-1) we consider the laser pulse to be approximately triangular in shape with rise time T so that

$$f(t) = \frac{P_o}{T} t \qquad o \leq t \leq T$$

where P_0 is the peak power in the pulse. Substituting into Eq. (3-1) we find that during the rising portion of the laser pulse,

$$u(t,0) = \frac{4}{3} \frac{\beta}{K} \left(\frac{\alpha}{\pi}\right)^{1/2} \frac{P_o}{T} t^{3/2} \qquad o \leq t \leq T$$

where the absorptivity of the particle β has been included. For most solid materials $\alpha \leq 1.0$ cm^2/sec.[42] and the value of the quantity $K^{-1}(\alpha/\pi)^{1/2}$ is approximately the same for all materials and in the units used here is ~0.2. Assuming an absorptivity $\beta \sim 0.5$[42] we find the surface temperature is

approximately

$$u(t,0) \simeq \frac{2}{3} \times 10^{7} P_0 t^{3/2}$$

where we have set the laser pulse rise time T = 20 nsec. If we substitute P_0 = 100 MW (the maximum power available) the time to heat the surface of the particle to the boiling point of water $u(0,t) = 100^{\circ}C$ is found to be $t \sim 2$ nsec. At the other extreme we calculate the minimum peak power required to raise the temperature of the particle to $100^{\circ}C$ by setting t = T. The result is $P_0 > 5$ MW.

Returning to our assumption that the particles are large compared to $(\alpha t)^{1/2}$ during this initial heating stage, we see that the "worst case" occurs for t = T = 20 nsec. Thus for $\alpha \leq 1.0$ $cm^2/sec.$ we find $(\alpha t)^{1/2} < 2 \times 10^{-4}$ cm. This result required that the absorbing particles be larger than 2 microns. Microscopic examination of the Millipore filters used to filter the distilled water revealed a few particles as large as 50 microns. However most particles trapped in the filter were approximately 10 microns and smaller in size having a variety of irregular shapes. Thus, the linear heat conduction equation can be expected to yield a reasonable first approximation to the rate of heating of the particle during the early stages of heating.

Following the onset of vapourization the behaviour of the plasma must be described by the equations of hydrodynamic

flow with radiation[39,40]. Since we lack knowledge regarding the composition of the particles, their size and the number irradiated by the laser, it would be pointless to pursue this complex problem further. However a phenomenological description of the probable course of events is possible. David et al[39] have described a model which adequately describes the interaction of laser radiation with a large, initially cool ablating surface in a vacuum and we use this model as a guide.

Once the linear absorption of the laser radiation has raised the temperature of the solid particle above the boiling point of the water in contact with it, a dense highly absorbing vapour layer will occur. The initial thickness of this layer may be estimated from the diffusivity of water, $\alpha \sim 10^{-3}$ cm^2/sec to be approximately 4×10^{-6} cm thick ($(\alpha t)^{1/2} \sim 4 \times 10^{-6}$ cm for $t = 20$ nsec). Further heating of this relatively cool vapour may then occur at later times due to molecular absorption with the eventual ionization of the vapour. The photographs in Fig. (3-1b) and the estimation above indicate that the plasma surrounding the particle was probably only a few microns in thickness at most. Hence, a significant portion of the laser energy would penetrate this plasma sheath to continue heating, vapourizing and ionizing the solid particle. The ionized vapour would be further heated by free-free and free-bound absorption resulting in strong ionization and re-radiation from the plasma.

The saturation which occurred in the luminescence emission

at high laser powers in filtered liquids is also indicative of a totally ionized breakdown plasma. See curve B in Fig. (3-5). Young[43] has shown that for laser powers greatly exceeding the breakdown threshold in gases, the total radiated energy increased linearly with increasing laser power.

The absorption data of Dowley et al[37] adds strength to this microscopic plasma model. These authors argue that attenuation of a white light source by a dense plasma of electrons and ions appears to be the only explanation of the essentially wavelength-independent broad-band absorption they observed.

Also, it is well known that the spectral distribution of dense plasmas closely resembles a black body spectrum. In particular, Peters[44] has shown that a dense water-vapour plasma radiates with a near perfect black body spectrum at 12000°K. Thus if we consider the microscopic plasma regions to be diffuse black body radiators the spectral distribution of the radiation intensity (watts/cm^2) in the wavelength band between λ and $\lambda + d\lambda$ is given by[42]

$$W(\lambda,T)d\lambda = \frac{2\pi hc^2}{\lambda^5} \frac{d\lambda}{\exp(hc/K\lambda T)-1} \qquad (3\text{-}2)$$

or

$$W(\lambda,T)\,d\lambda = \frac{C_1 \lambda^{-5} d\lambda}{\exp(C_2/\lambda T) - 1}$$

where $C_1 = 3.74 \times 10^{16}$ (Watts/cm^2) (nm)^4

$C_2 = 1.438 \times 10^{7}$ (nm) - °K

According to the Stefan-Boltzmann Law, the total black body radiation integrated over all wavelengths is

$$W(T) = \int_0^\infty W(\lambda;T)\, d\lambda = \sigma T^4 \qquad (3\text{-}3)$$

where

$$\sigma = 5.672 \times 10^{-12} \text{ Watts/cm}^2\text{-}^\circ\text{K}^4$$

Numerical integration of Eq. (3-2) over the visible portion of the spectrum transmitted by the $CuSO_4$ filter (350 nm to 540 nm) is possible using tables of black body functions[42,45]. This numerical integration in the temperature range 1000°K < T < 50,000°K yields approximately the same T^4 dependence predicted by Eq. (3-3). However it is impossible to fit meaningful theoretical curves to the data of Fig. (3-5) because the size and number of microscopic plasma regions, together with their temperature is not known.

Similar results were obtained in CCl_4 and methanol. We suggest that the phenomena are common to all liquids in agreement with Dowley et al[37].

Thus, in summary, the broad band luminescence occurring in liquids under excitation by a collimated laser beam probably involves linear absorption of the laser energy by colloidally

suspended particles. For sufficiently high powers the particles are heated to incandescence causing local boiling of the water in contact with them which further enhances the absorption process. For high incident laser power and/or small particle size the entire particle probably vapourizes and ionizes at which point the luminescence saturates and increases in intensity linearly with further increases in laser power.

3-4 Closed Cycle Filtering System

The filtering system finally adopted for preparing liquid samples free from suspended particulate matter is shown in Fig. (3-6). Filters with pore sizes as small as 0.01 microns were used in this apparatus. The components of this system were all manufactured by Millipore, Ltd. The filtering procedure was as follows. The "as-received" liquid (distilled water for the remainder of this thesis) was filtered through 0.45 micron filters using a Millipore vacuum filtering system. Then this filtered liquid was used to rinse all the components shown in Fig. (3-6) and the system was assembled. Plastic tubing connecting the stainless steel pressure vessel to the stainless steel pressure filter holder was made as short as possible. With approximately 10 litres of prefiltered water in the cleaned pressure vessel, the system was pressurized to 20 psi and about 1 to 2 litres passed through the system to flush and fill the components. Then the precleaned lucite water tank was connected as shown, and was filled and flushed twice before

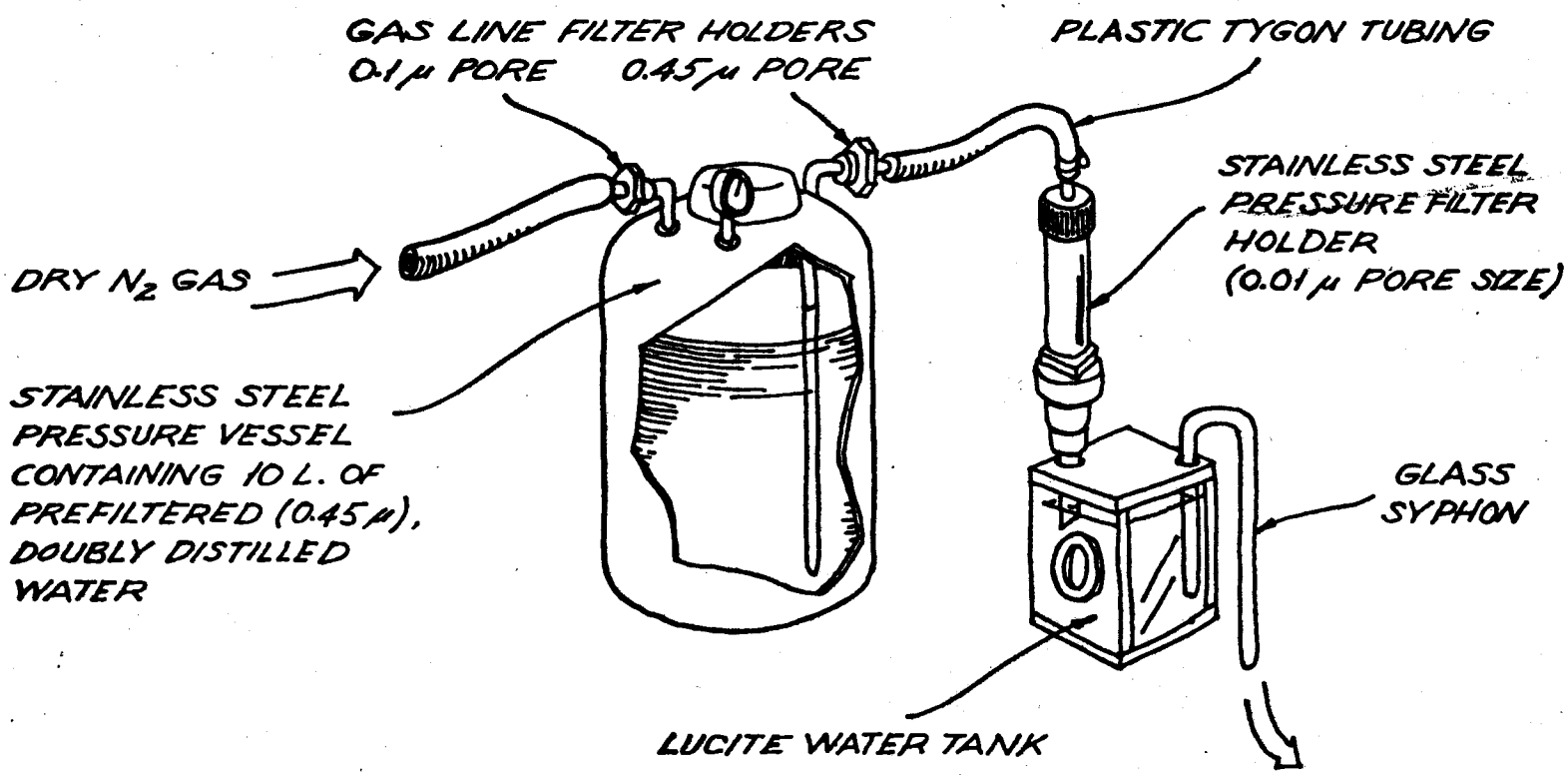

FIG (3.6) CLOSED CYCLE FILTERING SYSTEM.

the final filling. After the final filling, the tank was removed from the filtering system and the small inlet and syphon holes quickly sealed.

Liquids filtered in this manner with 0.01 micron filters showed little or no luminescence with laser powers up to 125 MW/cm^2. What little luminescence did appear in some liquids appeared to have a linear dependence on laser power.

Finally, distilled water that had been carefully filtered in this closed system required a focussed laser power density of $\sim 5 \times 10^{11}$ W/cm^2 to cause dielectric breakdown. Unfiltered water broke down with power densities as low as 10^{10} W/cm^2.

CHAPTER 4

GROSS FEATURES OF LASER INDUCED UNDERWATER BREAKDOWN PLASMA

4-1 Introduction

In this chapter, fast detector measurements time integrated photographs, and stimulated scattering measurements are discussed in order to determine the gross features of the breakdown plasma (hereafter referred to as the "spark") and resulting cavitation in water.

Having devised a technique for removing suspended particulate matter from distilled water in a reproducible way, measurements were performed in order to compare the laser generated underwater plasma to the extremely well studied breakdown plasma in air.

The somewhat surprising result of these measurements is, that the underwater breakdown plasma has little in common with breakdown plasma produced in air. It was predicted by Minck[46], that breakdown in liquids would probably be very similar to breakdown in gases at pressures exceeding 100 atmospheres where the molecular density of the gas approaches the molecular density in liquids.

Following a description of the experimental setup in section (4-2), it is shown in section (4-3) that the underwater spark does not have as clearly defined threshold as the air

spark, absorption of the incident laser pulse is less and the resulting plasma is short lived compared to the plasma created in air.

In section (4-4) time integrated photographs indicate the breakdown region is composed of individual breakdown regions separated by approximately 0.4mm and spread along the direction of propagation over a region of 5 to 10mm. A model proposed by Evans and Morgan[47] involving spherical aberration in the focal region appears to adequately describe this phenomena.

In section (4-5) measurements pertaining to back scattered SBS are presented. As much as 50% of the incident laser power was converted to the first Stokes stimulated Brillouin wave.

Finally, in section (4-6), we present results which indicate that self-trapping did not accompany the breakdown process in water.

4-2 Experimental Apparatus

The experimental apparatus used for measurements recorded in this chapter and the next is shown in Fig. (4-1). The laser operated in a single-longitudinal mode, with a half-cone divergence angle of 0.70 mr, at the half-power points, 20nsec FWHM and delivered powers up to 100MW. Stray white light from the flashlamps was eliminated with the Corning 2-64 filter. Most measurements in the sections to follow were made with circularly polarized light, introduced by the optical isolator

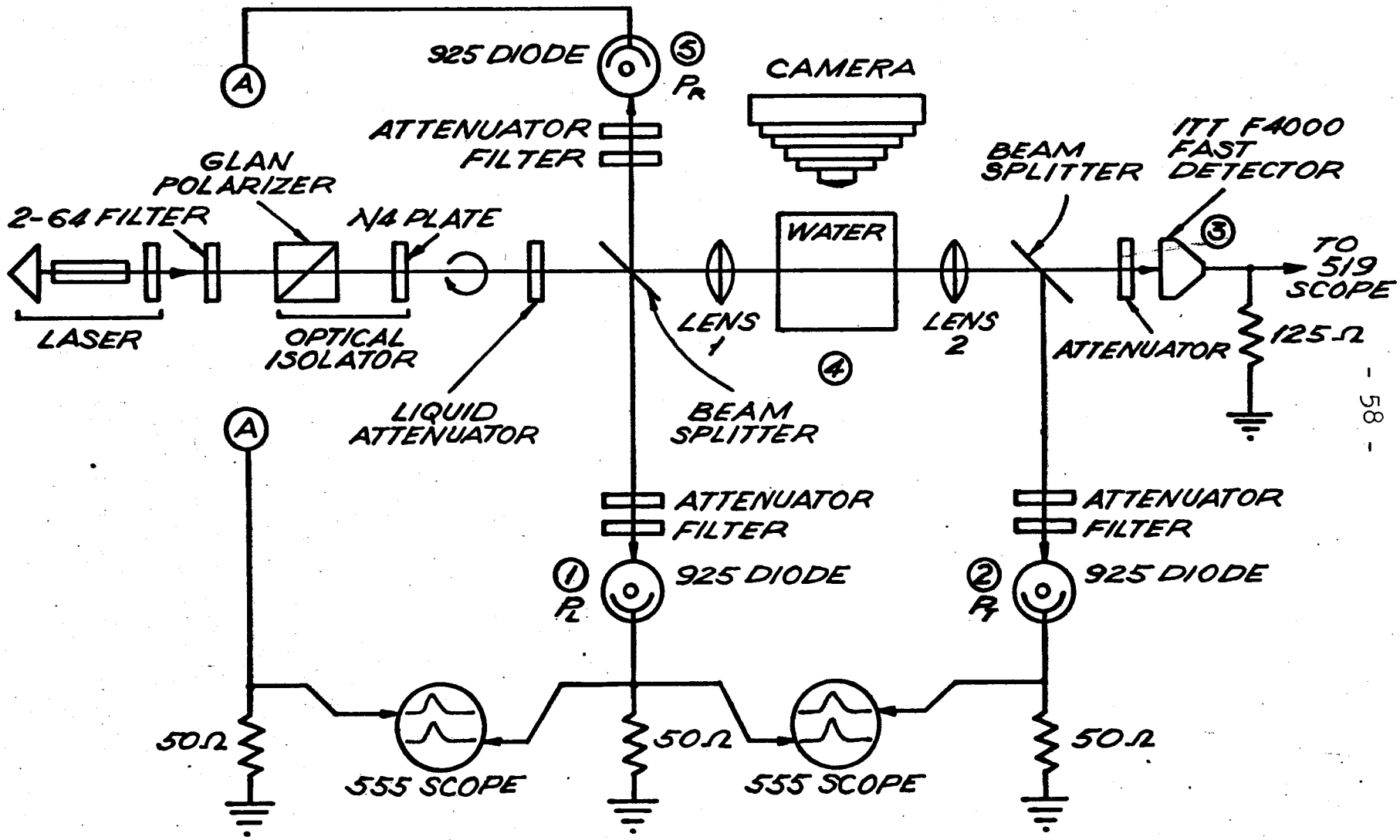

FIG (4.1) APPARATUS USED TO MEASURE LASER INDUCED BREAK-DOWN CHARACTERISTICS IN WATER.

consisting of a Glan polarizer, aligned to pass the plane polarized output of the laser and a quarter wave plate oriented to convert the plane polarized emission to circular polarized emission. Optical isolation was required in order to prevent the intense back scattered stimulated Brillouin scattering (SBS) generated in the water cell from re-entering the ruby-laser[48]. SBS in water is discussed in section (4-5). The liquid attenuator (LA) was used to adjust the laser power focused into the liquid cell through lens L_1. Lens L_2 served to re-collimate the laser radiation passing through the liquid cell. The beam splitters (BS) were either glass slides (measured reflectivity = 10% at 45° with circularly polarized light) or 8μ thick pellicles with reflectivity of 4% at 45°. The reflectivity of pellicles is a critical function of the angle of incidence[49] requiring extremely accurate alignment. The diodes labelled (1) Laser Monitor, P_L, (2) Transmitted Power Monitor, P_T, (3) SBS Monitor, P_R, were calibrated RCA 925 (S1 - cathode) vacuum photodiodes biased at 750 volts and preceded by suitable attenuators, diffusers, and spike filters. The diodes operated into 50 ohm coaxially mounted resistors which operate into 1A1 plug-in units of two Tektronix 555 oscilloscopes with an overall rise time of 12nsec. A typical attenuator - filter sequence in front of the 925 diodes was (a) 1cm of concentrated $NiSO_4$ solution with optical density (O.D.) of 5.0 at 694.3nm (b) a calibrated glass neutral density filter selected to maintain a reasonable signal current in the linear response

region of the diode (c) a ground glass diffuser (d) an interference filter with 3.0 nm pass-band centred at 694.3nm (usually called a "spike filter"). These diodes operated linearly from 10^{-5} to 8×10^{-2} Amps (pulse duration less than 100nsec) when biased at 750 volts. For further details pertaining to the diodes and liquid attenuators see Appendices B and C.

The ITT F4000 (S-1 photocathode) coaxially mounted biplanar photodiode[50] shown in position (3) was capable of 0.35nsec times when used in conjunction with a Tektronix 519 oscilloscope. In the position shown (Position 3) the diode monitors the time development of the transmitted pulse. This same diode was placed at position (4) (viewing the plasma at 90° to the direction of the laser beam) to measure the time development of the scattered laser light and the time development of the plasma itself. Suitable attenuators and filters preceded the F4000 diode depending on the application required.

The camera was used to record time integrated photographs of the plasma with magnifications up to 10X.

Most of the data presented in this thesis involves focused laser beams. It is essential when making quantitative calculations that the beam diameter in the focal plane of the lens be known. As will be shown in the next section the intensity distribution in the vicinity of the geometrical focus is exceedingly complicated. However the analysis we present below is based on a simple diffraction limited focus in which primary

lens aberrations are ignored.

The focused beam configuration is shown in Fig. (4-2). The lens is characterized by its focal length f and the incident laser beam diameter d combined to form the F-number F = f/d. The focused beam is characterized by its beam diameter S at the focal plane and its depth of focus L. Musal[51] has shown that for a variety of aperture illuminations from the uniform illumination of Born and Wolf[30] to the Gaussian illumination of Siegman[52] a simple relationship between the focal plane beam diameter S, the depth-of-focus L and the F-number of the system of the form

$$L = 4SF = 4Sf/d \qquad (4\text{-}1)$$

is approximately valid. The value most commonly used for S is the beam diameter in the focal plane where the intensity drops to one half its maximum value, which in terms of the focal length f and half-cone divergence angle θ is defined by

$$S = 2f\theta \qquad (4\text{-}2)$$

Thus the depth of focus may be written

$$L = 8f^2\theta/d \qquad (4\text{-}3)$$

For the laser used here $2\theta = 1.4 \times 10^{-3}$ r, d = 1cm and using a 5cm lens L = 1.4mm S = 7.0×10^{-2}mm = 70 microns. It is interesting to compare this experimentally determined value with the ideal diffraction limited focus for uniform plane

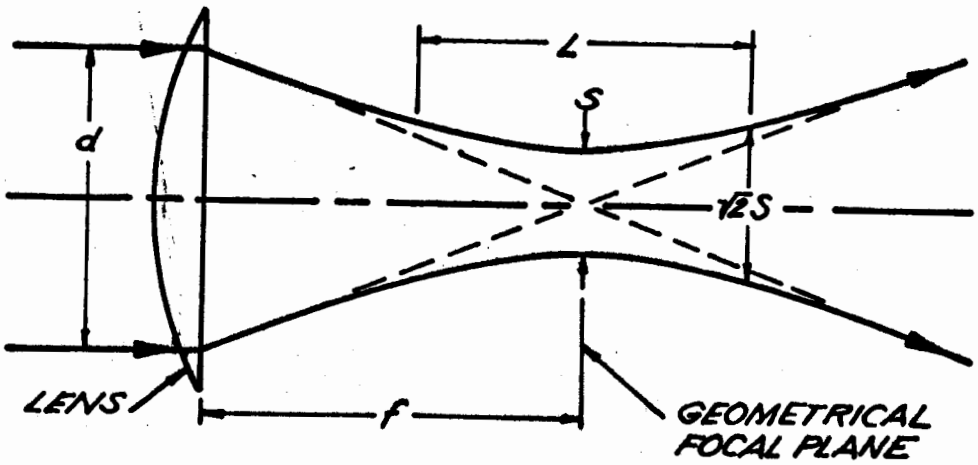

FIG (4.2) FOCUSED BEAM PARAMETERS.

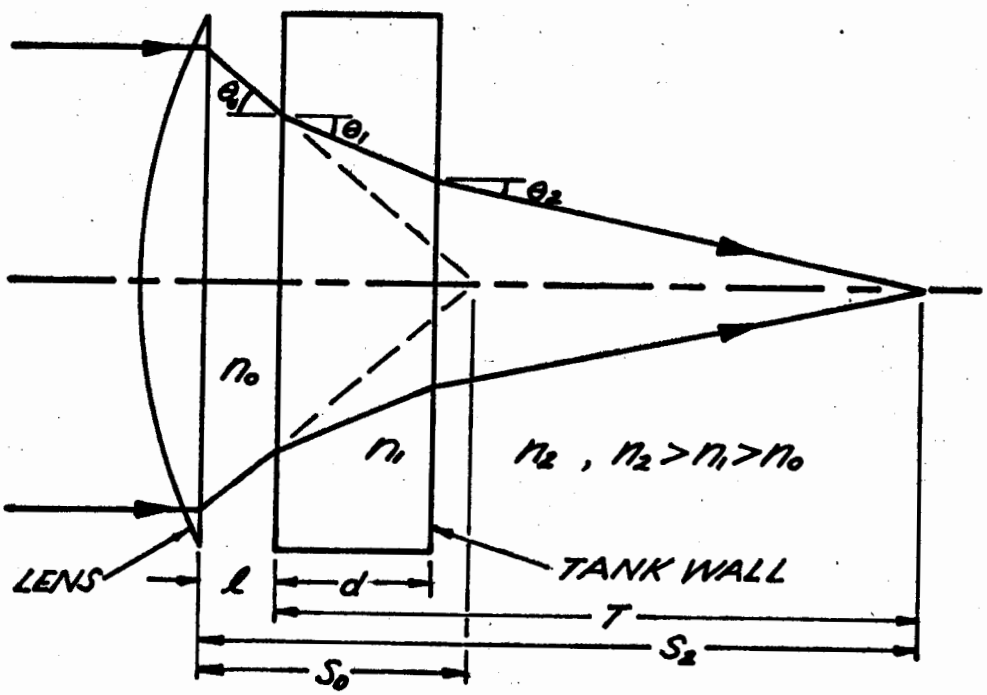

FIG (4.3) REFRACTION OF FOCUSED BEAM.

waves. Born and Wolf[30] (pg.441) show that the intensity along the direction of laser propagation, z, is given by,

$$I = \left[\frac{\sin u/4}{u/4}\right]^2 I_o$$

where

$$u = \left(\frac{2\pi}{\lambda}\right)\left(\frac{d}{2f}\right)^2 z$$

If we assume that a loss in intensity of 50% (half-power) is permissible then the value of u for which $\left(\frac{\sin u/4}{u/4}\right)^2 = 0.5$ must be found. This requires that $u = \pm 5.56$ which leads to

$$\Delta z = \pm 5.56 \left(\frac{\lambda}{2\pi}\right)\left(\frac{2f}{d}\right)^2 = \pm 3.54 \lambda \left(\frac{f}{d}\right)^2$$

Setting $\lambda/d \approx \theta$ and realizing $L = 2|\Delta z|$ we find $L \cong 7f^2\ \theta/d$ in close agreement with equation (4-3).

When focusing the laser beam into the rectangular tank containing water, or when photographing the underwater spark, the position of the focusing (or camera) lens must be adjusted to compensate for the refraction occurring inside the tank. By a repeated use of Snell's law it is easily shown that the focal position with the tank in place (S_2), is related to the focal position in air (S_o) via the equation

$$S_2 = S_o\left[\frac{n_2\cos\theta_2}{n_1\cos\theta_1}\right] - l\left[\frac{n_2\cos\theta_2}{n_o\cos\theta_o} - 1\right] - d\left[\frac{n_2\cos\theta_2}{n_1\cos\theta_1} - 1\right]$$

where all the parameters are shown on Fig. (4-3). For most applications the ratios of the cosines are very close to unity and $n_o \approx 1.0$. Thus we write

$$S_2 = n_2 S_o - \ell(n_2 - 1) + d\left(1 - \frac{n_2}{n_1}\right) \qquad (4\text{-}4)$$

This equation finds use in determining the position of the spark in the liquid cell for a given focal length lens $f = S_o$ located a known distance ℓ from the input window to the tank. Typically the lens is located ℓ = 1cm from the glass input window with d = 0.3cm, $n_1 = 1.50$ and for water $n_2 = 1.33$, leading to

$$S_2 = 1.33 f - 0.30 \quad \text{cm} \qquad (4\text{-}5)$$

With f = 5cm, S_2 = 6.35cm compared to S_o = 5cm in air.

When photographing the underwater spark it is more convenient to recast Eq. (4-4) into the form

$$S_2 = S_o + T\left[1 - \frac{1}{n_2}\right] + \frac{d}{n_2}\left[1 - \frac{n_2}{n_1}\right] \qquad (4\text{-}6)$$

where T is the distance to the spark measured from the outside wall of the tank. Photographs taken from the side in the 4 inch lucite tank (T = 2 inches = 5.08cm) with $\frac{1}{2}$ inch walls (d = 0.5 ich = 1.28cm) yields

$$S_2 = S_o + 1.35 \quad \text{cm.} \qquad (4\text{-}7)$$

Thus the camera must be moved back an additional 1.35cm after calculating S_o from the magnification desired i.e. $S_o = f(1 + {}^{1}/_{m})$ where m is the magnification.

Experimental checks were made of Eqs. (4-2), (4-3), (4-5) and (4-7). The parameters S and L were measured by photographing the focused laser beam in a tank of water to which a few ml. of milk had been added to render the beam visible. After correcting for the modified focal length using Eq. (4-5) the measured and calculated beam diameter S agreed within 25%. However the measured depth of focus L was approximately 2.0x longer than predicted by Eq. (4-3). Since spherical aberration introduced by the lens was neglected in the derivation of Eq. (4-3) this result was not surprising, as will be shown in section (4-4). The position of S was used to check Eq. (4-5) and was found to agree closely with the predicted result. Eq. (4-7) was checked by suspending a reticle in the tank of water and measuring the magnification after locating the camera lens using Eq. (4-7).

4-3 Comparison Between Laser Induced Breakdown in Air and Water

The plasmas resulting from laser induced breakdown in air and water differ considerably with only a few common characteristics. In this section we compare breakdown in air and water from measurements performed with a fast coaxially mounted ITT F4000 photodiode coupled to a Tektronix 519 oscilloscope with 0.35 nsec risetime.

The apparatus used is essentially the same as that depicted in Fig. (4-1) in the previous section. Only the laser power monitor (1) and ITT F4000 coaxial diode (3) were used here, however. The laser attenuator (LA) in Fig. (4-1) was positioned as shown with the optical density (O.D.) adjusted to prevent breakdown in either air or water and to reduce the incident power below the threshold for stimulated Brillouin scattering (SBS) in water. To prevent breakdown and SBS O.D. = 2.0 was used with the 96MW incident laser power available. When breakdown was desired the attenuator LA was repositioned in front of the laser monitor diode (1) and a second attenuator of equal O.D. place directly in front of the fast detector (3). In this way the signals received by the diodes remain the same with and without breakdown occurring.

Threshold values for breakdown in air and ultra clean water were determined when using a simple lens with 5.0cm focal length and shape factor[53] q = 0. The breakdown threshold in air occurred at 32 ± 2MW which lead to $6.9 \pm 0.4 \times 10^{11}$ W/cm^2 in the focal plane of the lens, calculated using the measured laser divergence of 0.7mr (see last section). This agrees closely with the value determined by Minck[46]. Breakdown in air was always accompanied by an intense flash of white light and loud audible crack, even when the threshold power density for breakdown was just exceeded.

The breakdown threshold power in water was not as clearly

defined as in air. Near the breakdown threshold power density of $(5 \pm 4) \times 10^{11}$ W/cm^2 the breakdown region appeared as a small spherical spark with radius less than 0.2mm. Further, the breakdown threshold was 10x to 20x higher than the SBS threshold. The large uncertainty in the threshold power density is attributed to competing effects such as SBS, depleting the incident power density available for breakdown. The breakdown threshold could be lowered momentarily in water by bubbling Millipore filtered nitrogen into the water tank. See Fig. (3-2) for effect of gas in water. This could lower the breakdown threshold by an order of magnitude, but after 4 to 10 ionizing laser shots the resulting shock wave appeared to outgas the liquid and the threshold returned to its previous high value. The surprising result was that the threshold for breakdown in water was so high.

Brewer and Rieckhoff[15] reported that breakdown and SBS frequently occurred simultaneously at power densities $\lesssim 5 \times 10^{10}$ W/cm^2. Carome et al[17] report breakdown occurring at powers as low as 1.7MW; however no divergence figure is quoted in this reference. In all the data recorded here the threshold for SBS in water was at least 10x lower than the breakdown threshold in sharp contrast to references 15 and 17. We should point out however that when using unfiltered distilled water, the results of Brewer and Rieckhoff were duplicated. More will be said regarding SBS in the following section.

With the liquid attenuator (LA) removed, the incident laser power of 96MW exceeded the breakdown threshold in both air and water by approximately three times. The resulting signals detected by the biplanar diode and displayed on the 519 oscilloscope are summarized in Fig. (4-4). The traces displayed are (a) the incident laser pulse (b) the transmitted laser pulse (c) the laser light scattered by the plasma and detected at 90° to the incident beam direction (d) the plasma light emission viewed at 90° to the incident beam direction. The curves (a) and (b) have the same vertical scale indicating the magnitude of the absorption after breakdown occurs. The curves (c) and (d) indicate the time development of the scattered light only; the magnitudes being arbitrary.

The transmitted pulse for air indicates the usual strong absorption of the laser beam after breakdown has occurred[54]. Although the laser beam transmitted through the underwater spark was reduced by 50%, the sharply defined cut-off in the transmitted pulse that occurred in the air spark was not evident. We will show in section 4-5 that this "absorption" of 50% is due to depletion of the incident beam by back scattered SBS.

The scattered laser light, curve (c) in Fig. (4-4), was only a small fraction of the incident laser power. In air the laser light was Thomson scattered by the free electrons[54]. In water Rayleigh and Brillouin scattering is strong[55] and

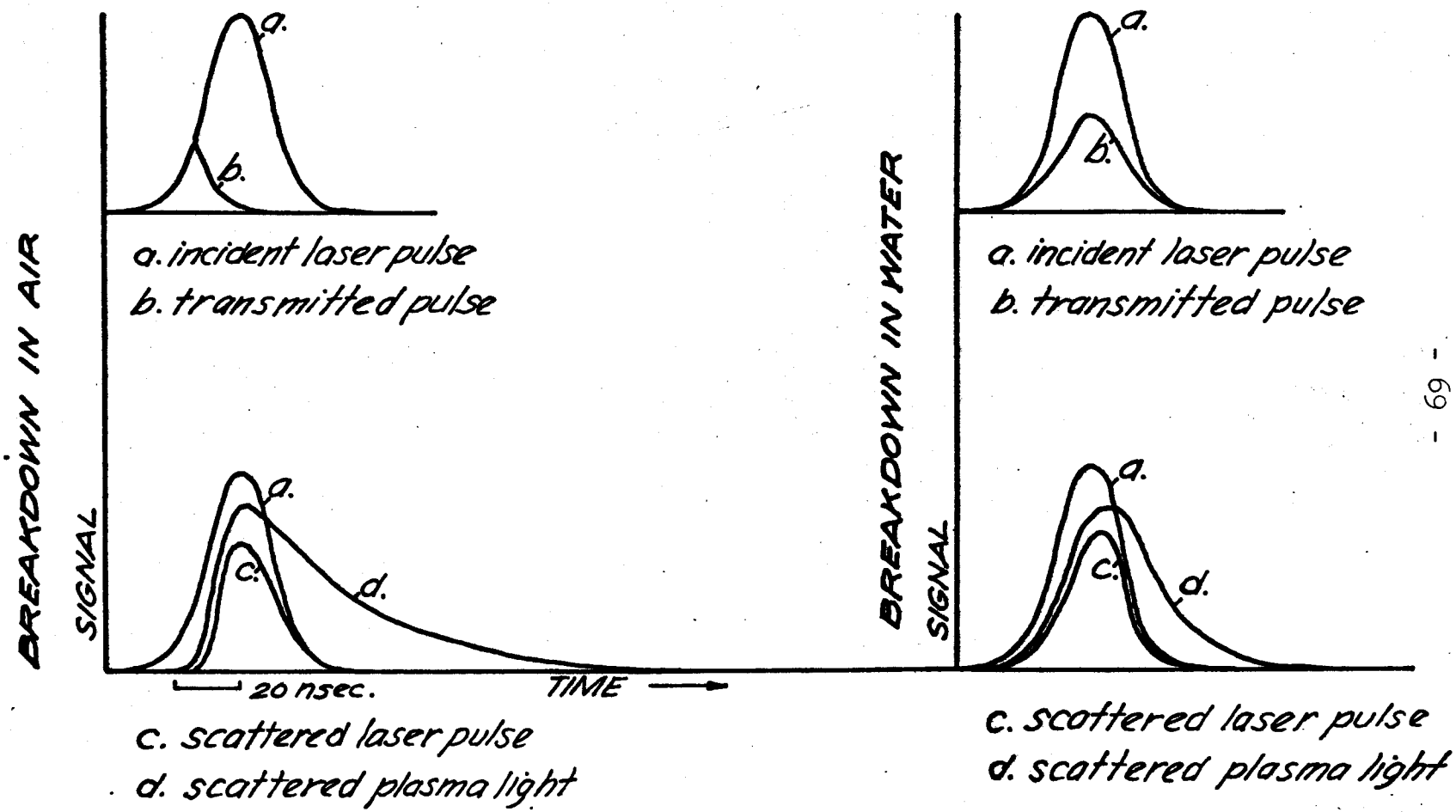

FIG (4.4) FAST DETECTOR SIGNALS FOR BREAKDOWN IN AIR AND WATER.

scattered light from the cell walls and windows can be significant. Hence the scattered laser light in curve (c) for water was not entirely due to the plasma. We discuss the scattering from the underwater spark in more detail in chapter 5.

Finally the plasma emission measured with 1cm of concentrated $CuSO_4$ preceding the fast detector is shown as curve (d). In air, the plasma emission was sharply peaked but decayed slowly, lasting as long as 100nsec. In contrast, the light emitted by the underwater plasma lasted for only 40nsec.

4-4 Photographs of the Underwater Breakdown Plasma

Time integrated photographs of the white light emitted from the breakdown plasma were taken through 1cm of $CuSO_4$ solution (O.D. = 8 at 694.3nm) using Polaroid Type 47 film, and appear in Fig. (4-5). The photographs were taken from the side (see Fig. (4-1)) and the magnification was approximately 10x. The complexity of laser induced underwater breakdown is clearly illustrated in these photographs.

As noted in the previous section, breakdown in water builds up slowly with increasing laser power above the threshold value of $\sim 5 \times 10^{11}$ W/cm^2. This is evident in the photographs appearing in Fig. (4-5). The focused laser beam originates from the left hand side of the page. The first photograph in the series shows the small, approximately spherical plasma which appeared close to the calculated geometrical focus when the breakdown threshold was just exceeded. As the laser power

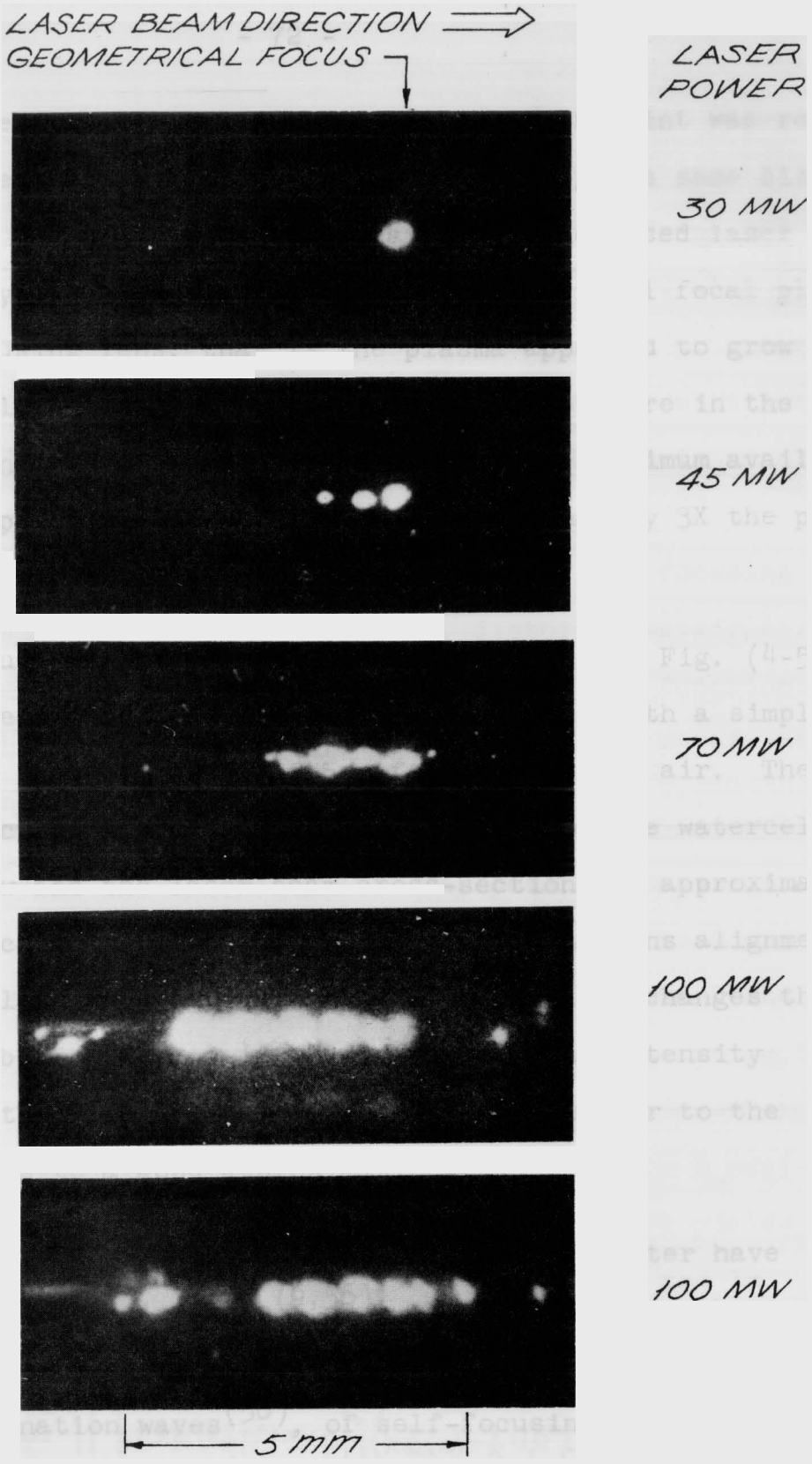

FIG (4.5) BREAKDOWN PHOTOGRAPHS SHOWING EFFECTS OF SPHERICAL ABERRATION.

was increased the original spherical breakdown point was replaced by several such points of approximately the same size and shape. The plasma points appearing at increased laser powers always were located between the geometrical focal plane and the focusing lens, that is the plasma appeared to grow backwards along the laser beam. The bottom picture in the series shown in Fig. (4-5) was taken with the maximum available laser power of 100MW, which was approximately 3X the power required at threshold.

To produce the breakdown plasmas appearing in Fig. (4-5), the laser beam was focused into the water cell with a simple lens (shape factor, q = 0) of 5cm focal length in air. The lens was located approximately 1cm in front of the watercell input window and the laser beam cross-section was approximately 1cm and carefully centred on the lens. The lens alignment was critical, since tipping or rotating the lens changes the spherical aberration and introduces coma. The intensity profile of the laser beam in a plane perpendicular to the lens axis was to a good approximation, Gaussian.

The discrete breakdown points occurring in water have also been observed in gases[9,56]. Various theories have been proposed to account for this observation based on concepts of detonation waves[56], of self-focusing of the laser beam[9] and spatial and temporal variation in the beam profile[57]. None of these models gave a totally satisfactory

explanation of the phenomena as it occurs in gases. Recently, however, Evans and Morgan[47,58] showed that primary spherical aberration caused by the use of simple lenses to focus the laser beam can, under the conditions discussed below, account for the multiplicity of distinct collinear regions of breakdown along the optic axis. We propose that the observations recorded in Fig. (4-5) for laser induced breakdown in water originate from the same effect. Evans and Morgan[47] point out, that due to the relatively large area of the focusing lens that is illuminated by the laser, distorted wavefronts occur with values of primary spherical aberration function Φ of several wavelengths. This distortion of the wavefronts leads to complex intensity distributions.

The value of the intensity I at any point in the region of the focus of a given lens and laser system may be computed from the Huygens-Fresnel-Kirchoff integral[30]. Evans and Morgan[47] solve this integral assuming a laser operating in a single spatial mode of beam radius a and with a Gaussian electric field intensity profile of the form $E(r) = E_o \exp(-r^2/2a^2)$ for $0 < r \leq a$. The equation Evans and Morgan solve yields the spatial variation of intensity near the focus and is given by

$$I = \left[\frac{2\pi A a^2}{\lambda f^2}\right] \left| \int_0^1 \exp\left(-\tfrac{1}{2}\rho^2\right) \exp\left[j\left\{k\Phi(\rho) - \tfrac{1}{2}u\rho^2\right\}\right] J_o(\rho v)\, \rho\, d\rho \right|^2 \qquad (4\text{-}8)$$

where $\rho = r/a$, k is the wavenumber and A is a constant governed by the electric field at the lens. The coefficients u and v are the so-called optical co-ordinates given by

$$u = \left(\frac{2\pi}{\lambda}\right)\left(\frac{a}{\rho}\right)^2 z$$
$$v = \left(\frac{2\pi}{\lambda}\right)\left(\frac{a}{f}\right) y \qquad (4\text{-}9)$$

where λ is the wavelength of the laser light in the water and y and z represent distances measured radially and axially from the geometrical focus.

The solution of Eq. (4-8) must be performed numerically. The results of such calculations are shown in Figs. (4-6) and (4-7). In Fig. (4-6) the primary spherical aberration increases from zero to two wavelengths. The trend of the intensity profiles with increasing spherical aberration is clearly visible from these sketches. Fig. (4-7) is taken from the work of Evans and Morgan[47] and indicates the lines of constant intensity in the focal region of a 5cm focal length f/5 simple lens. The intensity is normalized to 100% at the principal focus.

The isophotes of Fig. (4-7) clearly demonstrate how regions of high intensity maxima lying along the optic axis could lead to discrete plasmas localized in these regions of very intense field strength.

Transformations into real space for the ruby wavelength focused in water shows that the separation, d, between maxima

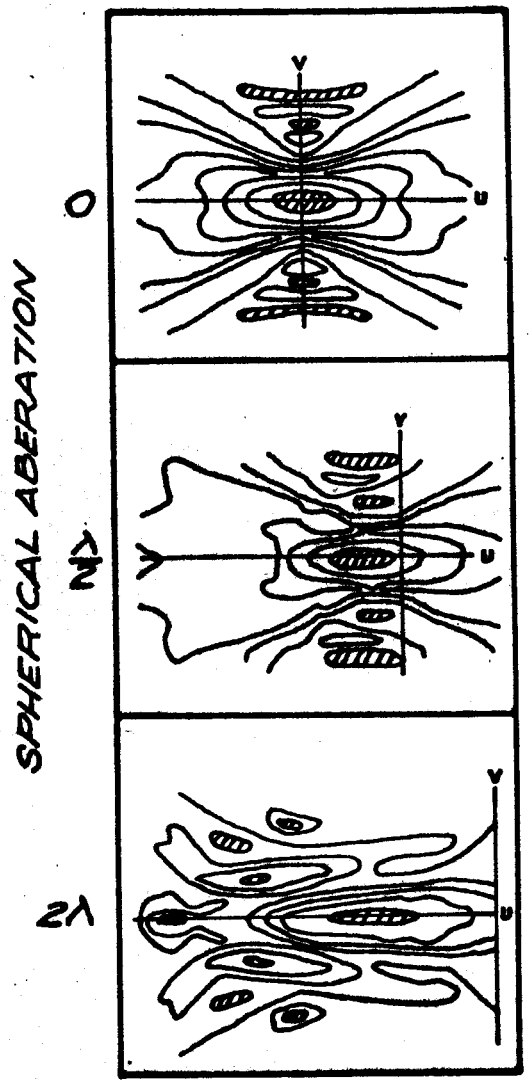

FIG(4.6) INTENSITY CONTOUR DIAGRAMS NEAR THE GEOMETRICAL FOCUS (U=V=0) FOR INCREASING SPHERICAL ABERRATION. (AFTER INNES AND BLOOM[102])

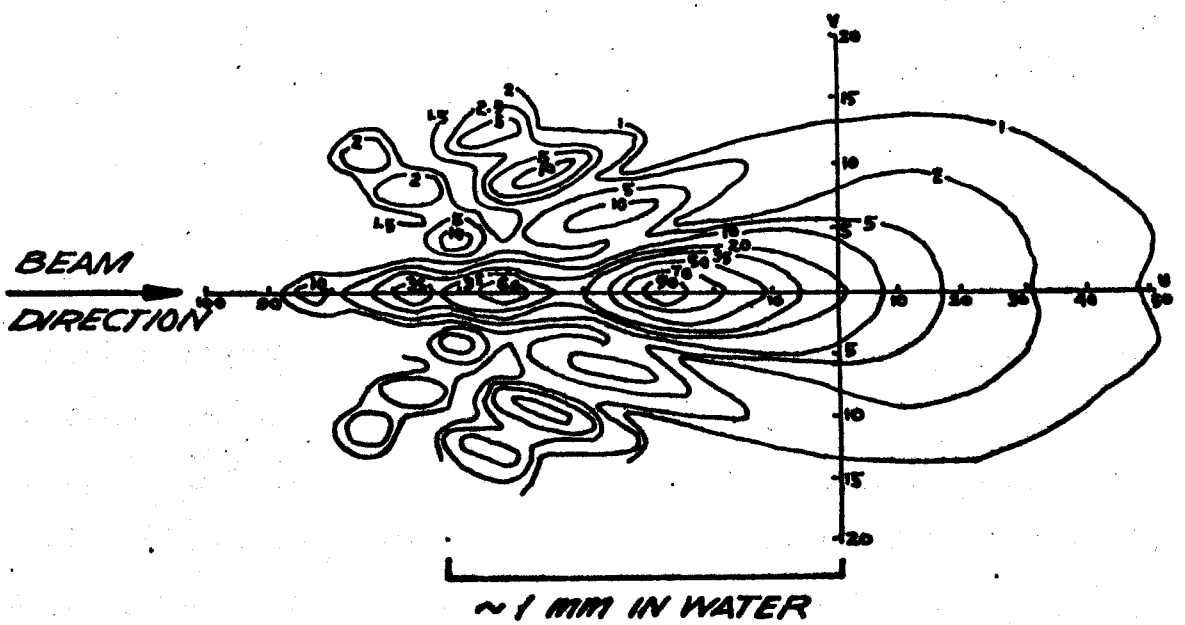

FIG (4.7) LINES OF CONSTANT INTENSITY IN THE FOCAL REGION OF A 5 CM. FOCAL LENGTH f/5 LENS, FOCUSED IN WATER. (AFTER EVANS AND MORGAN[47])

is approximately 0.4mm in close agreement with the spacing in the photographs of Fig. (4-5). Detailed calculations by Evans and Morgan show that the separation between maxima is relatively insensitive to the laser beam radius on the lens. For short focal length lenses the number of maxima does not increase significantly, however the ratio of intensities at adjacent maxima decreases more slowly than for longer focal lengths. As the laser beam intensity is increased above the breakdown threshold value, intensity levels will be reached where the next adjacent maximum will exceed the breakdown threshold, and two breakdown regions will occur. The second breakdown region will occur later in time however. For further increases in laser power more of the maxima occurring along the optic axis will be raised above the breakdown threshold as depicted in Fig. (4-7) and photographed in Fig. (4-5). The number of discrete breakdown points occurring will depend upon (1) the total amount of spherical aberration occurring (2) the focal length of the lens and (3) the amount by which the breakdown threshold intensity is exceeded.

In an earlier publication[19] we assumed this backward motion of the plasma was caused by strong absorption in a dense plasma of approximately 10^{20} electrons/cm^3. However the fast detector measurements of the beam transmitted through the breakdown region reported in the previous section do not uphold this contention. Further, as will be shown in the following section, that fraction of the incident beam which appears to

have been absorbed (~50%) in Fig. (4-4) was depleted due to stimulated Brillouin scattering, in the backward direction. Thus the model proposed by Evans and Morgan[47] appears to qualitatively describe the appearance of the discrete breakdown points observed.

4-5 Stimulated Brillouin Scattering

The apparatus described in section (4-2) and Fig. (4-1) was used to measure the incident, "reflected", and transmitted laser power as a function of input laser power. The 5cm lens used to focus the laser for the experiment of section (4-4) was located 1cm in front of the water cell. Below about 3MW, the transmitted peak power (P_T) increased linearly with increasing incident laser power (P_L) and $P_T \simeq P_L$ after accounting for reflection losses in the lenses and cell windows. A reflected beam (P_R) did not occur below 3MW. Above 3MW the reflected beam appeared and increased rapidly in intensity until the laser power exceeded 5MW. With further increases in laser power the reflected beam increased linearly up to a maximum value of $P_R/P_L \simeq 50\%$ occurring near the breakdown threshold of 30MW. The relationship $P_T + P_R \simeq P_L$ was approximately valid above 3MW. These results are presented graphically in Fig. (4-8).

When the transmitted beam was measured using the fast biplanar diode and Tektronix 519 oscilloscope, the transmitted intensity showed no increase in attenuation and no pulse

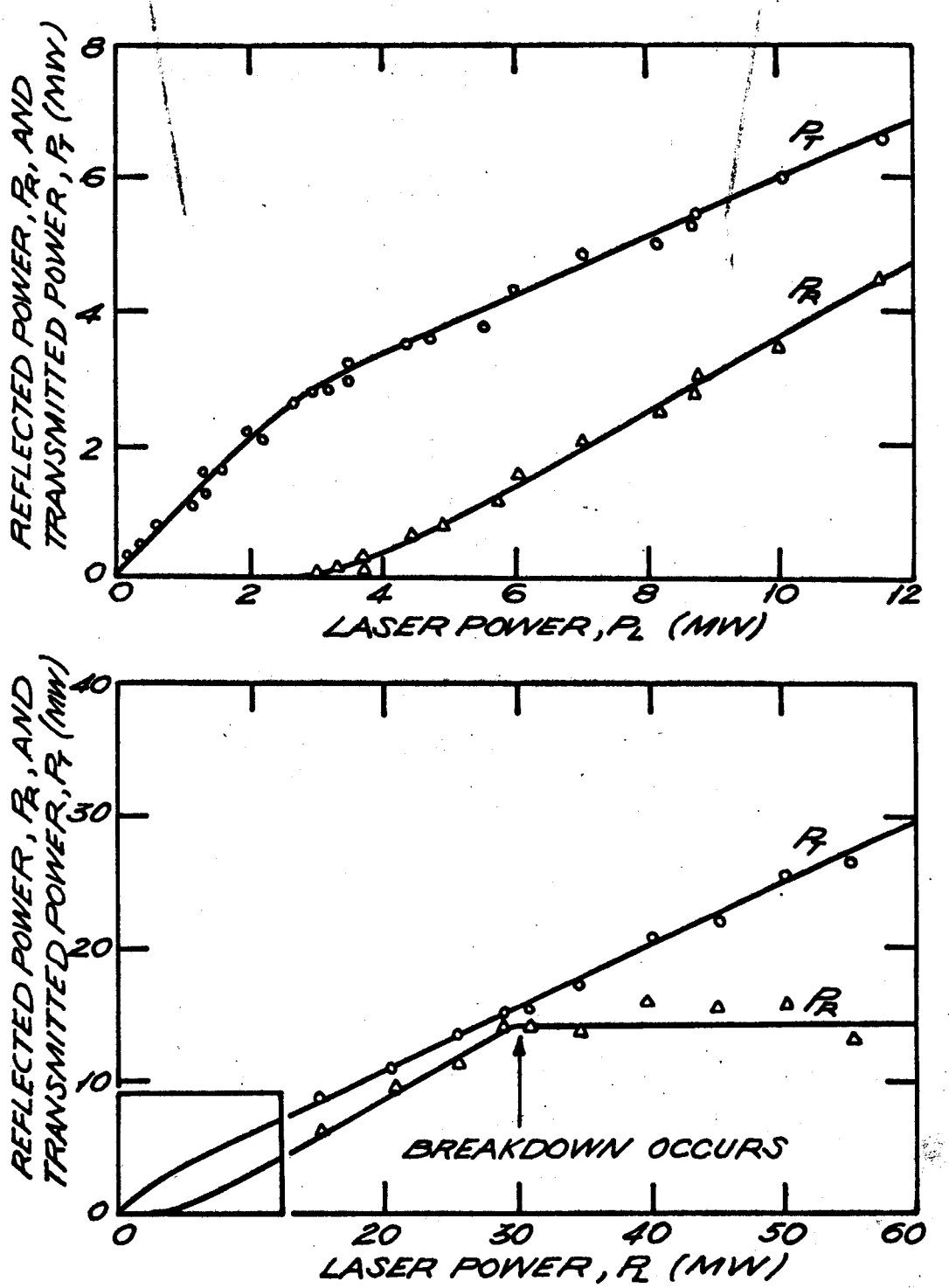

FIG (4.8) INTENSE BACK SCATTERED STIMULATED BRILLOUIN LIGHT.

shaping when the laser power was raised to just exceed the breakdown threshold. The attenuation of the laser beam remained fixed at approximately 50% for all powers greater than the 30MW breakdown power.

For powers well above the breakdown threshold of 30MW, deviations exceeding 50% occurred in the amplitudes of both the transmitted power and back-scattered SBS power for a fixed incident laser power. This lack of reproducibility did not occur below the breakdown threshold.

Replacing the diode monitoring the reflected light with a 1cm Fabry-Perot etalon revealed a single Stokes line, shifted by $\Delta\nu = 0.195\text{cm}^{-1}$ from the incident laser line, characteristic of stimulated Brillouin scattering (SBS) in water[59]. This Stokes shifted line only occurred for laser powers greater than 3MW focused with the 5cm lens. With the optical isolator removed and incident laser power of 20MW, as many as three SBS components occurred due to reamplification of the back scattered SBS in the laser[48]. The data plotted in Fig. (4-8) were taken with the optical isolator in place.

Detailed measurements pertaining to intense back-scattered SBS in CS_2 were reported by Maier et al[60] in 1966. More recently Zverev and Martynov[61] reported more than 50% of their incident laser power of 28MW was converted to back-scattered SBS in several liquids and solids, including water.

Thus the "absorption" of the incident laser beam recorded in Fig. (4-4b) when breakdown occurred in water appears to be due mostly to back-scattered SBS.

4-6 Self-trapping Measurements

Alcock et al[9] have proposed a self-trapping model for the initiation of breakdown in air. Sparks were produced in air at atmospheric pressure using a 3MW ruby laser operating in a single axial and spatial mode. A beam stop located behind the focal region blocked the direct (non self-trapped) laser radiation transmitted through it. When self-trapping occurs prior to breakdown, Alcock has shown that the small diameter of the self-trapped filament ($\sim$ 2 microns in air) leads to a large divergence of the transmitted laser pulse allowing as much as 30% of the incident laser beam to get past the beam stop. This occurs because the self-trapped filament is destroyed at a breakdown point allowing the laser light to emerge with the large divergence characteristic of the 2 micron filament diameter.

A careful check for self-trapping occurring in water prior to breakdown was performed. Following the experiments of Alcock an opaque screen was placed between the collimating lens L_2 and the fast detector depicted in Fig. (4-1). The screen was just large enough to block the recollimated laser beam when the liquid attenuator was adjusted to prevent breakdown. The size and location of the beam stop were checked by

replacing the fast detector with a photographic plate and observing if any laser light passed around the perimeter of the beam stop. The beam stop size was selected so that less than 1% of the incident laser light "leaked" around its perimeter allowing accurate centering of the beam stop. Replacing the film with the fast detector it was found that the 519 oscilloscope would not trigger unless the attenuation preceding the fast detector was reduced by more than a factor of 10.

Following this careful alignment, the liquid attenuator was moved from its position in front of focusing lens L_1 to a position behind the beam stop i.e. between the beam stop and the fast detector (or film). Using the full 100MW laser power available, photographs and fast detector traces were recorded to determine if self-trapping had occurred.

The fast detector traces indicated an increase of less than 1% in the intensity of the laser light getting passed the beam stop when breakdown occurred. Photographs were unable to resolve any increase in the divergence of laser light. In contrast, Alcocks photographs behind the beam stop indicated a dramatic increase in the divergence when self-trapping accompanied breakdown in air. However, Alcock points out that the widely diverging "scattered" light was only observed with a laser operating in the lowest order transverse mode.

Further, Korobkin and Serov[62] have shown that breakdown

occurring in the self-focused beam induced with a Q-switched neodymium laser focused in CS_2 always occurred to the right of the focal point for a laser beam originating from the left. The breakdown occurring in water always occurred to the left of the geometrical focus.

Thus we conclude that the discrete breakdown points recorded in Fig. (4-5) did not originate due to self-trapping of the focused laser beam.

CHAPTER 5

SCATTERING CHARACTERISTICS, SPECTRUM AND TEMPERATURE OF THE BREAKDOWN REGION

5-1 Introduction

The discussion in Chapter 4 established the gross features of the laser induced underwater plasma. In this chapter we attempt to determine the scattering and emission characteristics originating from the breakdown plasma and the resulting cavitation of the water.

The laser and the experimental setup described in section (4-2) were used in the experiments reported in this chapter. The measured scattering characteristics of the breakdown region are presented in section (5-2). In section (5-3) the spectrum emitted by the breakdown plasma is presented while in section (5-4) the measured radiance of the plasma and an estimate of its temperature is presented.

A discussion of the measurements presented in the above sections appears in sections (5-5) and (5-6). It is shown that the scattering behaviour of laser induced breakdown underwater reflects the character of the shock wave accompanying breakdown and not the breakdown plasma.

5-2 Scattering Characteristics of the Underwater Spark

Scattering measurements of the laser generated underwater spark were only partially successful in determining useful parameters of the plasma. Simple measurements were performed in which a photodiode preceded by suitable filters was rotated around the plasma in both the horizontal and vertical plane.

The white light emitted by the plasma was measured using a silicon photodiode preceded by 1 cm of concentrated $CuSO_4$ solution (O.D. = 8 at 694.3 nm with passband from 300 nm to 540 nm). The diode was located 10 cm from the breakdown region and subtended a solid angle of 1.5×10^{-2} steradians. The reproducibility of the radiance of the spark measured in this manner was ±20% for different laser firings at fixed laser power. The measured angular distribution of the white light emitted by the plasma was found to be the same in all directions within this ±20% reproducibility. This was true up to the maximum laser power available (100 MW).

The laser light scattered from the focal region was measured by replacing the $CuSO_4$ filter with a narrow bandpass interference centred at 694.3 nm (3 nm FWHM). The measured laser light scattered from the focal volume was highly non-reproducible with deviations in the recorded signal as large as 50% even though the diode was fixed in position and the laser delivered equal pulse amplitudes (±5%) on separate laser firings.

The reproducibility of scattered laser light measurements was improved by locating a 10 cm lens between the diode and the spark so that the image of the spark was magnified 10X and thus just filled the 4 mm diameter acceptance aperture of the silicon diode. This also allowed the diode to be located more than a meter away from the water cell, thereby greatly reducing the intensity of stray scattered light from the water cell walls and windows from reaching the diode. The stray light pickup was reduced also, due to the shallow depth of focus of the lens.

When the diode, lens combination was rotated around the spark in the horizontal plane containing the axis of the focusing lens L_1, the intensity of the scattered laser light measured was approximately the same independent of the scattering angle. The walls of the water cell restricted this angular measurement to $45° \leq \theta \leq 135°$ where θ was measured relative to the direction of propagation. The angular dependence of the scattered laser light intensity was independent of angle in the vertical plane also.

As a check on our measuring technique the water cell was emptied, carefully dried and flushed with a continuous flow of dry nitrogen, at 1 atmosphere pressure. Breakdown was induced inside the cell, and the angular dependence of the laser light scattered from the plasma occurring in nitrogen was measured. In the vertical plane containing the polarization vector, the

scattered laser intensity falls off as $\cos^2\theta$, which is consistent with classical Thomson scattering from free electrons. In the other two mutually perpendicular planes, however, the scattered laser intensity is peaked in the forward direction, with a less intense peak in the backward direction. Young et al[54] have obtained similar results in air breakdown experiments at atmospheric pressure. Parenthetically, we point out that Ahmad et al[101] have shown recently that the anomalously high scattered laser intensity in the forward and backward directions can be attributed to reflection at the refractive index change in the quasi-spherical breakdown plasma boundary. Further, the ratio of the scattered laser power P from the nitrogen breakdown plasma to the incident laser power L, in the horizontal plane with $\theta = 90°$, was $P/L \approx (1.3 \pm .2) \times 10^{-9}$, which when substituted into equation (5-19) in section (5-5) ahead, yields an electron density of approximately $5 \times 10^{19}/cm^3$ in agreement with other workers[2]. The intensity of the laser light scattered from the breakdown region in water with the same geometry yielded the ratio $P/L \approx (2 \pm 1) \times 10^{-7}$.

Thus we conclude that the scattered laser light originates from the breakdown region in water and is not due to background scattering from the water cell.

5-3 Photographic Spectrum

In this section we present data pertaining to the spectrum emitted by the underwater breakdown plasma as recorded on

photographic plates.

The spectrum emitted by the underwater spark was measured using a Spex Industries model 1700-111 3/4 meter Czerny Turner spectrometer. The location of the spectrometer and its associated condensing optics is shown in Fig. (5-1). Two well corrected 10 cm f.l. air-spaced achromats were used to collect and condense the spark radiation on to the spectrometer entrance slit. The light from the spark was collected at approximately f/3 and focused onto the slit at approximately f/7. The acceptance aperture of the spectrometer was f/6.8. Two achromats were required in order to collect the spark radiation efficiently while simultaneously matching the acceptance aperture of the spectrometer. The spark was magnified 1.5X at the entrance slit and the axis of focusing lens L_1 was perpendicular to the slit.

The plate factor of the spectrometer was 10Å/mm in first order and 3.7Å/mm in second order. The spectrum was recorded in first order using Polaroid type 55P/N film as well as Kodak type IN and IF plates, with the entrance slit set to 40 microns and 5 mm high. This slit width was chosen as a compromise between resolution (approximately 0.4Å) and the ability to expose the plates with a single laser firing, with laser power fixed at 35MW. Above 5000Å a Corning 3-72 filter was added in front of the spectrometer to remove second order radiation.

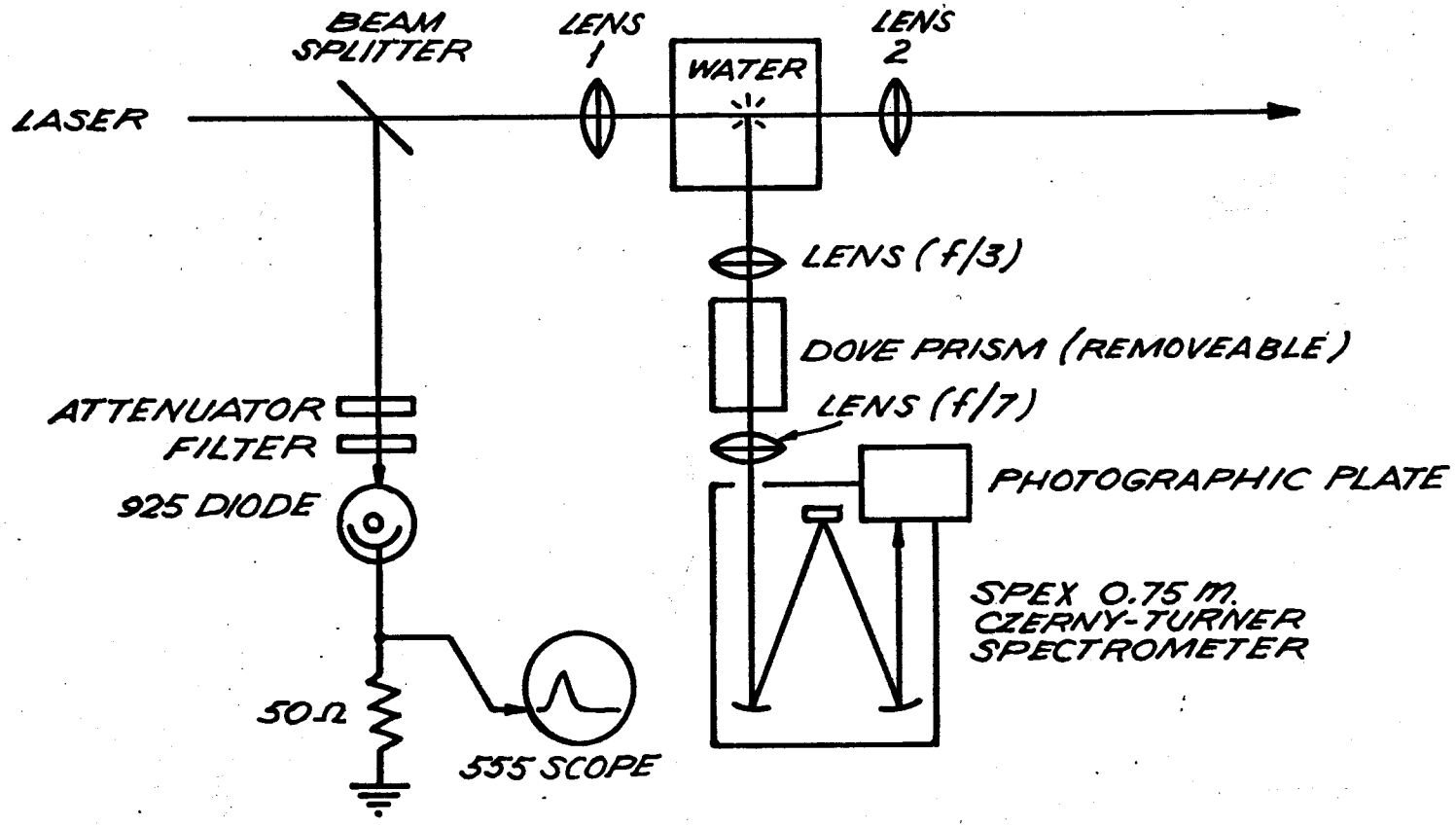

FIG(5.1) APPARATUS TO MEASURE SPECTRUM AND SCATTERED LINEWIDTH OF BREAKDOWN PLASMA.

The data recorded here was taken in the early stages of this study with a less refined laser than reported in Chapter 2. The laser used delivered a single longitudinal mode with a beam divergence of 1.0 mr (half-cone angle) with 30 nsec FWHM. All other parameters of the laser were similar to those reported in Chapter 2.

The wavelength region studied (3800Å to 9500Å) was completely free of any line spectra. The spectrum recorded consisted entirely of a very intense continuum which extends for a maximum height of 0.7 mm on the photographic plate. Since the image on the plate was magnified 1.5X, the spark height was 4.7×10^{-2} cm in close agreement with the photographs of Chapter 4. The absence of line spectra indicates a very high pressure plasma, while the absence of absorption lines indicates an approximately uniform temperature throughout the plasma volume.

Peters[63] has recorded the emission from dense water vapour plasmas. Above 1000 atmospheres pressure this plasma emits a black body like spectrum at a temperature of 12,000°K, completely free from line spectra. Bell and Landt[16] have shown that the shock wave created by the breakdown plasma in water expands with a velocity greater than 4000 m/sec. at least during the first 70 nsec following the onset of breakdown. Using the Rice and Walsh[64] equation of state for water Bell and Landt[16] calculate a pressure behind the shock

exceeding 10^5 atm. Further, Martin[65] has measured the spectrum emitted by the plasma created when a large capacitor is discharged between closely spaced electrodes underwater. The spectrum recorded was completely free from line spectra in the visible region of the spectrum and photoelectric measurements of the plasma yielded a maximum temperature calculated from an assumed blackbody like emission, of 30,000°K. In the next section we will show that the measured temperature of the laser induced breakdown plasma reported here has a blackbody temperature of 15,000°K.

The spectrum does show the scattered laser line near 6943Å. The height of the laser line on the photographic plate was approximately 1.5 mm and extended an equal distance either side of the continuum (height, 0.7 mm). Thus the laser light was probably scattered by the shock front resulting from the breakdown plasma.

If the laser light was scattered from the rapidly expanding shock wave, a blue Doppler shift should occur. To determine if such a Doppler shift occurred the spectrometer was operated in second order and the entrance slit was preceded by a Corning 2-64 glass filter. The slit height remained at 5 mm but the slit width was reduced to 20 microns. In second order the linear dispersion at 7000Å was 3.56Å/mm which with 20 micron slits yields a theoretical resolution of 0.075Å. However this resolution would require the film to resolve

$10^3/20$ = 50 lines/mm. For the films and development procedure used the experimental resolution was determined to be 30 lines/mm. thereby reducing the resolution to approximately 0.12Å. The laser light scattered by the shock wave was found to be shifted by 0.36Å ± 0.06Å towards the blue, when compared to the laser light scattered by a ground glass replacing the water cell. To within the 0.12Å resolution of the spectrometer, the linewidth of the scattered laser radiation was no greater than that of the laser beam itself.

5-4 Radiation Emitted from the Underwater Plasma

It was established in section (5-2) that the "white-light" emitted by the breakdown plasma was the same in all directions, within the ±20% reproducibility for separate laser firings. The isotropic nature of this white light emission allows for simple measurements of the radiance of the plasma without concern for angular corrections.

A 0.25 meter Model 82-410 Jarrell-Ash Ebert mounted grating spectrometer in conjunction with an EMI 6256B photomuliplier was used to detect the plasma radiation as shown in Fig. (5-2). The spectrometer had a linear dispersion of 33 nm/cm leading to a 0.5 nm bandpass with 100 micron slits. Two gratings were available, blazed at 300 nm and 600 nm. All spectra were recorded in first order. Above 500 nm a Corning 3-72 filter was added in front of the entrance slit to eliminate higher order radiation. In some cases, especially near the laser

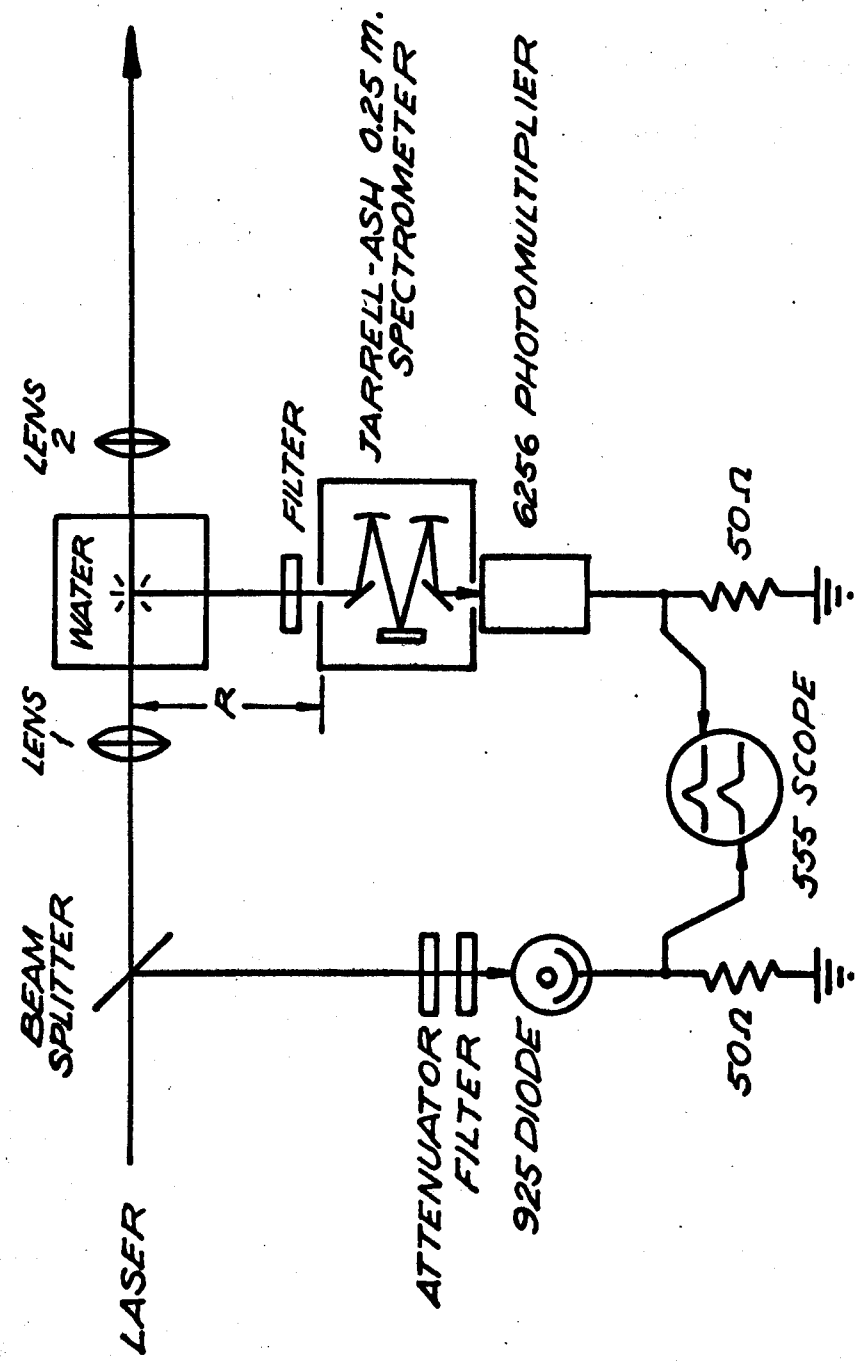

FIG(5.2) APPARATUS TO MEASURE RADIANCE AND SURFACE TEMPERATURE OF BREAKDOWN PLASMA.

wavelength the spectrometer entrance slit was preceded by a narrowband interference filter to decrease the scattered light occurring in the spectrometer.

The laser power was held constant at 35MW and the spectrum was scanned between 400 and 900 nm. An RCA 7102 PM (S-1 photocathode) replaced the EMI 6256B above 600 nm.

The calibration procedure used for the radiance measurements is described in Appendix C. Using (C-7) from Appendix C we find the measured radiance $P(\lambda_1)$ measured at wavelength λ_1 is given by

$$P(\lambda_1) = \frac{V_p}{V_c} J(\lambda_1) \qquad \text{Watts/cm}^2\text{-nm}$$

where V_p = pulsed voltage signal measured on the oscilloscope due to the plasma emission, V_c = the calibration voltage measured using a standard spectal source which emits $J(\lambda_1)$ Watts/cm^2 - nm. For further details see Appendix C.

The photographs of Fig. (4-5) indicate that the plasma was composed of one or several approximately spherical plasma regions depending upon the incident laser power. If each sphere is assumed to emit $W(\lambda_1)$ Watt/cm^2 - nm and if the distance R from plasma to the spectrometer entrance slit is

large compared to the plasma radius r, then the radiance detected at the slit is given by[53,66]

$$P(\lambda_1) = \frac{\pi r^2}{R^2} W(\lambda_1) \qquad W/cm^2\text{-}nm$$

If N plasma regions emit independently with average peak power $\overline{W}(\lambda_1)$, we multiply the right hand side of this equation by N. Thus the radiance of the plasma is given by,

$$\overline{W}(\lambda_1) = P(\lambda_1)\frac{R^2}{N\pi r^2} = J(\lambda_1)\frac{V_p}{V_c}\frac{R^2}{N\pi r^2} \qquad W/cm^2\text{-}nm$$

All the parameters on the right hand side of this equation are accurately known except r and N. The values of r and N depend on the laser power used. From photographs like Fig. (4-5), r was determined to have an average value $\overline{r} = (2.5 \pm 0.2) \times 10^{-2}$cm for the 35MW laser power used. The value of N increased as the laser power was increased.

The peak plasma emission recorded on the Tektronix 555 oscilloscope was reproducible within ±20% for fixed wavelength but separate laser firings.

The results plotted in Fig. (5-3) were recorded using a laser power of 35MW for which N = 1. The solid curve corresponds to an ideal black body at temperature T = 15,000°K, that is we assume

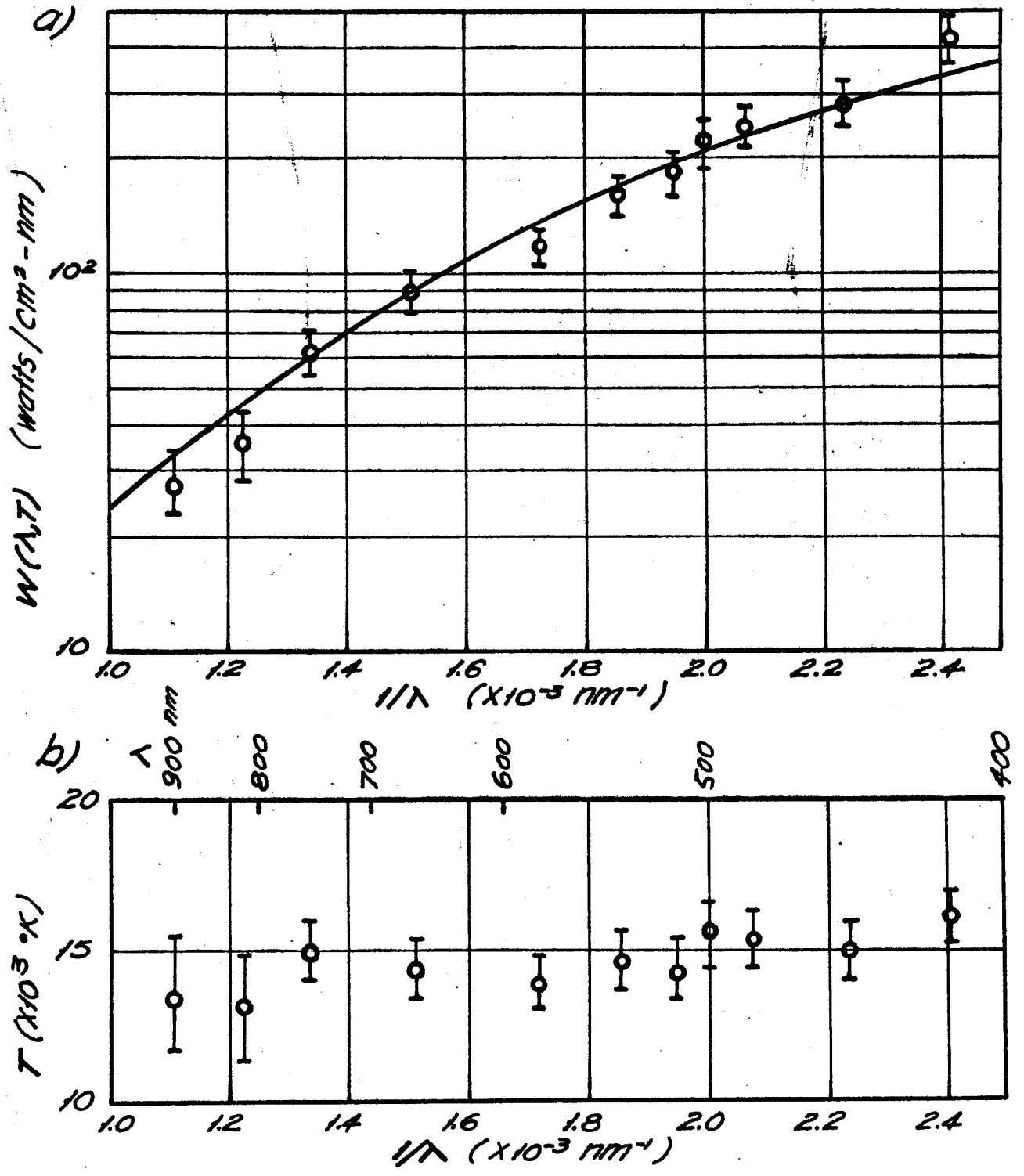

FIG (5.3) PLASMA RADIANCE vs. RECIPROCAL WAVELENGTH OF UNDERWATER PLASMA, a), SHOWING CURVE FOR AN IDEAL BLACK BODY AT T=15,000 °K; AND PLASMA TEMPERATURE, b), CALCULATED FROM RADIANCE ASSUMING AN IDEAL BLACK BODY.

$$\overline{W}(\lambda,1) \Longrightarrow W(\lambda,T) = \frac{2\pi hc^2}{\lambda^5} \frac{1}{\exp(hc/k\lambda T) - 1} \qquad (5\text{-}1)$$

or

$$W(\lambda,T) = \frac{C_1 \lambda^{-5}}{\exp(C_2/\lambda T) - 1}$$

where

$$C_1 = 3.74 \times 10^{16} \quad (\text{Watts}/\text{cm}^2)(\text{nm})^4$$

$$C_2 = 1.438 \times 10^7 \quad \text{nm} - {}^\circ\text{K}$$

This equation applies strictly to a diffuse black body radiator with an emissivity of unity. Monochromatic black body temperatures were calculated using the Planck function of (5-1). Gregg and Thomas[67] have shown that for laser induced plasmas, temperatures calculated using (5-1) yield values

$$T(\lambda) < T_{max}$$

where T_{max} is the maximum temperature in the plasma volume. Thus there is a point in the plasma at which the temperature is at least as high as any monochromatic temperature calculated using the observed emission intensity in (5-1). The observed intensities $\overline{W}(\lambda)$ and the calculated temperatures $T(\lambda)$ are plotted as a function of reciprocal wavelength in Fig. (5-3). The error bars indicate the spread in measured values $\overline{W}(\lambda)$ from shot-to-shot.

The calculated temperature appears to decrease slightly with increasing wavelength. If we assume radiation within the

plasma is reabsorbed via inverse bremsstrahlung this result is not surprising. The absorption coefficient for inverse bremsstrahlung is proportional to the wavelength squared. Further, the temperature gradient near the plasma surface is extremely steep, implying that the detected radiation at the longer wavelengths (~ 800nm) may have originated from a region near the cooler plasma surface. The shorter wavelength radiation (~ 400nm) will be less strongly absorbed and will originate from deeper within the plasma core.

This approximately constant temperature as a function of wavelength is a further indication that the plasma electron density is less than $10^{19}/cm^3$. The monochromatic black body temperatures determined by Gregg and Thomas[67] for dense plasmas induced at the surfaces of beryllium and lead targets show a strong temperature dependence on wavelength, with a factor of 2 difference in the temperatures calculated at 400nm and 800nm.

Finally radiance measurements at higher laser powers were attempted but the reproducibility is poorer due to the larger number of plasma regions (N = 6 at 100MW) - see Fig. (4-5) - each of which displays a variation in $\bar{r}$ of $\sim\pm$ 8%. However the measurements indicated slightly higher temperatures with increasing laser power which at 100MW incident power was T = 21,000°K ± 4000°K.

For comparison purposes we note that Peters[63] has

measured the radiance of a dense water vapour plasma operated at 1000 atm pressure. This plasma emits a blackbody like spectrum at a temperature of 12,000°K completely free from line spectra. Martin[65] has measured the spectrum emitted by the plasma created when 1800 Joules is discharged between electrodes spaced by 2mm underwater. The spectrum recorded was completely free from line spectra in the visible region of the spectrum and photoelectric measurements of the plasma yielded a temperature of 30,000°K.

5-5 Plasma Scattering

In this section we outline the theory used to discuss the scattering characteristics of a fully ionized plasma. We then apply this theory to the observations of the previous sections. It is shown that the scattering properties of the underwater breakdown region are not consistent with a plasma scattering model and in the next section we show the scattering is explained assuming the laser light is scattered from the rapidly expanding shock front.

It is well known that the scattered radiation field from a single stationary electron excited by an incident plane wave is given by[68]

$$\vec{E}_s = \frac{1}{4\pi\epsilon_0}\cdot\frac{e^2}{mc^2}\cdot\frac{1}{R}\left(\hat{q}\times\left(\hat{q}\times\frac{\vec{E}_0}{|E_0|}\right)\right) \qquad (5\text{-}2)$$

where $\hat{q}$ is a unit vector in the direction of propagation as shown in Fig. (5-4). The amplitude of this scattered field can be written as

$$E_s = \frac{r_o}{R} E_o \sin\psi$$

where r_o is the classical electron radius

$$r_o = \frac{1}{4\pi\varepsilon_o}\frac{e^2}{mc^2} = 2.8\times 10^{-13}\ \text{cm} \qquad (5\text{-}3)$$

The scattering cross-section is obtained by dividing the power scattered into the solid angle $d\Omega$ by the incident flux $\bar{S}_L$

$$d\sigma = \frac{\bar{I}_s r^2 d\Omega}{\bar{S}_L}$$

leading to

$$\sigma_e(\theta_s) = \frac{d\sigma}{d\Omega} = r_o^2 \sin^2\psi = r_o^2\left(1-\sin^2\theta_s\cos^2(\phi_o-\phi)\right) \qquad (5\text{-}4)$$

where the dash over the symbols signifies an appropriate time average. This result is the differential scattering cross-section for a single electron. If the incident light is randomly polarized the result must be averaged over the angle $(\phi_o - \phi)$ and the angular factor in (5-2) is replaced by $(1 + \cos^2\theta_s)/2$. The total scattering cross-section, the so-called Thomson cross-section, is obtained by integrating over the entire solid angle:

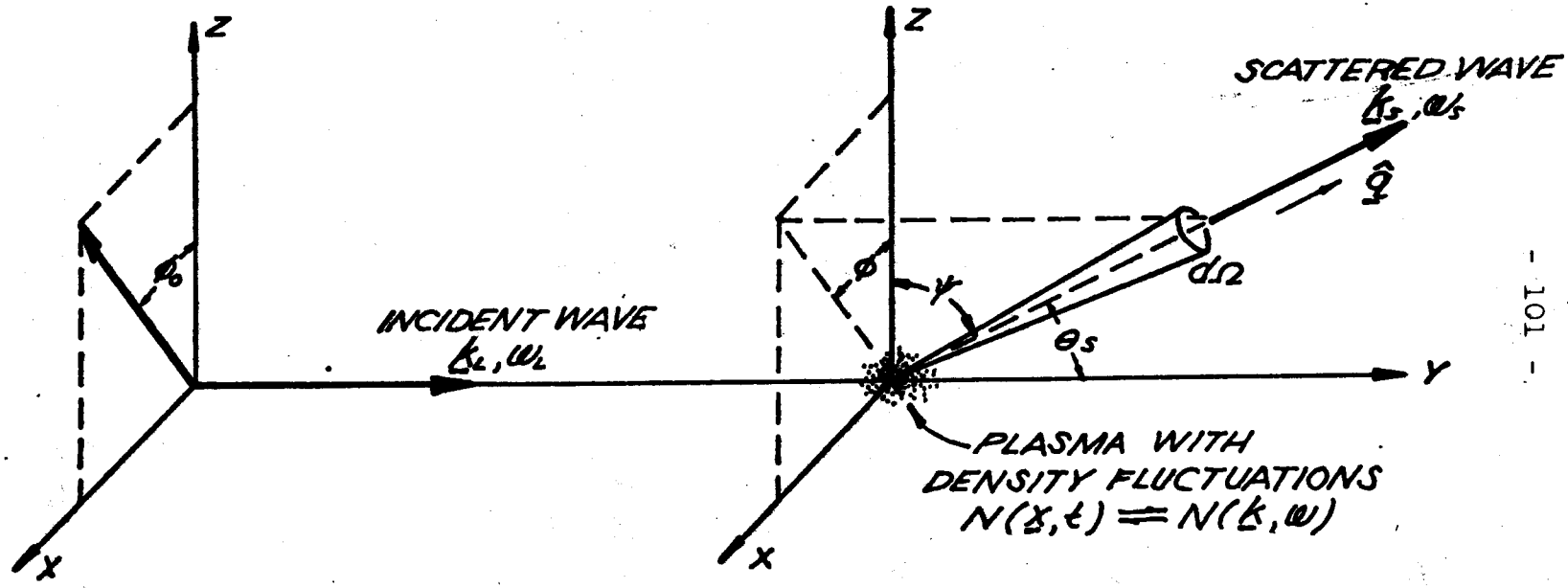

FIG (5.4) GEOMETRY USED TO CALCULATE SCATTERING CHARACTERISTICS OF BREAKDOWN PLASMA.

$$\sigma_T = \frac{8\pi}{3} r_o^2 = 6.65 \times 10^{-25} \quad cm^2 \qquad (5\text{-}5)$$

The mean-free-path for scattering $(n_e\ \sigma_T)^{-1}$ is of the order 10^3 meters for a plasma with an electron density as high as $n_e = 10^{19}/cm^3$. Thus the possibility of multiple scattering in the small volume laser induced plasma is negligible.

The calculations so far apply to a single stationary electron. We now consider the case of scattering of radiation by a fully ionized plasma in volume V. We will consider only scattering from electrons, because (5-2) indicates $E_s \sim 1/m$ and hence scattering from ions will be negligible compared to the contribution from electrons.

Consider N electrons in a volume V divided into a large number of small cells of volume dV_i of such size that the scattered electric fields from one cell arrive at the point of observation with the same phase φ_i. If the mean number of scattering electrons in the cells is $\bar{N}_e$ and the deviation from this mean value in the i-th cell δN_{ei}, the total electric field at the point of observation (neglecting thermal motion of the electrons) is obtained by

$$E_s \sim \sum_i (\bar{N}_e + \delta N_{ei}) e^{-j\varphi_i}$$

Since the number of cells is very large, practically every possible phase is present and the mean component with $\bar{N}_e$

vanishes leaving

$$E_s \sim \sum_i \delta N_{ei} \, e^{-j\varphi_i}$$

This result states the well known fact that scattering can only be observed if there exist deviations from uniformity in the spatial distribution of scattering centres. The scattered intensity (taking a suitable time average) is given by

$$\bar{I}_s \sim \sum_{i,k} \delta N_{ek} \, \delta N_{ei} \, e^{-j(\varphi_k - \varphi_i)} \qquad (5\text{-}6)$$

For the simple case of no correlations between the scattering particles, the fluctuations in the different cells are independent and the above equation reduces to

$$\bar{I}_s \sim \sum_i \overline{(\delta N_{ei})^2} = \sum_i N_{ei} = N \qquad (5\text{-}7)$$

i.e. the total scattering is simply proportional to the total number N of scattering electrons.

The calculations above assume a stationary particle. If the particle is moving with velocity v << c the frequency of the scattered laser light changes by an amount given by the well known Doppler formula

$$\omega = \omega_s - \omega_L = \frac{2\omega_L}{c} v_x \sin\tfrac{1}{2}\theta \qquad (5\text{-}8)$$

where ω is the magnitude of the Doppler frequency shift, ω_s is the frequency of the light scattered from the moving particle and V_x is the component of the velocity along the direction of the wave vector $\vec{k}$ given by

$$\vec{k} = \vec{k_s} - \vec{k_L} \tag{5-9}$$

Further, since $|k_s| \approx |k_L|$ if $v \ll c$ then

$$k \approx 2k_L \sin\tfrac{1}{2}\theta = 2\frac{\omega_L}{c}\sin\tfrac{1}{2}\theta \tag{5-10}$$

as shown in Fig. (5-5). Thus the Doppler shift can be written in the form

$$\omega = \vec{k} \cdot \vec{v}$$

Having shown in the arguments leading to (5-7) that a plasma in which the electrons scatter individually, that we can simply add the intensity contributions of all electrons we define a differential cross-section per unit volume,

$$\frac{d\sigma}{d\Omega} = n_e \sigma_e(\theta_s) \tag{5-11}$$

where n_e is the electron density and σ_e is the Thomson differential cross-section for a single electron, (5-4).

To get the frequency distribution of the scattered radiation it is necessary to add the contributions of all electrons, which have the same velocity component in the direction of the $\vec{k}$ - vector defined in (5-9). Thus the spectrum of the scattered

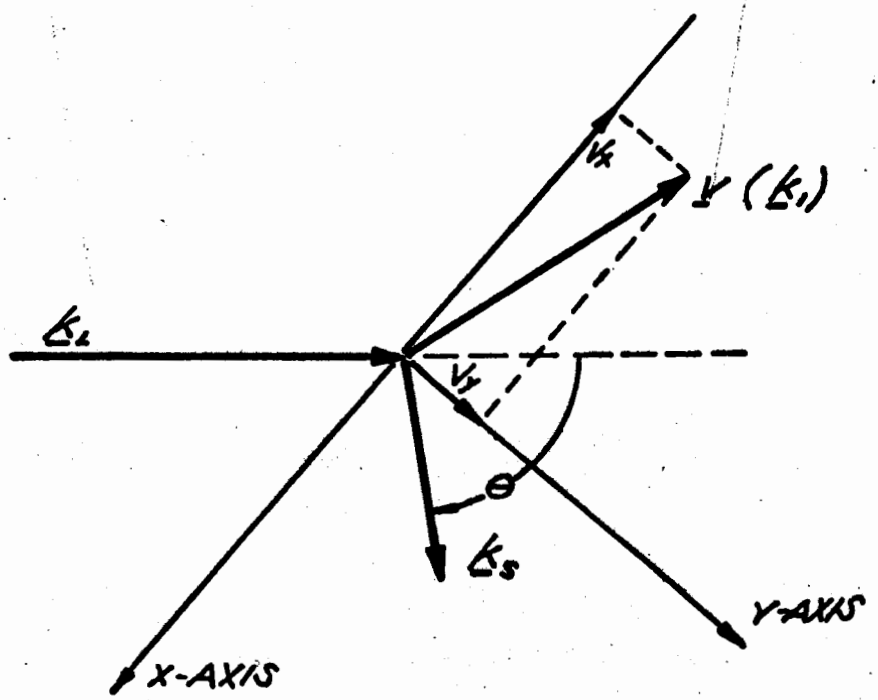

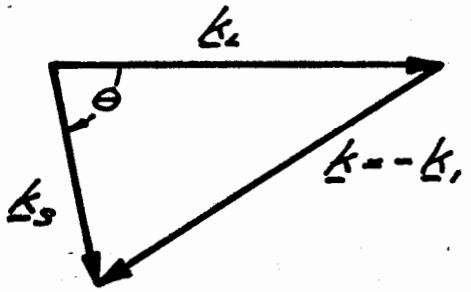

TRIANGLE RELATION BETWEEN THE WAVEVECTORS

FIG (5.5) SCATTERING BY A MOVING ELECTRON.

radiation will be determined by the velocity distribution of the electrons in the direction $\vec{k}$. The usual case considered, is a Maxwellian distribution of velocities in which the electrons are assumed to be in thermal equilibrium at temperature T_e. The Maxwell velocity distribution has the form

$$dn_e = n_e \sqrt{\frac{m}{2\pi K T_e}} \exp\left(-\frac{mv^2}{2KT_e}\right) dv$$

where K is the Boltzmann constant. Using (5-8) we obtain a Gaussian profile for the spectrum $S_T(k,w)$ of the scattered radiation (normalized to the electron density n_e)[68]

$$S_T(\vec{k},\omega)d\omega = n_e \sqrt{\frac{m}{2\pi k^2 K T_e}} \exp\left(-\frac{m\omega^2}{2k^2 K T_e}\right) d\omega \qquad (5\text{-}12)$$

Thus in terms of the differential cross-section per unit volume we write

$$\frac{d^2\sigma}{d\omega\, d\Omega} = \sigma_e\, S_T(\vec{k},\omega) \qquad (5\text{-}13)$$

The total half-width of the spectrum described by (5-12) is given by

$$\Delta\omega_{1/2} = 4\omega_L \sin\tfrac{1}{2}\theta \sqrt{\frac{2KT_e}{mc^2} \ln 2}$$

or converting to units of wavelength

$$\Delta\lambda_{\frac{1}{2}} = 4\lambda_L \sin\tfrac{1}{2}\theta \sqrt{\frac{2KT_e}{mc^2} \ln 2} \qquad (5\text{-}14)$$

Thus we see that the total scattered intensity, found by integrating (5-13) over all frequencies is just (5-11) and hence depends on the total electron density n_e. The spectrum emitted is given by (5-12) and (5-14) and depends only on the temperature T_e and mass m.

The next logical step in the derivations would be to consider the case where correlations between the scattering electrons occur. Simply stated, this means nothing more than putting (5-6) into an appropriate form to yield the desired spectral density function $S(\vec{K},w)$. The details of this solution are long and complex,and as will be shown later are of dubious value when applied to the underwater breakdown plasma.

We have indicated that the scattered spectrum originating from the electrons of a plasma is determined by the spectrum of electron density fluctuations. These density flucturations have been calculated by a number of authors[69-72]. The results obtained apply strictly to collisionless plasmas composed of electrons and a single species of ions.

We now quote the results of the Salpeter theory[69] that are useful in analyzing the experimental data. The spectral distribution of the scattered radiation is discussed by Salpeter using the parameter

$$\alpha = \frac{1}{kL_D} = \frac{\lambda_L}{4\pi L_D \sin\frac{1}{2}\theta} \tag{5-15}$$

where k is defined in (5-10) and L_D is the Debye length defined by

$$L_D = \left(\frac{\epsilon_0 K T_e}{n_e e^2}\right)^{1/2} \tag{5-16}$$

For $\alpha \ll 1$, electron correlations do not exist and the spectrum is described fully by the electron temperature T_e and mass m_e as shown in (5-12) and (5-14). For $\alpha \gg 1$, the spectrum is modified by co-operative interactions between the ions and electrons as described above. The spectrum in this case is composed of a narrow central line, whose width is determined by the Doppler shift for thermal ion velocities, flanked by a pair of satellites corresponding to scattering from longitudinal electrostatic oscillations in the plasma which are displaced from the central ion line by

$$\Delta\lambda = \frac{\omega_p}{2\pi c}\lambda_L^2\left(1 + \frac{3}{\alpha^2}\right)^{1/2} \tag{5-17}$$

where

$$\omega_p = \left(\frac{n_e e^2}{\epsilon_0 m_e}\right)^{1/2} \tag{5-18}$$

is the plasma frequency. For a thermal plasma the intensity

in the satellites is only $1/\alpha^2$ of the total scattered radiation. Further details regarding the line shape $S(\vec{K},w)$ may be found in Salpeters[69] paper or the excellent review article by Kunze[68]..

We now discuss the laser induced underwater plasma in terms of this theory. Using the Salpeter theory[69] the transition from uncorrelated to correlated scattering occurs for $\alpha \sim 1$. Thus using (5-15) in conjunction with (5-16) to (5-18) we find the transition occurs when

$$\frac{n_e}{T_e} \sim 7.8 \times 10^{11} \quad \frac{\text{electrons}}{cm^3 - {}^\circ K}$$

for $\theta = 90°$. Using our measured plasma temperature of 15,000°K we find $n_e \sim 1.17 \times 10^{16}/cm^3$. For electron densities less than this value, correlations do not exist and the scattered laser line should have a Doppler broadened width given by (5-14).

Even for the relatively cool 15,000°K plasma temperature measured in section (5-4) the linewidth would be $\Delta\lambda_{\frac{1}{2}} = 26\text{Å}$. The measured linewidth was less than 0.2A. Thus the narrow scattered laser line could have originated from ion-electron correlations provided $n_e > 10^{16}/cm^3$. However, we will now show that the intensity of the scattered laser light is inconsistent with this assumption.

In terms of the differential scattering across-section we

write for the scattered power

$$P = \frac{d\sigma}{d\Omega} L\, dz\, d\Omega \qquad (5\text{-}19)$$

where L is the laser power in Watts, dz is the interaction length of the laser light in the plasma volume, and $d\Omega$ is the solid angle subtended by the detector at the focal volume. Assuming that scattering occurs due to the electrons in the plasma, then using (5-11) with $\theta_s = 90°$ we write

$$\frac{P}{L} = n_e r_o^2\, dz\, d\Omega$$

The value of $dz \approx 2.5 \times 10^{-2}$cm while the solid angle $d\Omega \approx 1.2 \times 10^{-2}$ and $r_o^2 = 7.95 \times 10^{-26}$ cm^2. Thus for electron scattering we find

$$\frac{P}{L} = 2.4 \times 10^{-29} n_e \qquad (5\text{-}20)$$

The fraction P/L was measured as $(2 \pm 1) \times 10^{-7}$ leading to an electron density $n_e \sim 10^{22}$cm^3. This extremely high electron density is not realistic for the following reasons.

1. For radiation to penetrate a plasma its frequency must exceed the plasma frequency given by

$$\omega_p = \left(\frac{n_e e^2}{\epsilon_o m}\right)^{1/2}$$

or

$$\frac{\omega_p}{2\pi}[Hz] = 8979\left(n_e[cm^{-3}]\right)^{1/2}$$

The laser frequency is $\omega_p/2\pi = 4.32 \times 10^{14}$Hz leading to a critical electron density $n_c = 2.58 \times 10^{21}/cm^3$. Thus for electron densities exceeding this figure the laser radiation would be unable to penetrate the plasma. In fact, microwave measurements of low electron density plasmas indicate a significant attenuation of the incident radiation for densities exceeding $n_c/5$.

2. The number density of water molecules in the focal volume prior to breakdown is $3.3 \times 10^{22}/cm^3$. Thus the calculated $n_e \sim 10^{22}/cm^3$ implies almost total ionization of the water in the focal volume. Martin(65) has measured the electron density in an underwater spark generated by discharging 1800 Joules between electrodes spaced by 2mm. The electron density at the peak of this high energy discharge was $4.5 \times 10^{20}/cm^3$ and the ionization level never exceeded 30%. Even if the total energy of our 100MW laser pulse was absorbed the energy available is less than 2 Joules. The absorption data of Chapter 4 implies the energy absorbed is very much less than 1 Joule.

3. Ramsden and Davies(73) have shown that for laser induced air sparks over 50% of the incident laser energy was absorbed in the focal volume. The electron density in this case was $5 \times 10^{19}/cm^3$. From the absorption measurements of

section (4-3) it is doubtful whether the electron density occurring in the underwater plasma reaches these high concentrations required for strong absorption. This may also be shown theoretically as follows: Spitzer[74] has shown that for a fully ionized plasma, optical radiation will be absorbed via the inverse bremsstrahlung process. That is, the free electrons in the vicinity of an ion or atom absorb energy from the electromagnetic field of the incident radiation with the consequent increase in energy of the electron and a corresponding decrease in the energy of the field. The exponential absorption coefficient derived by Spitzer is given by

$$K = \frac{4}{3}\left(\frac{2\pi}{3mKT_e}\right)^{1/2} \frac{Z^2 e^6}{hcm\nu^3} n_e n_i g\left[1 - e^{-h\nu/KT_e}\right] \quad (5\text{-}21)$$

$$= 3.69\times10^{8} \frac{Z^2 n_e n_i}{T_e^{1/2}\nu^3} g\left[1 - e^{-h\nu/KT_e}\right] \quad cm^{-1}$$

where $n_e(n_i)$ is the electron (ion) density in cm^{-3}, ν is the frequency in Hz, Z is the ionic charge, g is the Gaunt factor and T_e the electron temperature. The requirement for strong absorption of the laser energy is that $Kdz > 1$ in the equation

$$dP(z) = -P(0)\,K\,dz$$

Assuming single ionization and setting the Gaunt factor equal to unity we find that the electron density requirement for strong absorption of the laser beam is

$$n_e > 5.3\times10^{18}(dz)^{-1/2}$$

for the relatively "cool" electron temperature of 1eV (11, 600°K). Thus the electron density in a plasma region with $dz = 4 \times 10^{-2}$cm must exceed $2.7 \times 10^{19}/cm^3$ for strong absorption to occur. Thus an electron density $n_e > 10^{19}/cm^3$ would strongly absorb the ramaining portion of the laser pulse after breakdown had occurred, in agreement with the experimental results of Ramsden and Davies[73]. This strong absorption was not observed in underwater sparks. (See section (4-3)).

4. Finally the image of the laser line on the photographic plate extends well beyond the continuum emitted by the plasma. We will show in the next section that this result together with the intensity and frequency shift of the scattered laser line is consistent with the assumption that the laser light is scattered by the rapidly expanding shock wave.

5-6 Shock Wave Scattering

We now show that the data recorded in the preceding sections, regarding the scattering of the laser light from the focal volume, are consistent with the assumption that the laser light was scattered from the shock wave accompanying breakdown rather than directly from the breakdown plasma.

Bell and Landt[16] have shown that the shock wave originating from the cavitation resulting from laser induced breakdown in water has spherical symmetry. We approximate the breakdown plasma as a high intensity point discharge. The spherical shock wave originating from a "point explosion" was

treated originally by Taylor[75]. The results below are taken from Zel'dovich and Raizer[76]. The approach followed by Taylor was to use dimensional analysis to find the so-called similarity variable which involves the known initial state of the explosion i.e. the energy E released and the initial density ρ_o, which is consistent with the equation of motion and the equation of continuity describing the shock wave. The similarity variable is so-called because variables are chosen which "freeze" the motion of the shock. That is, instead of plotting v_r vs. r to see the effect of shock velocity with increasing radius the ratio r/t replaces r. This type of motion in which the distribution of the velocity remains similar in time and changes only as a result of changes in scale is called self-similar. The method of finding the similarity variable appears to be one of trial and error. Zel'dovich and Raizer[76] show that the dimensionless quantity

$$\xi = r\left(\frac{\rho_o}{Et^2}\right)^{1/5} \qquad (5\text{-}22)$$

can serve as the similarity variable adequately describing the spherical shock wave, during its early history.

The shock front is defined by a given value of the independent variable ξ_o. The motion of the wave front defined by the similarity variable (5-22) and ξ_o is given by

$$R(t) = \xi_o\left(\frac{E}{\rho_o}\right)^{1/5} t^{2/5}$$

and

$$\xi = \xi_0 \frac{r}{R}$$

The value of ξ_0 can only be calculated for very special cases such as the ideal gas. Its value is often determined experimentally. The shock variable we are most interested in is the propagation velocity as a function of time

$$v_r = \frac{dR}{dt} = \xi_0 \frac{2}{5}\left(\frac{E}{\rho_0}\right)^{1/5} t^{-3/5} \qquad (5\text{-}23)$$

A rough estimate of the shock velocity is possible from the height of the scattered laser line recorded on the photographic plate of section (5-3). After accounting for the 1.5x magnification the length of the laser line was 1mm.

The data recorded in chapter 4 does not fix the exact moment in time when breakdown occurred. However, since the data reported here was recorded with laser powers exceeding the breakdown threshold by only 10% we may safely assume that breakdown occurred near the peak intensity of the laser pulse. Thus the laser light was scattered for the remaining approximately 30nsec of the pulse duration. The shadow graphs of Bell and Landt[16] indicate a spherical shock front expanding outwards from the plasma. Thus the velocity of the shock averaged over the 30nsec duration of the scattering process is approximately, $\bar{v} = \bar{r}/t = 1.7 \times 10^6$cm/sec.

A more accurate estimate of the initial shock velocity is

possible using the measured Doppler shift of the scattered laser light. In section (5-3) the laser light scattered by the shock wave was found to be shifted in wavelength by 0.36Å ± .06Å averaged over several measurements. The Doppler formula links this blue shift of the laser light to the velocity of the shock wave through the equation

$$\frac{\Delta\lambda}{\lambda} = 2\frac{\bar{v}_r}{c}\sin\frac{1}{2}\theta$$

For the 0.36Å shift measured at $\theta = 90°$ we calculate the average shock velocity $\bar{v}_r = (1.1 \pm 0.2) \times 10^6$cm/sec.

The maximum shock velocity determined by Bell and Landt was 0.7×10^6cm/sec which was measured following a delay of 70nsec after the initiation of the breakdown plasma. We have shown in (5-23) that the velocity of the expanding shock wave is proportional to $t^{-3/5}$. Thus two velocities v_1 and v_2 measured at times t_1 and t_2 are related through the equation

$$\frac{v_2}{v_1} = \left(\frac{t_1}{t_2}\right)^{3/5}$$

Substituting $v_1 = 0.7 \times 10^6$cm/sec at $t_1 = 70$nsec and $v_2 = 1.1 \times 10^6$cm/sec at $t_2 = 30$nsec yields $v_1/v_2 = 1.57$ for the left hand side of the equation while $(t_2/t_1)^{3/5} = 1.66$ for the right hand side. The agreement is good.

It was noted in the previous section that the scattered laser intensity was too high by at least three orders of magnitude,

assuming Thomson scattering from the plasma electrons as the scattering mechanism. However, liquid water scatters optical radiation due to Brillouin scattering. Benedek and Greytak[55] have shown that the differential scattering cross-section per unit volume at room temperature for this process is

$$\left(\frac{d\sigma}{d\Omega}\right)_B \simeq 0.8\times10^{-6} \quad cm^{-1}$$

We have shown that the frequency integrated cross-section for Thomson scattering is given by

$$\left(\frac{d\sigma}{d\Omega}\right)_T = 7.95\times10^{-26} n_e \quad cm^{-1}$$

Thus an electron density of $n_e \sim 10^{19}/cm^3$ is required to equal the scattering strength originating in the Brillouin scattering process. The high electron density would cause strong absorption of the laser beam as observed by Ramsden and Davies[73] in air. This strong absorption was not observed in water.

The intensity of the laser light scattered from the focal volume was measured with the laser intensity reduced below the breakdown threshold, then the measurement was repeated with the laser intensity raised to just exceed the breakdown threshold. The scattered power is again given by

$$P = \frac{d\sigma}{d\Omega} L\, dz\, d\Omega$$

Using the Brillouin scattering cross-section of Benedek and Greytak and substituting the experimental parameters $d\Omega = 1.2 \times 10^{-2}$ and $dz = 4 \times 10^{-2}$cm. yields the theoretical scattered power ratio

$$\frac{P}{L} = 3.8 \times 10^{-9}$$

The measured ratio of P/L below the breakdown threshold was $P/L \approx (7 \pm 2) \times 10^{-9}$. This is in fair agreement with the theoretical value. When the laser power was raised above the breakdown threshold, the scattered laser power increased sharply to $P/L \approx (2 \pm 1) \times 10^{-7}$ as stated previously.

This sharp increase in the scattered laser light is consistent with the previous data of this section which indicates that the scattering originates from the strong shock front accompanying breakdown. Zel'dovich et al.[77] have shown that for water explosively shocked to pressures exceeding 50kbar, the shock front reflects light due to the increased index of refraction occurring in the shock front. The reflectivity was shown to obey Fresnel's reflection equations.

We conclude therefore that the laser light scattered from the focal region during laser induced breakdown in water, was reflected from the rapidly expanding spherical shock front.

CHAPTER 6

CONCLUDING REMARKS

6-1 Summary

In the preceding chapters we have presented a study of the gross features of laser induced breakdown in liquid water. It was hoped that the detailed theories developed to explain breakdown in gases, could be extrapolated to describe the breakdown features in liquids. However, the breakdown phenomena occurring in water had very little in common with breakdown in gases. This was due in part to the competing effects occurring simultaneously with breakdown in liquids such as SBS. These competing effects either do not occur or are very weak in gases, and can be neglected.

Real gases (including air) have been adequately described using the simple ideal gas law for the equation of state[2]. There is no single, simple equation of state, which describes the properties of liquid water at the high pressures occurring during laser induced breakdown. Several empirical equations of state exist but they usually apply over limited pressure ranges and often are presented as tables of measured thermodynamic functions. See for example the Rice and Walsh[64] equation of state.

We can conclude however that the laser induced underwater

breakdown region had the following properties:

1. The breakdown region was composed of several discrete collinear breakdown plasmas located near the geometrical focus of the lens. The number of distinct breakdown plasmas was found to be a function of the laser power used. These observations were found to be adequately explained using a model proposed by Evans and Morgan[47] who calculated the intensity distribution near the geometrical focus, taking into account the effects of spherical aberration introduced by the focusing lens.

2. Each discrete breakdown region yielded an intense white light pulse lasting approximately 40nsec. The radiance of this light pulse was measured spectrographically and found to be a continuum completely free of line spectra in the range of wavelengths, 350nm to 900nm. The continuum emitted like a blackbody with an equivalent temperature of 15,000°K.

3. The cavitation of the water accompanying breakdown resulted in a strong spherical shock wave. Due to the incompressibility of water, this shock wave produced shock velocities exceeding 10^6 cm/sec during the first 100nsec which leads to estimated pressures exceeding 10^5 kbars using the Rice and Walsh[64] equation of state for water. This shock wave carries off most of the internal energy generated in the breakdown region.

4. Absorption measurements of the laser light transmitted through the breakdown plasma indicated an electron density of

less than $10^{18}/cm^3$. That is, little or no absorption of the laser light occurred. Attempts to obtain a more accurate figure for the electron density by measuring the laser light scattered by the plasma region were unsuccessful. This was due to the very short lifetime ($\sim$ 40nsec) of the continuously changing electron density and the fact that the shock front scatters a much larger fraction of the incident laser light than the electrons of the plasma.

6-2 Suggestions for further work

Problems related to laser induced breakdown occurring in water (and probably liquids in general) present several areas for further study. The shock wave and the exceedingly high pressures it induces offers, in the authors opinion, the most interesting area for study. We outline possible problems utilizing the breakdown plasma below:

1. Shock velocity measurements. Accurate measurements of the rapidly expanding shock wave would be possible using a mode locked laser as a Schlieren light source. Alcock and coworkers[78] at the National Research Council in Ottawa have accurately measured the shock velocities occurring during the first hundred nanoseconds following laser induced breakdown in air. Using a mode locked laser as the light source yielded a 400 nsec long train of pulses with individual pulses spaced by 5.5 nsec and having a duration of 5 psec. Thus ten or more shock fronts appear in a single photograph of a single

breakdown region.

When multiple collinear breakdown regions occur as discussed in Chapter 4 it should be possible to determine, at what point in time the breakdown regions occur relative to the appearance of the first breakdown region occurring at the threshold power. This would allow a further check on the aberration theory of Evans and Morgan[47] which predicts a delay of approximately 3 to 10 nsec between the appearance of successive breakdown regions.

Panarella and Savic[79] have derived a theory which should describe the shape and velocity of the shock during its early development. With the accurate shock velocities measured using the method described above this theory could be easily checked.

For times greater than 100 nsec the shock velocity could be measured using a second ruby laser triggered by the laser producing the breakdown. With suitable delays the entire history of the shock wave could be recorded at least until it interacted with the container walls.

2. Equations of State. The intense shock wave generated in the breakdown region could be reshaped, using an acoustic lens, into a plane shock front. Then a second laser triggered by the first laser could be used to measure the SBS scattered by the shocked liquid. The Stokes shift of the back scattered wave is given in this case by[80]

$$\Delta\nu = \frac{2\nu_0}{c}\left[n_2 v_s + (n_2 - n_1)u_s - n_2 u_p\right]$$

instead of the usual formula in an unshocked liquid

$$\Delta\nu = \frac{2\nu_0}{c} n_1 v_s$$

where v_s is the velocity of sound in the unshocked liquid u_s is the velocity of the shock front, u_p is the particle (or "piston") velocity driving the shock (Up < Us) n_1 is the index of refraction of the unshocked liquid and n_2 is the index in the shocked liquid.

This experiment would allow at least the determination of the index of refraction of liquids under high transient pressures. Static measurements are difficult to perform above pressures of 100 kbar. The shocks resulting from breakdown develop pressures exceeding 10^5 kbar.

Preliminary work along these lines has recently been reported[80] using explosive devices to generate the shock wave.

3. Stimulated Brillouin Scattering. The efficient conversion of incident laser light to back scattered SBS has previously been restricted to liquids with exceedingly low threshold powers such as CS_2[60]. This restriction was due to the high thresholds for SBS in other liquids and the onset of breakdown originating on suspended particulate matter occurring before the SBS wave has sufficient laser power to develop.

Using the closed cycle filtering system described in Chapter 3 to cleanse liquids of foreign material it should be possible to study SBS and the nonlinear properties of liquids with small nonlinear coefficients such as water and CCl_4. It may also be possible, at least for focused beams, to observe self-trapping[35] in the so-called non-self-focusing liquids provided breakdown does not occur first.

4. Electron Density Measurements. Alcock and Ramsden[81] described a Mach-Zehnder interferometer, using a Q-switched laser as a light source, used to measure electron densities occurring in the after glow of a laser induced air spark.

It may be possible to adapt this system to measure the electron density occurring in the later stages of the laser induced underwater spark. However the small size of the underwater spark, its very short lifetime and the problems associated with the index change resulting from the shock wave accompanying breakdown may require the use of the very short pulses available from a mode locked laser. This would require selecting a single picosecond pulse[82] at the desired time to probe the plasma. This is a formidable problem.

5. Use of the Plasma as a Light Source. The laser induced underwater spark was shown in Chapter 4 to be very short lived ($\sim$ 40 nsec FWHM). This exceeding intense transient light source could be used to measure optical effects in materials under intense but short lived illumination.

Novak and Windsor[83] have used the laser generated air spark to measure broadband absorption in liquids excited by the same ruby laser which created the spark. Gill and coworkers[84] measured drift mobility in semiconductors under transient excitation of air sparks.

In both cases, a shorter lived, faster risetime light source would have been desirable. The underwater spark fulfills these requirements.

APPENDIX A

LASER OPTICAL FREQUENCY RESONATORS

A-1 Introduction

A Laser optical resonator is, in principle, no different from its low frequency microwave counterpart. However, due to the very short wavelength of a ruby laser ($\lambda \sim 7\mu$), the mode density is very high and given by[85]

$$P(\nu)d\nu = \frac{8\pi}{\lambda^3}\frac{d\nu}{\nu}$$

where $d\nu$ is the frequency bandwidth of the fluorescent line. Thus, the number of modes that fall within the fluorescent linewidth of ruby ($\Delta\nu$ = 333GHz at 300°K) at $\nu = 4.32 \times 10^{14}$ Hz is about 2×10^{10} modes/cm^3. In a closed resonator these modes would have essentially the same Q so that they would interact equally with the atoms of the medium inside the resonator.

The optical resonator is an open resonator i.e. the four "side-walls" have been removed. Such a resonator will discriminate heavily against modes whose energy propagates along directions other than the remaining two "end walls". These end walls are the mirrors of the open optical resonator. Thus, only those modes propagating in a direction essentially normal to the mirrors will have a high Q.

Carrying this microwave analogy one step further it is possible to estimate the longitudinal and transverse frequency differences of the electromagnetic field configurations over the surface of the output mirror. Assuming plane-waves inside a perfect dielectric waveguide of length L and circular cross-section r, waveguide theory predicts that resonant frequencies can be determined from the resonance equation(86)

$$\left(\frac{X_{p\ell}}{r}\right)^2 + \left(\frac{\pi q}{L}\right)^2 = k^2 = \left(\frac{2\pi\nu}{c/n}\right)^2$$

where $X_{p\ell}$ is the ℓth zero of the Bessel function of order p ($TE_{p\ell}$ modes) or its derivature ($TM_{p\ell}$ modes). The longitudinal mode separation in either case is found by setting $\ell = 0$, $p = 0$ and defining $X_{oo} = 0$. Thus the frequency separation between longitudinal (axial) modes $(q + 1)$ and q is

$$\Delta\nu = \frac{c}{2nL} = \frac{c}{2d_{opt.}}$$

where d_{opt} is the optical distance between the laser mirrors. For d_{opt} = 50cm (typical) $\Delta\nu$ = 300MHz. The higher order transverse modes are those modes for which $\ell^2 + p^2 \neq 0$. The first off-axis mode is the TM_{o1} mode. We can calculate the separation of this first off-axis mode from the axial mode for the same large value of q as follows. The axial mode has wave vector

$$k_o^2 = \left(\frac{\pi q}{L}\right)^2$$

while the TM_{01} mode has wave vector

$$k_1^2 = \left(\frac{\pi q}{L}\right)^2 + \left(\frac{X_{01}}{r}\right)^2$$

leading to

$$k_1^2 - k_0^2 = \left(\frac{X_{01}}{r}\right)^2$$

Now assuming $\nu_1 \approx \nu_0$ (i.e. $k_1 \approx k_0$) we may apply the approximation $k_1^2 - k_0^2 \approx 2k_0(k_1 - k_0)$. Then converting to units of frequency,

$$\frac{\nu_1 - \nu_0}{\nu_0} = \frac{1}{2}\left(\frac{X_{01}}{2\pi n}\frac{\lambda}{r}\right)^2$$

where ν_0 is centre frequency of the laser emission.

It will be shown shortly that a typical value of r = 2mm. Setting the derivative of the Bessel function $J_{01}(kr)$ equal to zero at r leads to $X_{01} = 2.405$. Substituting the known parameters for ruby we find for the spacing of the off-axis mode

$$\Delta\nu_{01} = \nu_1 - \nu_0 = 1.23 \text{ MHz}$$

We will show in the next section that the more exact analysis yields very similar but by no means identical results.

A-2 Wave Analysis of Laser Resonator

Theoretical studies of the modes of laser resonators have been made by Fox and Li[22], Boyd and Gordon[87], and Boyd and

Kogelnik[23]. Excellent reviews of these and over 200 other contributions to the theory of laser resonators are those of Kogelnik[88] and Kogelnik and Li[89]. The theoretical outline presented here follows closely the review by Kogelnik and Li[89].

We shall restrict the detailed discussion to the lowest order TEM_{ooq} mode. The derivation of the higher order modes will only be sketched here; however the interested reader will find detailed calculations in references (85), and (22),(87), (88),(89).

By analogy to the waveguide theory outlined in the introduction to the Appendix we can discuss the laser modes in terms of a set of field configurations over the surfaces of the reflectors. Such a field configuration is called a transverse mode if after propagation from one reflector to the other and back, the field returns with the same spatial pattern multiplied by a complex number that gives the total phase shift (imaginary part) and loss (real part) of the round trip. For every such transverse mode there is a sequence of longitudinal modes for which the round trip phase shift is an integral multiple of 2π. Since the waves are nearly plane waves the spacing of longitudinal modes for a given transverse mode is

$$\Delta\nu = \frac{c}{2d_{opt.}}$$

where d_{opt} is the optical distance between the mirrors and c is the vacuum velocity of light.

The problem of finding the transverse modes has been attacked in two ways. The original, and now classic, approach by Fox and Li[22] used the scalar formulation of Huygen's principle[30] to compute the field at one mirror caused by the illumination of the other. The return field configuration is similarly calculated and is then required to match, within a constant, the initial field configuration. The beauty of this technique is that diffraction losses can be "built-into" the resulting integral equation. Further the integral equation can be solved numerically allowing solutions where analytical methods are unavailable and/or fail. The plane parallel optical resonator does not have an analytical solution originating in Maxwells equations and if precise results are required a solution must be found numerically using the methods of Fox and Li[22]. The other method seeks simple solutions to Maxwells equations. These solutions take the form of narrow beams near the optic axis, which are required to have phase fronts with the same radius of curvature as the reflecting surfaces (mirrors). That is the mirrors intersect the beam everywhere perpendicular to the local direction of propagation, thereby ensuring the reflection of the beam back along itself.

Let us consider the simple beam solutions to Maxwells equations. Following any standard text on electromagnetic theory[86] it is known that a field component or potential u of a coherent wave with sinusoidal time dependence $u = u(x,y,z)\, e^{-j\omega t}$ satisfies the scalar wave equation

$$\nabla^2 u + k^2 u = 0 \qquad \text{(A-1)}$$

where, if the medium is lossless, $k = \omega/c = 2\pi/\lambda$ is the propagation constant. Since the deviation of the field component u from a plane wave is small for light travelling in the z-direction one writes[89]

$$u = \psi(x,y,z)\, e^{-jkz} \qquad \text{(A-2)}$$

where ψ is a slowly varying complex function which represents the difference between a laser beam and a plane wave, namely: a non-uniform intensity distribution, expansion of the beam with distance of propagation, curvature of phase front, and other differences discussed below. Inserting (A-2) into (A-1) one obtains

$$\frac{\partial^2 \psi}{\partial x^2} + \frac{\partial^2 \psi}{\partial y^2} - 2jk\frac{\partial \psi}{\partial z} = 0 \qquad \text{(A-3)}$$

where it has been assumed that ψ varies slowly with Z and that its second derivative $\partial^2\psi/\partial z^2 \approx 0$. The differential equation (A-3) has a form similar to the time dependent Schroedinger equation. A solution to (A-3) is[89]

$$\psi = \exp\left[-j\left(P + \frac{k}{2q} r^2\right)\right] \qquad \text{(A-4)}$$

$$r^2 = x^2 + y^2 \qquad \text{(A-5)}$$

The parameter P(z) represents a complex phase shift which is associated with the propagation of the light beam and q(z) is a complex beam parameter which describes the Gaussian variation in intensity with distance r from the optic axis, as well as the curvature of the phase front which is spherical near the axis. If (A-4) is inserted into (A-3) a quadratic in r results and after comparing terms of equal powers of r one obtains the relations

$$q'(z) = 1 \tag{A-6}$$

$$P'(z) = -j/q(z) \tag{A-7}$$

where the prime indicates differentiation with respect to z. The integration of (A-6) yields

$$q_2(z) = q_1(z) + z \tag{A-8}$$

which relates the beam parameter q_2 in one plane (output plane) to parameter q_1 (input plane) separated from the first by a distance z. Compare this result to the radius of curvature of two phase fronts originating from the same point source and separated by a distance z along the optic axis i.e.

$$R_2 = R_1 + z$$

A-3 Fundamental Mode

The intensity of the coherent beam defined by equation (A-4) $I \sim |\psi|^2$ obviously has a Gaussian profile. It is not the only solution to (A-3) but it is the lowest order solution

called the "fundamental mode" as compared to higher order transverse modes to be discussed later. We now consider the fundamental mode in more detail.

It proves convenient to introduce two real beam parameters R and w related to the complex parameter q(z) by[89]

$$\frac{1}{q} = \frac{1}{R} - j\frac{\lambda}{\pi w^2} \qquad \text{(A-9)}$$

(c.f. transformation of a spherical wave with input radius R_1 passing through a lens of focal length f, $\frac{1}{R} = \frac{1}{R_1} - \frac{1}{f}$). When (A-9) is substituted into (A-4) we get

$$\psi = \underbrace{\exp\left[-j\left(P + \frac{kr^2}{2R}\right)\right]}_{(1)} \cdot \underbrace{\exp\left(-r^2/w^2\right)}_{(2)} \qquad \text{(A-10)}$$

The first term above, (1) contains the phase information of the propagating mode while the second term, (2) shows the variation of amplitude with radius r. From what has been said above (see statement following (A-9)) we see that R(z) is the radius of curvature of the wave front that intersects the axis at z and w(z) is a measure of the decrease of the field amplitude E with distance from the axis. This decrease is Gaussian in form as shown in (A-10) and is plotted in Fig. (A-1). Note that when r = w the amplitude falls to 1/e times that on the axis.

The parameter w is often called the beam radius or "spot size" and 2w the beam diameter.

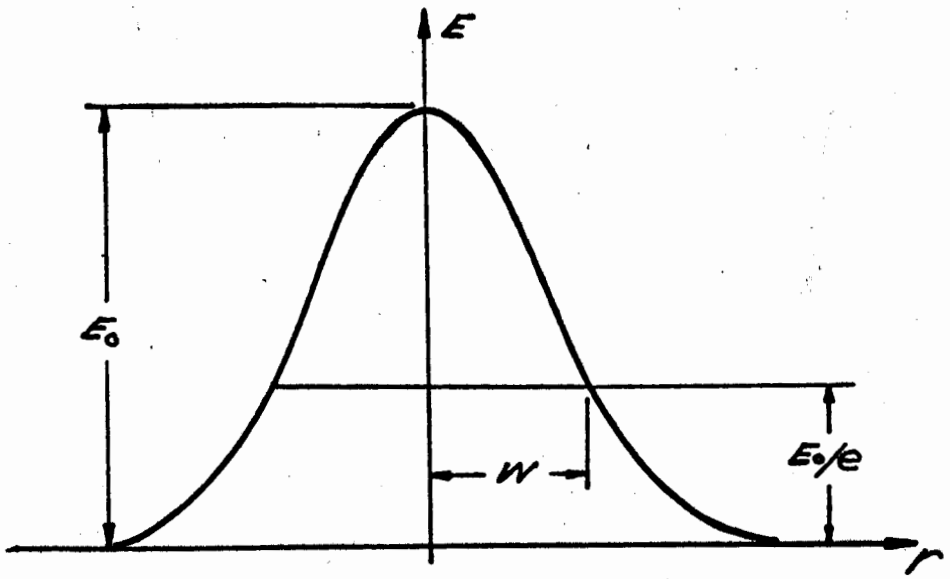

FIG (A.1) AMPLITUDE DISTRIBUTION OF FUNDAMENTAL MODE.

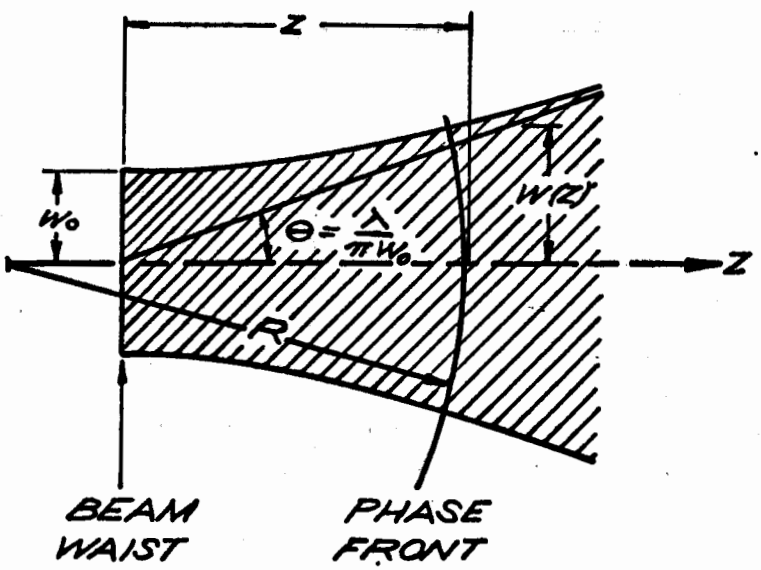

FIG (A.2) CONTOUR OF A GAUSSIAN BEAM.

The Gaussian beam contracts to a minimum diameter $2w_o$ at the beam waist where the phase front is plane. If one measures z from this waist, the expansion laws for the fundamental mode ensue. The complex beam parameter at the beam waist is purely imaginary ($R = \infty$ in (A-9)).

$$q_o = j\frac{\pi w_o^2}{\lambda} = jz_o \tag{A-11}$$

Using (A-8) we can calculate q a distance z away from the waist

$$q = q_o + z = jz_o + z \tag{A-12}$$

Combining (A-12), (A-11) and (A-9) and after equating real and imaginary parts we find

$$w^2(z) = w_o^2\left[1 + \left(\frac{\lambda z}{\pi w_o^2}\right)^2\right] = w_o^2\left[1 + \left(\frac{z}{z_o}\right)^2\right] \tag{A-13}$$

$$R(z) = z\left[1 + \left(\frac{\pi w_o^2}{\lambda z}\right)^2\right] = z\left[1 + \left(\frac{z_o}{z}\right)^2\right] \tag{A-14}$$

Figure (A-2) shows the expansion of the beam according to (A-13). The cross-section of this side view of the beam is of course Gaussian.

The beam contour w(z) is a hyperbola with asymptotes

$$\lim_{z\to\infty} w(z)/z = \frac{\lambda}{\pi w_o} = \tan\theta \tag{A-15}$$

This is the far field half-cone diffraction angle of the fundamental mode.

It is interesting to note that if θ is small

$$\lim_{z\to\infty} 2w(z)/z = \frac{2\lambda}{\pi w_o} = \frac{4}{\pi}\frac{\lambda}{D_o} \simeq 1.27\frac{\lambda}{D_o} \qquad \text{(A-16)}$$

where D_o is the beam diameter of the fundamental mode at the beam waist. Compare this result with the angle of the first minimum in the Airy diffraction pattern of plane waves incident on a circular aperture of diameter D i.e. $\theta_d \simeq 1.22\lambda/D$. A result to be expected since the fundamental mode is a plane wave at the beam waist. The slight difference in the constant is due to the fundamental mode intensity being Gaussian instead of uniform across the "aperture".

To calculate the complex phase shift a distance z away from the waist, one inserts (A-12) into (A-7) to get

$$P'(z) = -j/q = \frac{-j}{z + z_o}$$

Integration of this equation yields

$$jP(z) = \ln\left[1 - j\left(\frac{z}{z_o}\right)\right]$$

and using the identity $a - jb = re^{-j\Phi}$ where $r = a^2 + b^2$ $\Phi = \tan^{-1}(b/a)$ so that $\ell n\, re^{-j\Phi} = \ell n\, r - j\Phi$ we get

$$\begin{aligned} jP(z) &= \ln\sqrt{1+(z/z_o)^2} - j\Phi \\ &= \ln(w/w_o) - j\tan^{-1}(z/z_o) \end{aligned} \qquad \text{(A-17)}$$

The real part of P(z) represents a phase shift difference Φ between the Gaussian beam and an ideal plane wave while the imaginary part produces an amplitude factor (w_o/w) which gives the expected intensity decrease on the axis due to the expansion of the beam. With the results of (A-12) and (A-17) the fundamental Gaussian beam (A-2) can be written

$$u(r,z) = \frac{w_o}{w} \exp\left[-j\left(kz - \Phi\right) - r^2\left(\frac{1}{w^2} + \frac{jk}{2R}\right)\right] \quad \text{(A-18)}$$

$$\Phi = \arctan\left(\frac{\lambda z}{\pi w_o^2}\right) \quad \text{(A-19)}$$

A-4 Higher Order Modes - Cylindrical Geometry

For a laser system with the usual cylindrical symmetry (r,ϕ,z) Boyd and Kogelnik[23] used as a trial solution to (A-3)

$$\psi = g_p\left(\frac{r}{w}\right) \exp\left[-j\left(P + \frac{kr^2}{2q} + l\phi\right)\right] \quad \text{(A-20)}$$

After considerable calculation they found

$$g_p\left(\frac{r}{w}\right) = \left(\sqrt{2}\,\frac{r}{w}\right)^l L_p^l\left(\frac{2r^2}{w^2}\right) \quad \text{(A-21)}$$

where L_p^l is a generalized Laguerre polynomial and p and l are the radial and angular mode numbers. $L_p^l(x)$ obeys the differential equation

$$x\frac{d^2L_p^l}{dx^2} + (l+1-x)\frac{dL_p^l}{dx} + pL_p^l = 0$$

Some polynomials of low order are

$$L_0^{\ell}(x) = 1$$

$$L_1^{\ell}(x) = \ell + 1 + x \qquad \text{(A-22)}$$

$$L_2^{\ell}(x) = \tfrac{1}{2}(\ell+1)(\ell+2) - (\ell+2)x + \tfrac{1}{2}x^2$$

The parameter R(z) in (A-18) is the same for all modes implying that the phase-front curvature is the same and changes in the same way for modes of all orders. This result is due to the requirement that the curved mirror surface must have the same radius of curvature as the beam mode if the beam is to reflect back exactly along itself. The phase shift Φ, however, is a function of the mode numbers

$$\Phi(p,\ell:z) = (2p+\ell+1)\arctan(\lambda z/\pi w_0^2) \qquad \text{(A-23)}$$

Note that this result reduces to (A-19) when p = 0, ℓ = 0 as required.

A-5 Optical Resonators

The most commonly used laser resonators are composed of two spherical (or flat) mirrors or one spherical and one flat mirror, facing each other. If the formulae we have developed are to be useful, we should be able to calculate the beam parameters R and w and the frequency separation of the modes in terms of the known radii of curvature of the mirrors and their separation. The beam parameters R and w can be calculated in terms of the mirror radii $-R_1$ and $+R_2$ using (A-14)

$$-R_1 = z_1 + z_0^2/z_1^2$$

$$+R_2 = z_2 + z_0^2/z_2^2$$

where the sign convention that R(z) is positive if it is convex when viewed from $z = +\infty$ is used.

Solving these equations we get

$$z_1 = -\frac{R_1}{2} \pm \frac{1}{2}\sqrt{R_1^2 - 4z_0^2}$$
$$z_2 = \frac{R_2}{2} \pm \frac{1}{2}\sqrt{R_2^2 - 4z_0^2} \qquad \text{(A-24)}$$

Taking the mirror spacing as $d = Z_2 - Z_1 > 0$ we calculate the beam diameters on the mirrors. $2w_1$ and $2w_2$ are given by

$$w_1^4 = \left(\frac{\lambda R_1}{\pi}\right)^2 \frac{R_2 - d}{R_1 - d} \cdot \frac{d}{R_1 + R_2 - d} \qquad \text{(A-25)}$$

$$w_2^4 = \left(\frac{\lambda R_2}{\pi}\right)^2 \frac{R_1 - d}{R_2 - d} \frac{d}{R_1 + R_2 - d} \qquad \text{(A-26)}$$

Further the diameter of the beam waist $2w_o$ is given by

$$w_o^4 = \left(\frac{\lambda}{\pi}\right)^2 \frac{d(R_1 - d)(R_2 - d)(R_1 + R_2 - d)}{(R_1 + R_2 - 2d)^2} \qquad \text{(A-27)}$$

Finally the very useful beam parameter $z_o = \pi w_o^2/\lambda$ can be determined from this last equation

$$z_o^2 = \frac{d(R_1 - d)(R_2 - d)(R_1 + R_2 - d)}{(R_1 + R_2 - 2d)^2} \qquad \text{(A-28)}$$

Since the signs of R_1 and R_2 were taken care of in deriving equations (A-25) to (A-28) only the magnitudes are substituted to calculate the beam diameters. (See Fig. A-3).

A-6 Resonance Frequencies

The resonance frequencies of the optical resonators are determined by the condition that the phase delay associated with a two-reflection round trip be equal to an integral multiple of 2π. Another way of putting this is that resonance occurs when the phase shift from one mirror to the other is a multiple of π. Taking the mirror positions at $z_1 = -d_1$ and $z_2 = d_2$ and using (A-18) and (A-23) we find

$$\left[kd_2 - \Phi(d_2)\right] - \left[-kd_1 - \Phi(-d_1)\right] = q\pi$$

$$k(d_2+d_1) - (2p+l+1)\left[\tan^{-1}\left(\frac{d_2}{z_0}\right) + \tan^{-1}\left(\frac{d_1}{z_0}\right)\right] = q\pi$$

where $d_1 + d_2 = d$ and q is an integer, $kd = \frac{2\pi d}{\lambda} = \left(\frac{2d}{c}\right)\pi\nu$.

Only two cases interest us here: (1) both mirrors with equal curvature $R >> d$ so that $d_1 = d_2 = d/2$ leading to

$$\Delta\nu = \frac{c}{2d}\left[\Delta q + \frac{2}{\pi}(2\Delta p + \Delta l)\tan^{-1}\left(d/2z_0\right)\right]$$

$$z_0^2 = (2R-d)d/4 \qquad \text{(A-29)}$$

and (2) one plane mirror ($R_2 = \infty$) and one spherical mirror ($R_1 = R$). In this case $w_1 = w_0$ so that $d_2 = 0$ and $d_1 = d$ leading to

$$\Delta\nu = \frac{c}{2d}\left[\Delta q + \frac{1}{\pi}(2\Delta p + \Delta l)\tan^{-1}\left(d/z_0\right)\right]$$

$$z_0^2 = d(R-d) \qquad \text{(A-30)}$$

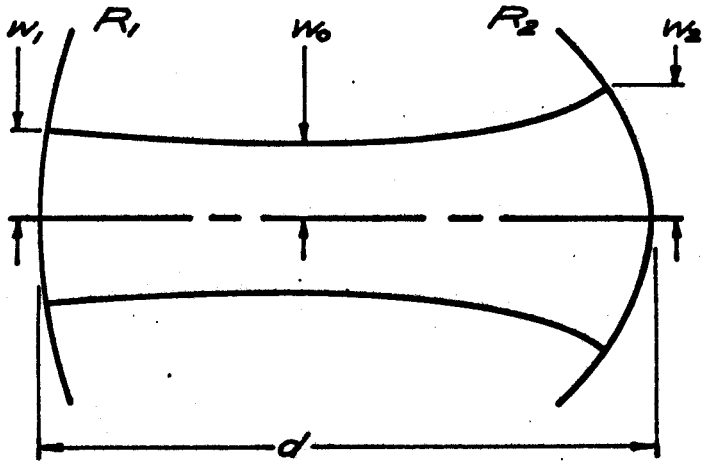

FIG (A.3) AN ASYMMETRIC RESONATOR WITH MIRROR CURVATURES R_1, R_2.

Equations (A-25) to (A-30) constitute the working equations used in determining the beam parameters R, w_o, z_o and frequency separations $\Delta\nu$ on working lasers.

APPENDIX B

$CuSO_4$ AND $NiSO_4$ LASER ATTENUATORS

B-1 Introduction

The attenuation of Q-switched ruby lasers creates problems due to the possibility of irreversible damage to the usual Gelatin and Jena glass-filters. The Jena glass neutral density (N.D.) filters are able to withstand higher power densities than the Gelatin filters but are known to fluoresce at these higher powers.

Two liquids commonly used to attenuate ruby lasers are aqueous solutions of $CuSO_4$ and $NiSO_4$, in quartz or pyrex cells. The advantages of these liquid attenuators are: (1) concentrated solutions have high attenuation with pathlengths of only 1cm; (2) the concentration is quickly and easily adjustable to yield a continuously variable optical denisty from O.D. = 0($T = 100\%$) to O.D. > 20 ($T < 10^{-20}$); (3) both filters pass the blue-green portion of the visible spectrum and $CuSO_4$ passes the optical second harmonic of the ruby laser (347.6 nm) virtually unattenuated; (4) if the liquid should accidently breakdown it is "self-healing".

In this appendix we show the pass-band of these two filters and accurately calibrate their attenuation coefficients at the ruby wavelength of 694.3 nm.

B-2 Theory

In Fig. (B-1) we show the model of the cell-attenuator solution combination assumed in the discussion below. Assuming that only a single pass is made through the attenuator with no multiple reflections, then in passing through the four surfaces shown the transmitted intensity I_T is given in terms of the incident intensity I_0 by

$$\begin{aligned} I_T &= I_0(1-R_1)e^{-\alpha_1 \ell}(1-R_2)e^{-\alpha_2 L}(1-R_2)e^{-\alpha_1 \ell}(1-R_1) \\ &= I_0(1-R_1)^2(1-R_2)^2 e^{-(2\alpha_1 \ell + \alpha_2 L)} \end{aligned} \tag{B-1}$$

$$R_1 = \left(\frac{n_1 - 1}{n_1 + 1}\right)^2 \qquad R_2 = \left(\frac{n_2 - n_1}{n_2 + n_1}\right)^2 \tag{B-2}$$

and we have assumed Beer's Law applies i.e. $I(x) = I(0)_e{}^{-\alpha x}$. The other symbols are clear from the figure. Now, the optical density is defined by the equation

$$O.D. \equiv \log_{10}\frac{I_0}{I_T} = \log_{10}\frac{1}{T} \tag{B-3}$$

where T is the intensity transmission fraction. Thus substituting Eq. (B-1) into Eq. (B-3) yields

$$O.D. = -2\left[\log_{10}(1-R_1) + \log_{10}(1-R_2)\right] + \log_{10}e\left(2\alpha_1 \ell + \alpha_2 L\right) \tag{B-4}$$

The cell faces are either pyrex ($n_1 \simeq 1.475$) or fuzed quartz ($n_1 = 1.457$) and $n_2 \geq 1.331$. The value of n_2 will increase

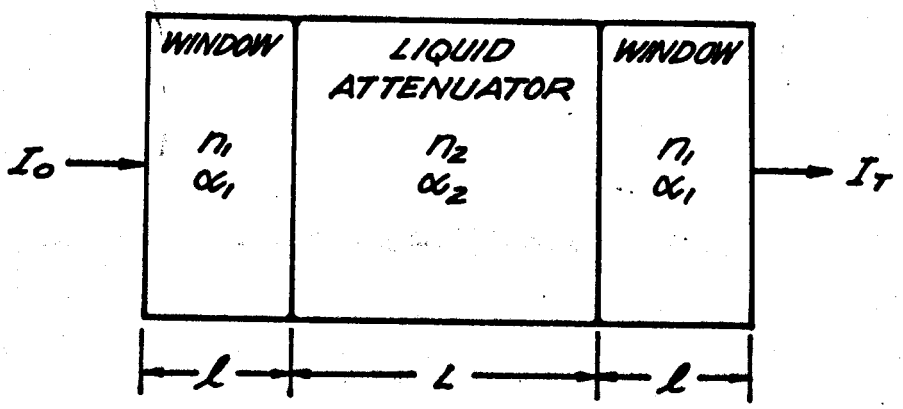

BEER'S LAW : $I(x) = I(0)e^{-\alpha x}$

SINGLE PASS : $I_T = I_0 (1-R_1)^2 (1-R_2)^2 e^{-(2\alpha_1 l + \alpha_2 L)}$

$$R_1 = \left(\frac{n_1 - 1}{n_2 + 1}\right)^2 \qquad R_2 = \left(\frac{n_2 - n_1}{n_2 + n_1}\right)^2$$

FIG (B.1) LIQUID ATTENUATOR MODEL.

as $CuSO_4$ or $NiSO_4$ is dissolved in the water. Using the values of n_1 and n_2 above we find

$$R_1 = 0.0344 \text{ (quartz)} \qquad R_2 \leq 0.00194$$

Substituting into (B-4) we find

$$O.D. = 0.0320 + 0.4342(2\alpha_1 \ell + \alpha_2 L) \qquad \text{(B-5)}$$

The thickness of the pyrex or quartz windows (ℓ) was typically $\ell \leq$ 1mm requiring the α_1 be greater than 0.5 cm^{-1} if $\alpha_1 \ell$ is to contribute significantly to the absorption process. Since α_1 for both fuzed silica and quartz is less than 10^{-3}, $(2\alpha_1 \ell) < 2 \times 10^{-4}$ and hence can be neglected in comparison to $\alpha_2 L$. The working equation for the graphs of the next section is

$$O.D = 0.0304 + 0.4342\alpha_2 L \qquad \text{(B-6)}$$

where the effects of R_2 have been dropped also.

We now consider the possibility of multiple reflections, neglecting the small effect of R_2 and assuming no interference between reflected beams. Setting $e^{-\alpha_2 L} = A$, the fraction R_1 of the incident beam is reflected from the input surface, while the fraction $A(1 - R_1)$ is transmitted through the cell to the second surface. Of this $A(1 - R_1)^2$ escapes (Eq. (B-1)) while the fraction $AR_1(1 - R_1)$ is reflected back toward the input surface. Iteration of this analysis yields the series

$$I_T = I_0 A(1-R_1)^2 \left[1 + A^2 R_1^2 + A^4 R_1^4 + \cdots\right]$$

where the infinite series sums to $(1 - A^2R_1^2)^{-1}$. Substituting for A we find

$$I_T = \frac{I_o(1-R_1)^2 \exp(-\alpha_2 L)}{1 - R_1^2 \exp(-2\alpha_2 L)} \qquad \text{(B-7)}$$

The numerator of this equation is equivalent to Eq. (B-1) with $R_2 = 0$ and $\alpha_1 = 0$. The value of $R_1^2 e^{-2\alpha_2 L} = 0.00121e^{-2\alpha_2 L}$, so that the denominator in Eq. (B-7) lies between the limits,

$$0.9988 \leq (1 - R_1^2 e^{-2\alpha_2 L}) \leq 1$$

Thus the effects of multiple reflections can be neglected and the working equation (B-6) is the form used in the next section.

B-3 Results

The liquid filters were prepared by carefully weighing $CuSO_4 \cdot 5H_2O$ and $NiSO_4 \cdot 6H_2O$ into bottles containing a carefully preweighed volume of water. The bottles were sealed and the more concentrated solutions warmed to promote dissolving of the solid material. After the solutions stood for several hours, measurements were made of (1) the passband in the range of 350.0 nm to 700.0 nm and (2) the O.D. of the solutions at 694.3 nm. The measurements were made on a Cary 14 spectrometer with the solutions in 1mm and 1cm fuzed silica Opticells whose pathlength was known to the nearest .003mm at 20°C. Thus the accuracy was limited by the spectrometer and not the concentration determination or the pathlength accuracy. All data was

taken with the reference beam containing a similar cell filled with distilled water.

The graphs of Fig. (B-2) and (B-3) show the passband converted from units of optical density to the more usual transmission, T vs. wavelength λ(nm) saturated solutions of $CuSO_4$ and $NiSO_4$ in opticells with 1.004 mm pathlength were used. The temperature in the cell compartment of the spectrometer was 21°C.

Optical density (O.D.) vs wavelength in nanometers is plotted in Fig. (B-4) and (B-5) for $CuSO_4$ and $NiSO_4$ respectively at a fixed wavelength of 694.3 nm - the ruby laser emission wavelength. The data shown was collected over a period of eight months and was taken on two different Cary 14 spectrometers. All the data points taken are shown on these plots. A least squares fit was calculated for the two plots together with the standard error of estimate S_{yx} which is plotted as the pair of dashed lines in Figs. (B-4) and (B-5).

The results of these least squares calculations are shown below for $CuSO_4$ (Eq. B-8) and $NiSO_4$ (Eq. B-9)

$$O.D._{Cu} = 0.0114 + 0.0215CL$$

$$S_{yx} = 0.0127 \qquad \text{(B-8)}$$

which includes all the data taken and plotted. The results for $NiSO_4$ showed a deviation from linearty at low optical densities which could be due to either a change in the sign of

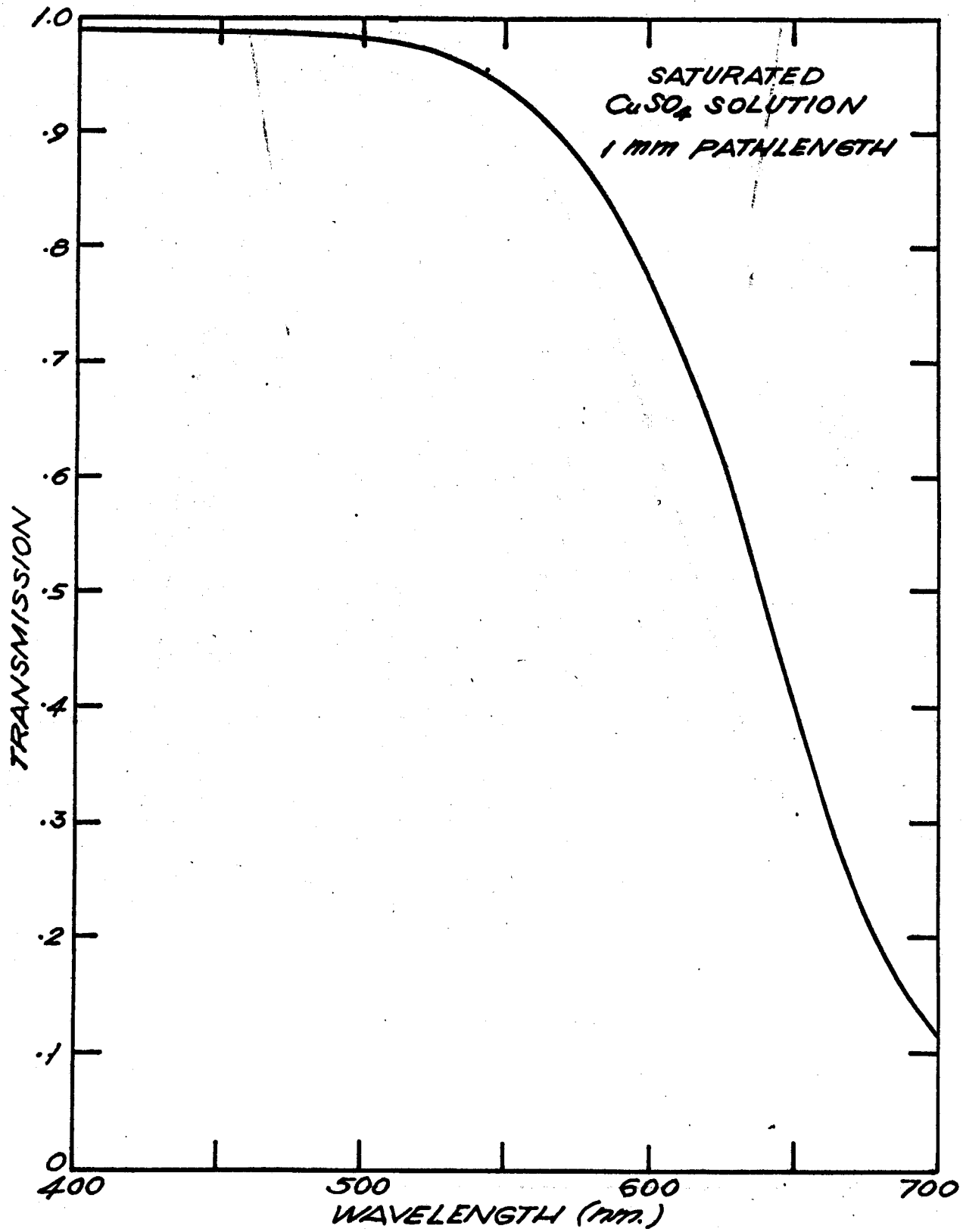

FIG (B.2) TRANSMISSION vs. WAVELENGTH; $CuSO_4$ SOL^N

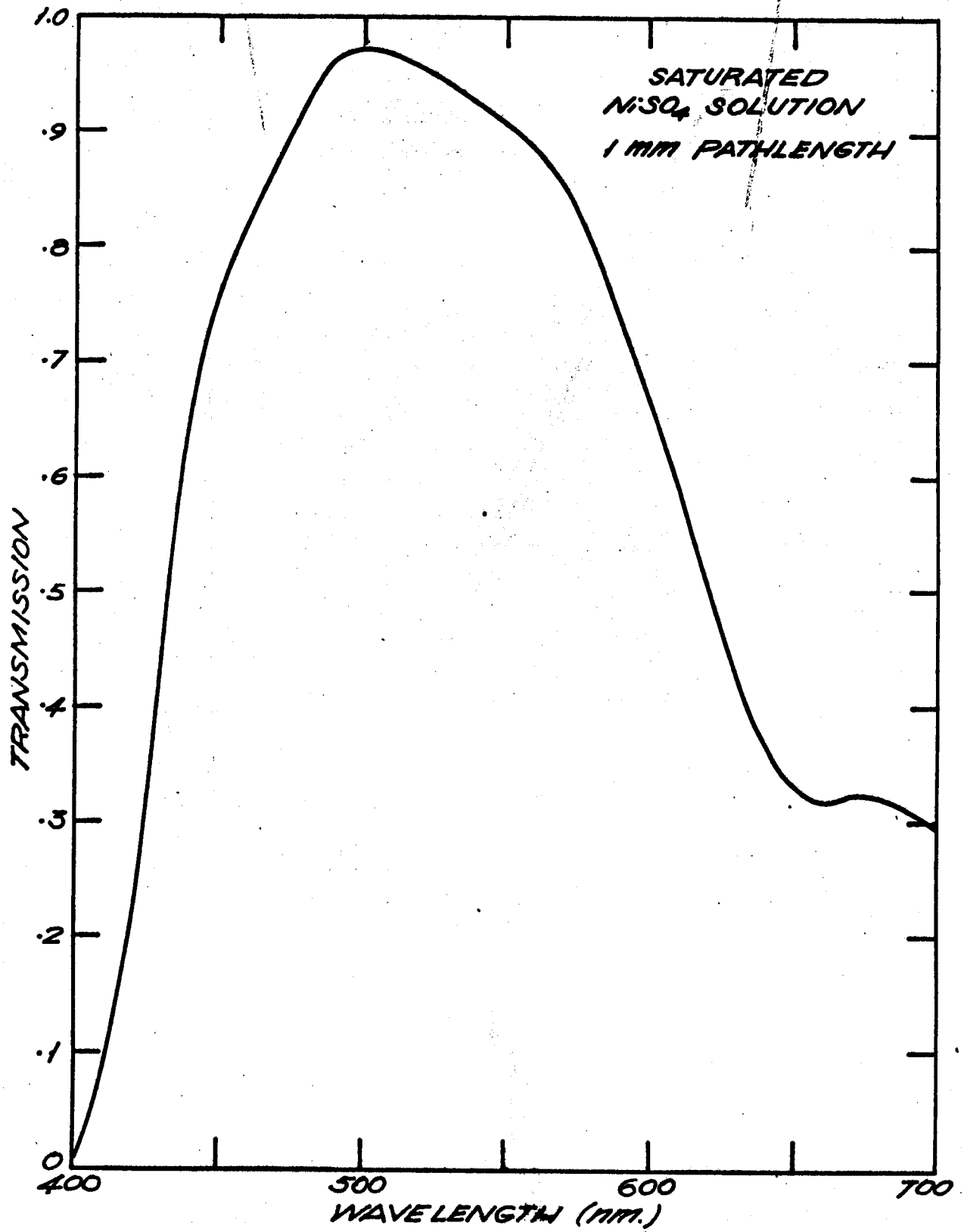

FIG (B.3) TRANSMISSION vs WAVELENGTH ; $NiSO_4$ SOL^n

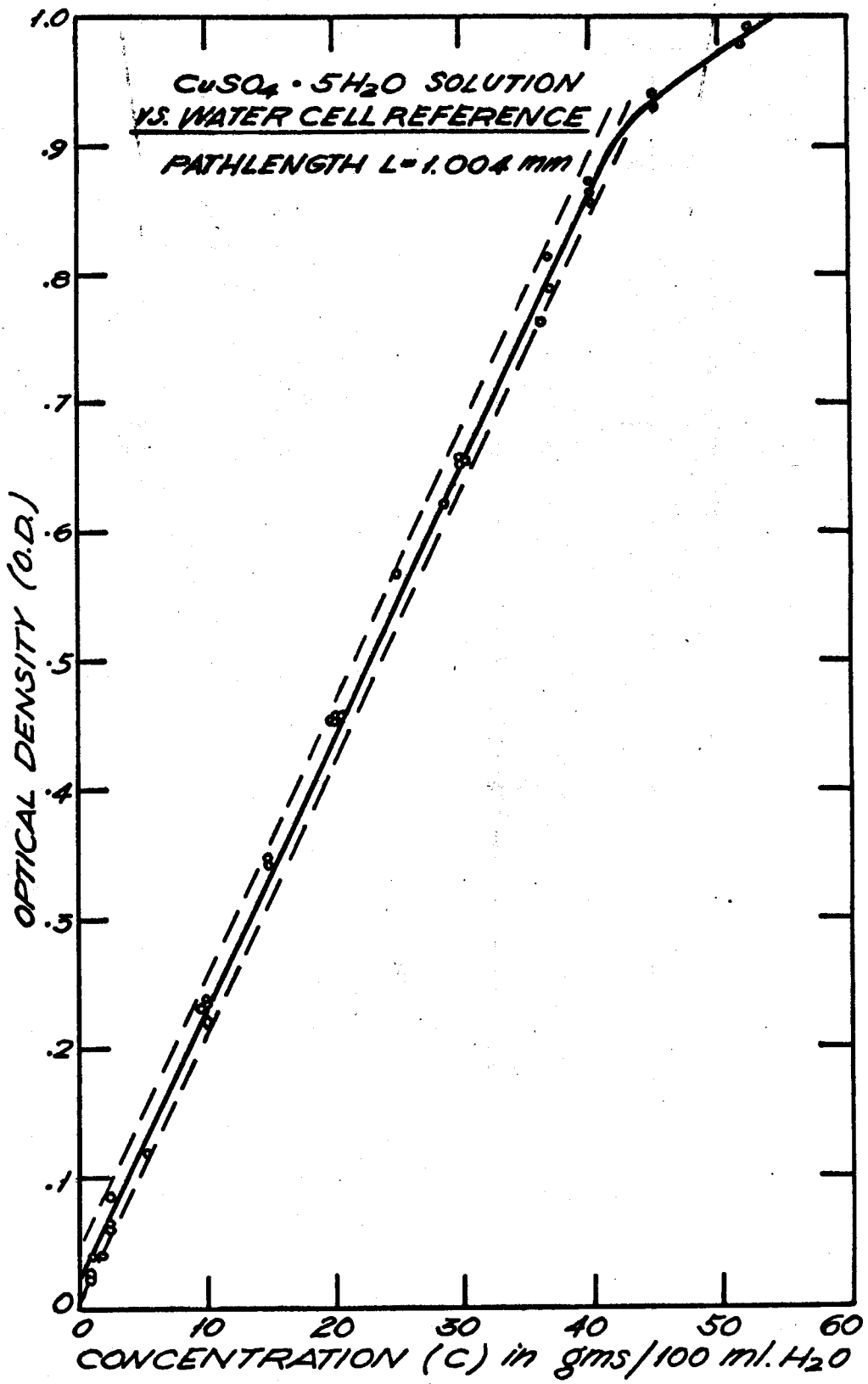

FIG (B.4) OPTICAL DENSITY VS CONCENTRATION OF $CuSO_4$ SOLUTIONS AT 694.3 nm.

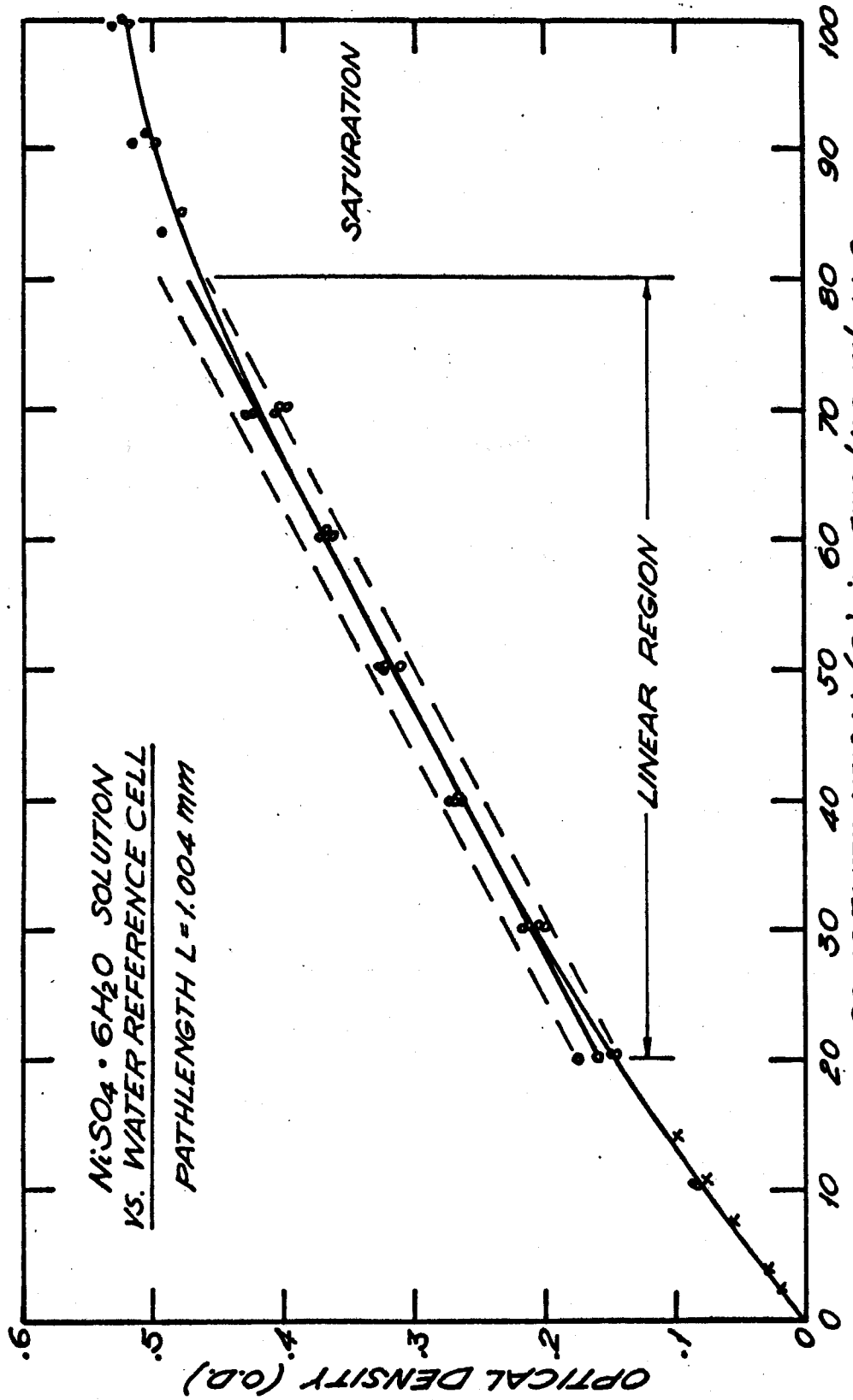

FIG (8.5) OPTICAL DENSITY VS CONCENTRATION OF $NiSO_4$ SOLUTIONS AT 694.3 nm.

$(n_1 - n_2)$ - see Eqs. (B-4) and (B-2) - or a failure of Beers Law in this solution at low concentrations. The author suggests the former is the cause of the discrepancy. For this $NiSO_4$ data two least squares fits were calculated, one for the linear region between the vertical dashed lines and the other including all the data with concentrations less than C = 80 gms/100ml

$$O.D._{Ni} = 0.0631 + 0.00497CL \quad ; \quad S_{yx} = 0.0103 \tag{B-9}$$

$$O.D._{Ni} = 0.0366 + 0.00530CL \quad ; \quad S_{yx} = 0.0185$$

where the first equation corresponds to the linear region only. In all three of the experimentally determined equations L is the pathlength in mm and C is the concentration in grms of $CuSO_4 \cdot 5H_2O$ (or $NiSO_4 \cdot 6H_2O$) per 100 ml of water.

B-4 Discussion

Assuming Beers Law is valid for all concentrations below the saturation concentration, the optical density vs. concentration should be defined by Eq. (B-6) i.e.

$$O.D = 0.0304 + 0.4342\alpha_2 L$$

where the slope, m, of the experimentally determined straight lines is related to the above equation through the relation

$$0.4342\alpha_2 L = mC$$

where α_2 has the dimensions of cm^{-1}, if L is measured in cm.

Most data was recorded with a reference cell containing distilled water which should eliminate the first term in Eq. (B-6) i.e. intercept passes through O.D. = 0. The intercept in the $CuSO_4$ data agreed with the theoretical value of zero within the experimental error. The intercept with the $NiSO_4$ data is larger than can be justifiably attributed to experimental error so that several points with low concentrations ($c < 10$ grms/100ml) were measured and are plotted as x's in Fig. (B-5). It should be noted that these points approach zero in a nonlinear way. We attribute this nonlinear behaviour to the non-constancy of $(n_2 - n_1)$ and its effect on R_2 which was neglected in Eq. (B-6).

To check the validity of Eq. (B-6) the water filled reference cell was removed and the data retaken. It was found that the slope of the lines was unaffected as expected. The O.D. of the $CuSO_4$ data increased by O.D. = 0.031 in close agreement with Eq. (B-6) while the $NiSO_4$ data increased by O.D. = 0.039.

The calibrations discussed above all pertain to the low light intensity measurements performed on the Cary 14 spectrometer. A final test of the liquid attenuators was performed using the high intensity ($120MW/cm^2$) light beam delivered by the Q-switched laser. Two methods of testing were used. (1) The O.D. of the liquid attenuators in 1cm pathlength cells was adjusted to have the same value as the Jena glass attenuators calibrated independently by the manufacturer. The signals received by two calibrated photodiodes, one preceded by the glass

attenuator and the other preceded by the liquid attenuator, were measured. A second measurement was made with the liquid and glass attenuators interchanged. Agreement within ±5% occurred for optical densities in the range $0.3 \leq$ O.D. < 6. Below O.D.= 0.3 the liquid attenuators yielded slightly larger signals (~ 20% larger) than their glass counterparts. (2) A series of 1cm pathlength cells with O.D.'s in the range from 0.3 to 6 were stacked in series in front of a calibrated photodiode. The Q-switched laser operating with constant amplitude (±5%) was fired at the stack of cells. The number of cells used and the order in which they were stacked was varied while keeping the overall O.D. the same for each laser firing. Once again, no variations in the detected signals was measureable.

From the results of these high intensity measurements we conclude that the liquid attenuators scale linearly with concentration and/or pathlength in the range $0.3 \leq$ O.D. < 6 for incident laser power densities up to 120MW/cm^2 and possibly higher.

Finally we note that the calibrations and calculations in this appendix assume light beams at normal incidence to the cell. In stacking cells in series they are tipped slightly to avoid interference effects. The question remains; how does tipping the cell effect the path length L? It is easily shown, from Snell's law, that if L_0 is the pathlength at normal incidence, θ the angle of incidence and n_2 the index of refraction

of the liquid the pathlength will be increased from L_0 to

$$L = L_0 \left(1 - \frac{\sin^2\theta}{n_2^2}\right)^{-1/2} \simeq L_0 \left[1 + \frac{1}{2}\left(\frac{\theta}{n_2}\right)^2\right]$$

where we have neglected the effects of the cell windows as in Eq. (B-6). Even for angles of incidence as large as 30°, the increase in pathlength is less than 8%. For the usual angle of less than 10°, the pathlength increase is less than 1%. Thus errors due to tipping the cell can be neglected.

Large errors occur for solutions close to the saturated solution concentration. This was to be expected due to the known failure of Beer's law with very concentrated solution and the sensitive dependence of saturation concentration on temperature. Crystals appeared in saturated solutions when they were cooled by as little as 2° C. Thus solution concentrations should be kept well below the saturation values.

APPENDIX C

CALIBRATION OF PHOTODETECTORS

C-1 Phototubes

Several types of phototubes were used as detectors of ruby laser radiation and the plasma radiation. Five phototubes in common use in this laboratory are listed in Table C-1, together with typical characteristics[90]. Monochromatic responsivity vs. wavelength[90] is plotted in Fig. C-1 for the photocathodes discussed here. Included on this figure is the responsivity of a silicon pin diode (dashed curve). The vertical scale and quantum efficiency (i.e. electrons/photon) should by multiplied by 10 for this curve.

The RCA 925[91] vacuum photodiode was commonly used as a monitor of Q-switched ruby radiation. When used in conjunction with a reasonably fast oscilloscope, rise times were limited by the oscilloscope (~ 4 nsec for Tektronix 585, 12 nsec for Tektronix 555) and not the diode. When biased at 1600 vdc, this diode can deliver currents sufficient to drive TWT oscilloscopes such as the Tektronix 519 with rise times in this case governed primarily by the transit time spreading (TTS) caused by the focusing effects[92,93] of the diode cylindrical geometry.

The so-called biplanar vacuum photodiode[94] is capable of delivering currents from 5×10^{-7} to 5 amps with a deviation

PHOTOTUBE AND CATHODE	PEAK MONCHROMATIC RESPONSIVITY (A/W)	BIAS VOLTAGE (Volts D.C.)	PEAK PULSED CURRENT (AMPS)	CAPACITANCE (pf)
RCA 925 (S-1)	0.0024	1000	0.10	1.6
RCA 929 (S-4)	0.042	1000	0.10	2.6
ITT F4000 (S-1)	0.0011	2500	3.00	1.0
EMI 6256B (S-11)	0.048	1550	.50	10.0
HPA 4205 (Silicon)	0.7	-20	.01	<1

TABLE (C-1) - CHARACTERISTICS OF PHOTODETECTORS

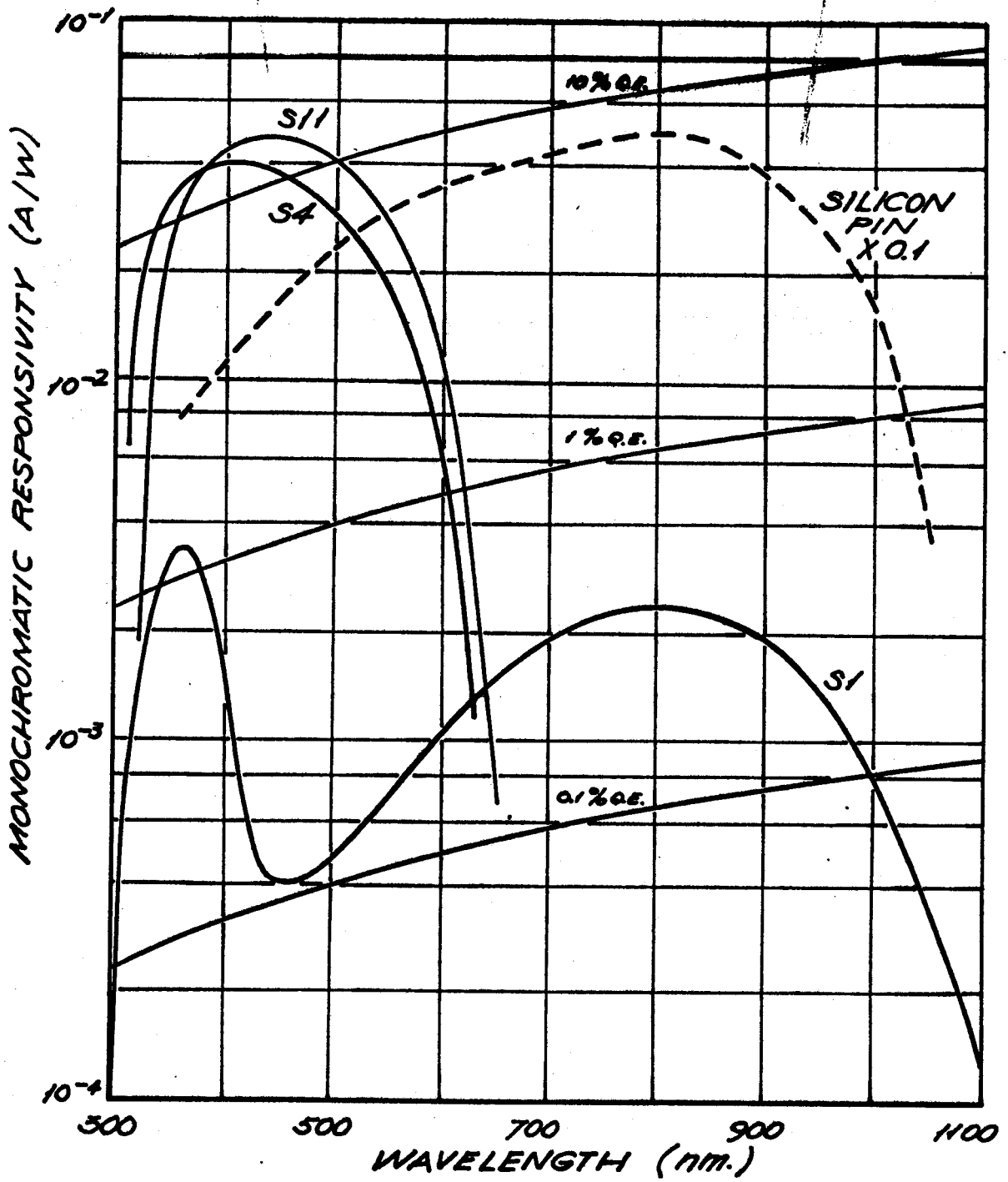

FIG (C.1) RESPONSIVITY OF PHOTOCATHODES.

from direct proportionality between current output and light input of less than 10%[95]. When the biplaner-diode was mounted in a high-frequency coaxial mounting[94,96] and properly terminated into a coaxially mounted 50 ohm load, a rise time of less than 0.5 nsec was attainable.

Solid state devices such as the HPA 4205 pin diode[97] listed in Table (C-1) have the advantages of small size (.061 inches diameter), low bias requirements (-20Vdc), extremely high quantum efficiencies (0.75 electrons/photon or 0.5A/W), wide spectral range, (400 to 1000nm) and rise times of less than 1 nanosecond. Their main disadvantage is that the peak pulsed current is limited to about 10 mA for pulse durations less than 100 nsec. This current limitation can be overcome by using a large area diode at some sacrifice to rise time.

Finally photomultipliers (PM) are capable of high pulsed currents of short duration, but suffer from rise times of typically 0.5 nsec[98] per stage. For the EMI 6256B in Table (C-1) with 13 stages the rise-time was approximately 7 nsecs in close agreement with this prediction.

In this appendix we discuss the calibration procedures used and the measured linear operating ranges of the phototubes. The discussion to follow relates primarily to the cylindrical 925 and biplanar F4000 phototubes.

C-2 Calibration Procedure

The diodes were calibrated using an Electro Optics Associates (EOA) model L-101 spectral source. This spectral irradiance standard was a quartz-iodine lamp operating at a colour temperature of 3050°K when 6.500 Amps were delivered to the lamp from a precision EOA model P-101 current supply. The use of this lamp as a spectral irradiance standard is discussed in detail by Stair et al.[99]. Both the lamp and current supply are directly traceable to NBS secondary standards. The manufacturer claims ±5% accuracy for the calibration curve of the lamp, provided it has been in use for less than 100 hours. The lamp used in the calibrations below was approximately 35 hours old. In the visible region of the spectrum the calibration curve is inaccurate due to the coarse wavelength scale and the rapidly changing irradiance of the source as a function of wavelength. However, in those regions of the calibration curve where accurate readings were possible (λ > 1500nm and three points between 250 and 500nm) it was found that our lamp agreed with Stair's lamp QL-10 within 2%[99]. Thus, Stair's accurate results in the range $350 < \lambda < 1000$nm were used to improve our calibration accuracy. If the calibrations determined from this "improved" curve are seriously questioned, the number of significant figures in the final result can always be reduced to agree with the accuracy of the manufacturers calibration curve. (For example, at the ruby emission wavelength, 694 nm, the EOA curve yields the irradiance 6.2 ± 0.2 $\mu w/cm^2$-nm

at 40 cm while from Stairs results we find 6.33 ± .12 $\mu w/cm^2$-nm).

The current delivered by the diode under calibration was measured with a Keithley model 153 nanoampere meter which was calibrated using a Keithley model 261 Picoampere Calibration unit. This allowed currents to be read with ±1% accuracy of full scale.

The spectral irradiance standard is calibrated for a lamp-to-cathode distance, d, of 40 cm. This distance could be measured to within ±1mm and we calculate the error due to distance measurements using

$$\frac{I_1}{I_2} = \left(\frac{d_2}{d_1}\right)^2 = \left(\frac{40 \pm \Delta}{40}\right)^2 = \left(1 \pm \frac{\Delta}{40}\right)^2$$

which with $\Delta = \pm$ 1mm yields

$$\frac{I_1}{I_2} \simeq 1 \pm \frac{2\Delta}{40} = 1 \pm \frac{1}{200}$$

The error introduced due to uncertainties in d is ±0.5%.

With planar photocathodes (F4000 diode and 6256B PM) this distance accuracy was easily obtained. With semi-cylindrical diodes (925 and 929 diodes) the distance to the photocathode varies across the cylindrical cathode. The 925 has a typical cathode radius of 8mm; thus if we measure the lamp-to-cathode distance midway between the anode and the extreme point of the cathode we set $\Delta = \pm$ 4mm and the distance error in this case

was ± 2%.

C-3 Laser Detector Calibration

The 925 diodes were calibrated with a spike filter preceding the photocathode with the following properties: 1) aperture of filter = 2.54 cm diameter 2) peak transmission at 694.3 nm was 0.72 3) passband, FWHM was 3.0 nm. Thus the responsivity of the detector was given by

$$K_L = \frac{I_L}{A \int J(\lambda) F(\lambda) d\lambda} \qquad \frac{\text{Amps}}{\text{Watt}} \qquad \text{(C-1)}$$

where I_L was the detector output (Amps), $J(\lambda)$ was the standard lamp irradiance (Watts/cm^2-nm at 40cm), $F(\lambda)$ was the filter transmittance normalized to unity, and A the area of the receiving aperture. It was found that a numerical integration of $\int J(\lambda)F(\lambda)d\lambda$ using the calibration curves of the standard lamp and the filter yielded a result which agreed within ~2% with the result obtained when approximating the integral by

$$\int J(\lambda)F(\lambda)d\lambda = J(\lambda_L) \cdot T(\lambda_L) \cdot \Delta\lambda$$

where $J(\lambda_L)$ is the irradiance of the lamp at the laser wavelength λ_L, $T(\lambda_L)$ is the peak transmittance at λ_L and $\Delta\lambda$ is the FWHM of the spike filter in nanometers. Thus,

$$K_L = \frac{I_L}{A \cdot J(\lambda_L) \cdot T(\lambda_L) \cdot \Delta\lambda} \qquad \frac{\text{Amps}}{\text{Watt}} \qquad \text{(C-2)}$$

For 9 diodes (S1 cathode) calibrated using the procedures described above, it was found that K_L varied from 0.741×10^{-3} to 2.03×10^{-3} A/W. The mean value of K_L was $\overline{K}_L = 1.54 \times 10^{-3}$ A/W in close agreement with the published average value of 1.68×10^{-3} A/W. All but two diodes were clustered in the range $1.3 < K_L < 1.6 \times 10^{-3}$ A/W. The measured values of K_L remained essentially constant for bias voltages ranging from 250V to 1100V. An independent check of our calibration procedure was available from the calibration ticket provided by the manufacturer of our biplanar photodiode. The manufacturer's calibration ticket listed $K_L = 0.766 \times 10^{-3}$ A/W at 694.3 n, while our calibration yielded $K_L = 0.74 \times 10^{-3}$ A/W, i.e. agreement within $\sim$ 4%.

C-4 Photomultiplier Calibration

Photomultipliers (PM's) are usually calibrated in combination with a spectrometer. The 6256B PM used in this study was preceded by either narrow bandwidth interference filters (spike filter) or a Jarrell-Ash 0.25 meter Ebert Type spectrometer with 0.5nm resolution. The spectrometer - PM combination requires the addition of a suitable filter preceding the entrance slit to ensure that only a single spectrum order is detected. The responsivity of the filter, spectrometer, PM combination is given by

$$K_R = \frac{I_R A_R}{l w \int J(\lambda) T(\lambda) d\lambda} \quad \frac{\text{Amps}}{\text{Watt}} \qquad (C\text{-}3)$$

where I_R is the detector output (Amps), $J(\lambda)$ is the irradiance of the standard lamp, $T(\lambda)$ is the transmission of the filter and spectrometer in series, ℓ and w are length and width respectively of the entrance slit of the spectrometer and A_R is an added attenuator at the spectrometer entrance slit to prevent saturation of the PM (A_R is typically a neutral density filter with $A_R \leq 10^3$). The response, S_R(Amps), of the spectrometer - PM detector to a radiant source with wavelength power distribution $P(\lambda)$ (Watts/cm^2-nm) is

$$S_R = K_R \ell w \int P(\lambda) T(\lambda) d\lambda \quad \text{Amp.} \qquad (C\text{-}4).$$

provided the filter-spectrometer combination are the same as those used to determine K_R. Therefore the scattered power distribution is given by

$$\int P(\lambda) T(\lambda) d\lambda = \frac{S_R}{I_R A_R} \int J(\lambda) T(\lambda) d\lambda \qquad (C\text{-}5)$$

This equation can be greatly simplified if $J(\lambda)$ and $P(\lambda)$ are smoothly varying, continuous functions of wavelength. The standard lamp varies smoothly, and if we assume $P(\lambda)$ also varies smoothly then since the bandwidth of the spectrometer is only 0.5nm, we can consider both $J(\lambda)$ and $P(\lambda)$ to be constant at the wavelength λ_1 of interest and hence

$$P(\lambda_1) \int T(\lambda) d\lambda = \frac{S_R}{I_R A_R} J(\lambda_1) \int T(\lambda) d\lambda$$

or
$$P(\lambda_1) = \frac{S_R}{I_R A_R} J(\lambda_1) \qquad \text{(C-6)}$$

When calibrating our Jarrel-Ash 0.25 meter spectrometer in conjunction with our 6256B PM it was found that the gain of the PM was sufficient when biased at 1000 vdc to yield measureable voltages across the 50 ohm resistor used in the pulsed light emission measurements of chapter 5 of this thesis. Using the Keithley Model 153 nanoamper-microvolt meter, measureable calibration voltages with the same 50Ω load were possible. Thus (C-6) was recast into the form

$$P(\lambda_1) = \frac{V_p}{V_c} \frac{J(\lambda_1)}{A_R} \qquad \text{Watts}/\text{cm}^2\text{-nm} \qquad \text{(C-7)}$$

where V_p = pulsed signal to be measured and V_c = the calibration voltage. Further $A_R = 1$ for bias voltages $\leq$ 1000V for the system described above. The value of $P(\lambda_1)$ calculated from Eq. (C-7) is the irradiance at the input slit to the spectrometer.

C-5 Linearity

Ideally, a photodetector should indicate a direct proportionality between current output and light flux input, if the photocathode is uniformly illuminated. That is, the current I(t) should be related to the light flux L(t) through the equation

$$I(t) = K_L L(t) \qquad \text{(C-8)}$$

where K_L is the monochromatic responsitivity in Amperes/Watt (See Eq. (C-1), $K_L \sim 1.5 \times 10^{-3}$ A/W for 925 diodes at 694.3 nm). The linearity predicted by Eq. (C-8) was checked using a General Radio Type 1538A Stroboscope which delivered a light pulse with 1.3 microsec duration (FWHM) and roughly triangular shape. A pulse rate of 2 flashes per second was used for the measurements reported here. The bias curcuit used with cylindrical 925 diodes is shown in Fig. (C-2). The GR874-K coaxial capacitors provided a high frequency, low impedance current source. The current pulse delivered by the diode to the Tektronix 50 ohm coaxial resistor with 100 MHz bandwidth was displayed on a Tektronix 555 oscilloscope.

We approximate the light pulse time dependence by the expression

$$L(t) = L_p \sin^2 \frac{\pi}{2\delta} t \qquad 0 \le t \le \delta \qquad \text{(C-9)}$$

where L_p is the peak intensity and δ is the full width at half-maximum (FWHM). A rough estimate of the maximum pulsed current the diode can deliver may be calculated by equating the d.c. rating of the phototube, I_{dc}, to the value of the pulsed current I(t) averaged over the period T, that is

$$I_{dc} \longrightarrow \frac{1}{T} \int_0^T I(t)\, dt \qquad \text{(C-10)}$$

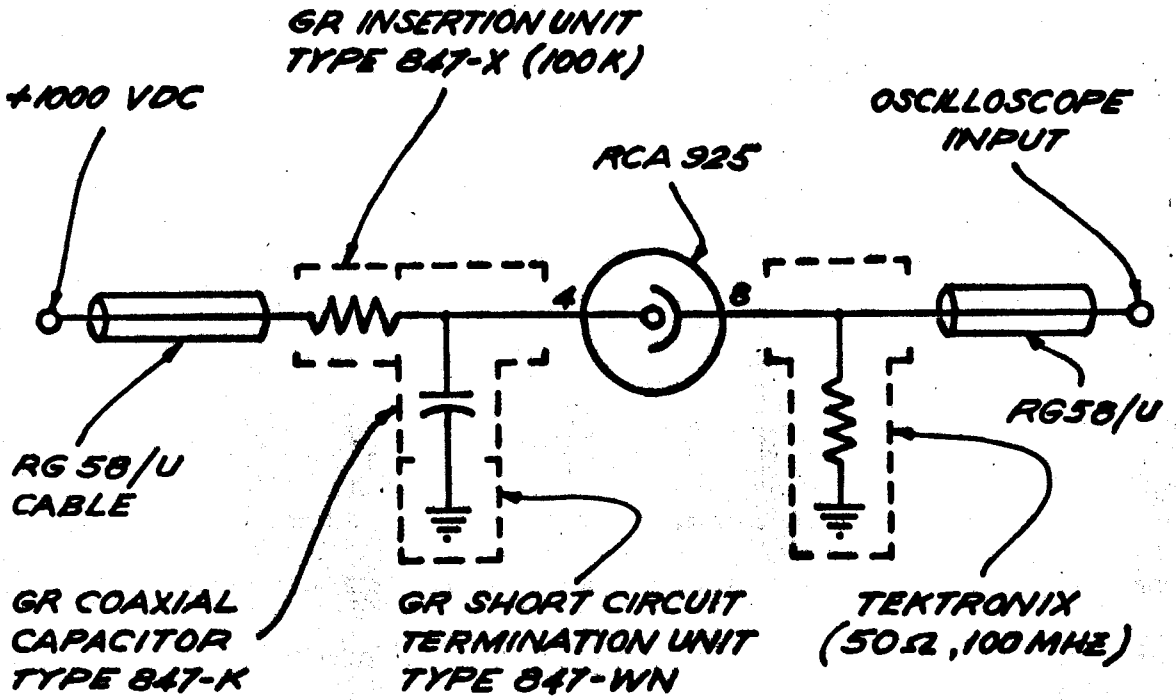

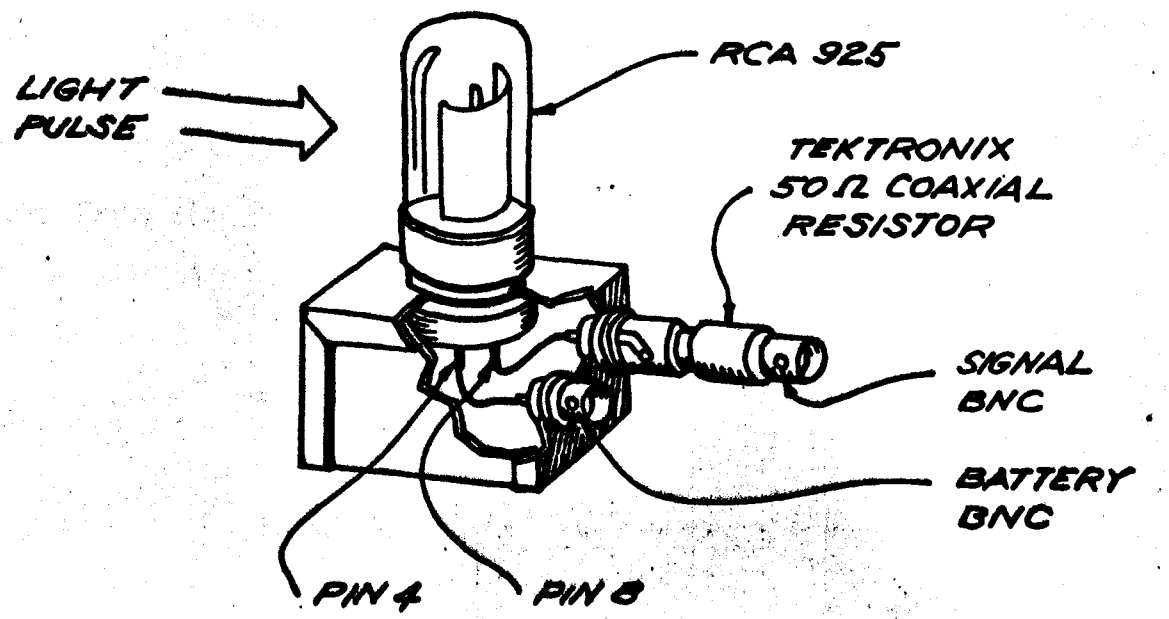

FIG (C.2) BIAS CIRCUIT FOR CYLINDRICAL PHOTODIODES.

Equation (C-10) states that the charge delivered by a d.c. current, I_{dc}, flowing for a time T, is equal to the charge delivered by the single pulse occurring in time T. Substituting (C-9) into (C-10) realizing $I(t) = K_L L(t)$ and solving for the peak current ($I_p = K_L L_p$) yields

$$I_p = I_{dc} \frac{T}{\delta} \tag{C-11}$$

Equation (C-11) must be used with caution since it predicts very high currents for large T/δ. Experimentally it was found that Eq. (C-11) was valid for $T/\delta < 10^6$ for S-1 and S-4 vacuum diode photocathodes. Using T = 1/2 and δ = 1.3 μsec together with the typical I_{dc} = 5 μ A.d.c. rating of vacuum phototubes we find $I_p \sim 1.92$ Amp. However, the diode current will often saturate due to space-charge current limiting before this value is reached. This space-charge limited current is calculate from the Child-Langmuir equations[92,100]

$$\left.\begin{aligned} I_b &= \frac{\sqrt{2}}{9}(4\epsilon_0)\sqrt{\frac{e}{m}}\frac{A}{d^2}V^{3/2} \\ &= 88.6\times10^{-6}\,V^{3/2} \quad \text{(Amp)} \end{aligned}\right\} \text{Biplanar} \tag{C-12}$$

$$\left.\begin{aligned} I_c &= \frac{\sqrt{2}}{9}(4\pi\epsilon_0)\sqrt{\frac{e}{m}}\frac{V^{3/2}}{(\beta^2 d^2)} \\ &= 19.6\times10^{-6}\,\frac{V^{3/2}}{\beta^2} \quad \text{(Amp)} \end{aligned}\right\} \text{Cylindrical} \tag{C-13}$$

where A = cathode area, d = cathode-anode distance, ℓ = anode length r_a = anode radius, V = bias voltage and β^2 is a factor

introduced by Langmuir[92] to account for focusing effects in cylindrical diodes. The numerical values apply to the F4000 biplanar diode and 925 cylindrical diodes used in this study, and $\overline{\beta}^2$ is an experimentally determined value of β^2.

The biplanar diode is usually biased at 2500 Vdc leading to a space charge limited current of 6 Amps. The manufacturer[94] claims a linear response up to one half this value, i.e. I_b = 3 Amp.

The cylindrical 925 diode (Fig. C-2) is recommended to be operated at 250V for dc applications[91] leading to $I_c\overline{\beta}^2$ = 77.5×10^{-3} Amp. We will show shortly that $\overline{\beta}^2 \approx 4$; thus I_c = 19.4×10^{-3} Amp. well above the d.c. rating of 5×10^{-6}A. It was determined experimentally that all 925 diodes could be biased at 1000Vdc and selected (low gas) diodes biased to 1600Vdc. Substituting V = 1600Vdc and assuming $\overline{\beta}^2 = 4$ in Eq. (C-13) yields I_c = 0.314 Amp. The superiority of the biplanar diode is evident.

The coaxially counted biplanar diode was found to respond linearly (±5%) for currents ranging from 10^{-4} Amp. (minimum detectable level) to 1.5 Amps using the Strobe flash described above. Using the ruby laser as the pulsed light source this diode responded linearly to greater than 3 Amps (voltage signals > 375 volt using a 125 ohm load!). The bias voltage was fixed at 2500Vdc.

Prior to measuring the linearity of the cylindrical 925 phototubes, they were checked for gas amplification by maintaining

a constant light flux sufficient to yield a d.c. photocurrent of 10^{-6} Amp and increasing the bias voltage while simultaneously measuring the tube current. Most phototubes indicated a linear, almost horizontal I-V characteristic for voltages less than 1100Vdc. Above this voltage, all but one of the nine tubes tested showed a sharp increase in current, characteristic of gas amplification. The remaining tube remained linear to 1600Vdc. The cylindrical diodes were checked for linear response to the pulsed Strobe flash light source at bias Voltages of 250, 500, 750 and 1000 Volts. The resulting diode current vs. the transmission of calibrated neutral density filters is plotted in Fig. (C-3). From these results and the known bias voltage, values of $\overline{\beta}^2$ were calculated from Eq. (C-12) and are included on the figure. The theoretical value of β^2 is critically dependent on the ratio r/r_a where r_a is the radius of the anode cylinder and r the radius to the space charge layer[92]. While the values of $\overline{\beta}^2$ varied from 4 (at 250 volts) to 8 (at 1600 volts) the ratio r/r_a only changes from 3.3 to 4.5[92]. The fact that β^2 changes with bias voltage is given only passing mention in the theoretical discussion of Langmuir and Blodgett[92]. The interested reader should consult this reference for further details.

When the Strobe flash was replaced with the Q-switched laser the 925 diodes saturated due to space-charge current limiting at essentially the same point shown in Fig. (C-3).

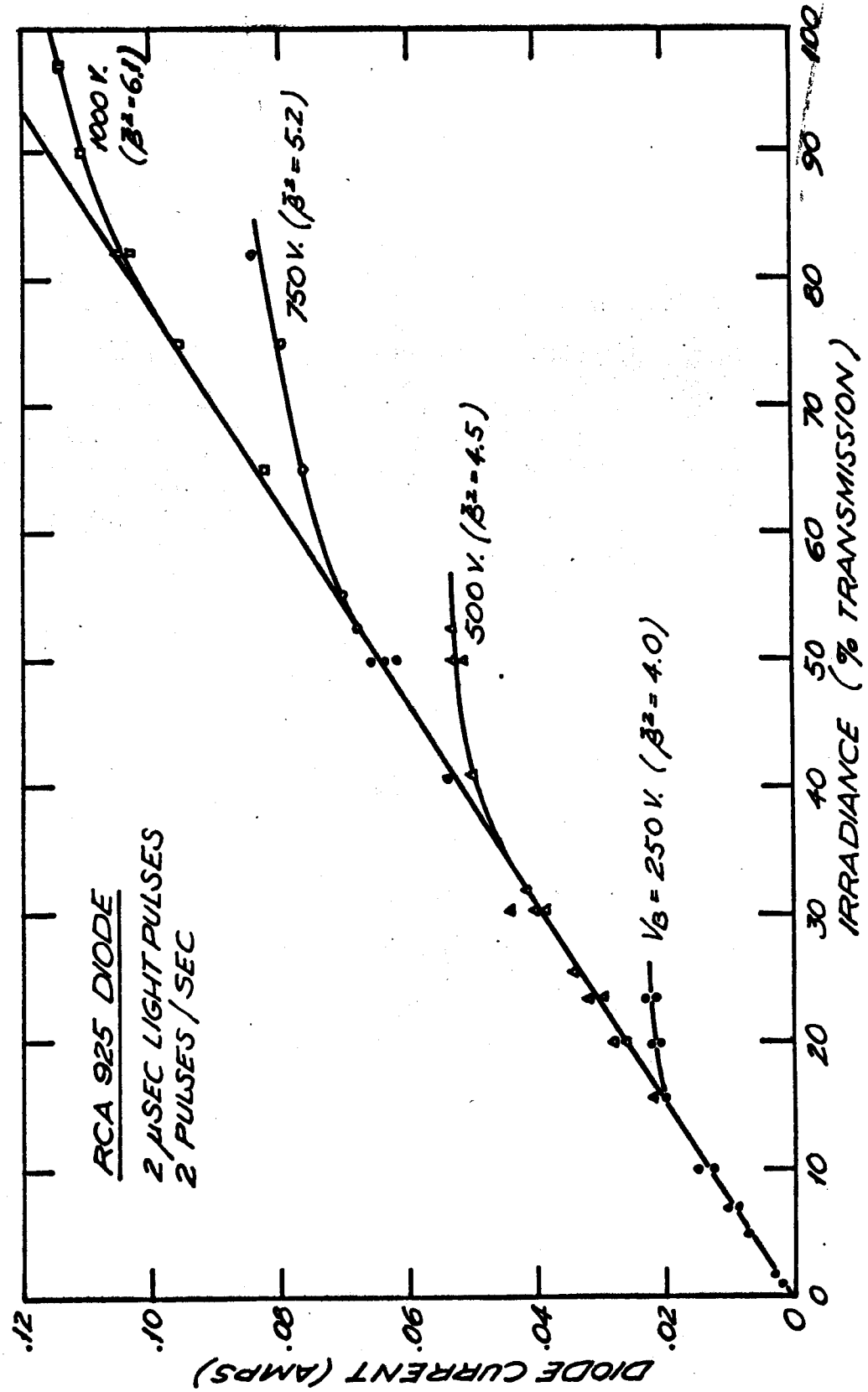

FIG (C.3) LINEAR RESPONSE OF CYLINDRICAL DIODES VS BIAS VOLTAGE.

C-6 Laser Beam Sampling

In most experiments, only a small fraction of the incident laser beam is "monitored" using a beam-splitter. The beam splitter is followed by suitable attenuators and filters as in Fig. 4-1 of chapter 4. Assuming the reflectivity of the beam-splitter to be R, then RP_L of the incident laser power P_L is directed toward the photodiode where it is attenuated by an amount A so that the power incident on the photocathode is RP_L/A. If the sensitivity of the cathode is K_L Amps/Watt and the load resistor is R_L ohms then the voltage across the coaxial resistor in Fig. (C-2) will be $V = (RP_L/A)K_LR_L$ so that the incident power is given by

$$P_L = \frac{AV}{RK_LR_LT(\lambda_L)} \quad \text{Watts} \qquad (C\text{-}14)$$

We have added a term $T(\lambda_L)$ in (C-14) to account for the transmission of an interference filter designed to pass the ruby wavelength.

The reflectivity of the beam splitter is a critical function of both the angle of incidence and the polarization of the incident laser beam. For example, at the usual 45° angle of incidence $R_\perp = 0.092$ for light polarized perpendicular to the plane of incidence while for the parallel case R reduces to $R_{11} = 0.008$ for a single surface of glass with index $n = 1.50$.

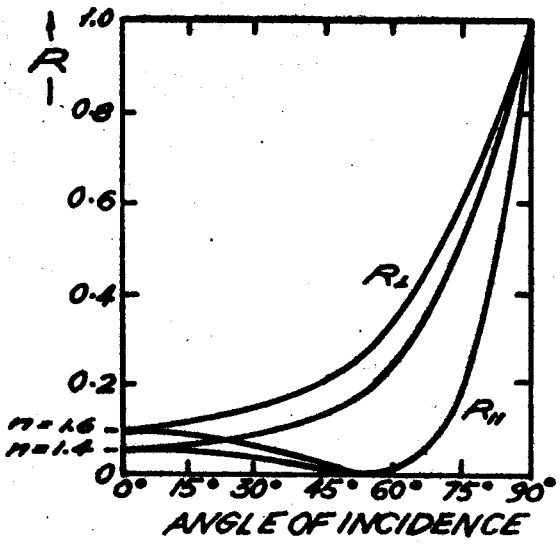

a) REFLECTIVITY OF GLASS SLIDE BEAM SPLITTER (AVERAGE OF BOTH SURFACES)

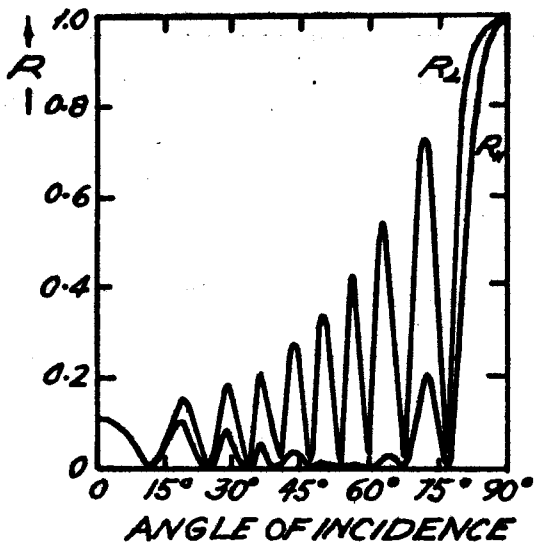

b) REFLECTIVITY OF PELLICLE BEAM SPLITTER
$n=1.49$, $\lambda=693.4$ nm., PELLICLE THICKNESS $=8\mu$

FIG (C.4) REFLECTIVITY vs ANGLE OF INCIDENCE FOR GLASS SLIDE AND PELLICLE BEAM SPLITTERS (AFTER HILLENKAMP[49]).

Two types of beam splitters were used: (1) simple glass microscope slides approximately 1mm thick and (2) pellicles of collodion membranes, approximately 8 microns thick, stretched over a suitable frame. The reflectivity of these two forms of beam-splitter is shown in Fig. (C-4) which is taken from the work of Hillenkamp[49]. Note the rapidly changing reflectivity near 45° for the pellicle beam splitter. The reflectivity changes from approximately $R_{\perp} = 0.3$ to $R_{\perp} = 0$ in less than 5° for the ruby laser light polarized perpendicular to the plane of incidence. Measured reflectivities of both the pellicle and the glass slide using a He-Ne laser confirmed these results.

Glass slides yielded $R_{\perp} = 0.20$ for plane polarized light and $R_{o} = 0.10$ for circularly polarized light. The pellicles yielded $R_{\perp} \cong 0.08$ and $R_{o} = \cong 0.04$. Hillenkamp[49] points out that particularly in the case of pellicle beam splitters, the reflectivity is also affected significantly by the divergence of the laser beam. For most of the experiments performed in this thesis, glass slides were used as beam splitters.

REFERENCES

1. P. D. Maker, R. W. Terhune and C. M. Savage, Proc. Third International Quantum Electronics Conference, Paris (1963), P. Grivet and N. Bloembergen, Eds., Columbia University Press (1964).

2. Yu. P. Raizer, Soviet Physics Uspekhi 8, 650 (1966).

3. A. Gold and H. B. Bebb, Phys. Rev. Letters, 14, 60 (1965).

4. H. B. Bebb and A. Gold, Phys. Rev., 143, 1 (1966).

5. R. G. Meyerand, Jr., and A. F. Haught, Phys. Rev. Letters 13, 7 (1964).

6. J. K. Wright, Proc. Phys. Soc., 84, 41 (1964).

7. P. F. Browne, Proc. Roy. Soc., 86, 1323 (1965).

8. B. A. Tozer, Phys. Rev., A137, 1665 (1965).

9. V. V. Korobkin and A. J. Alcock, Phys. Rev. Letts., 21 1433 (1968).
A. J. Alcock, C. DeMichelis, V. V. Korobkin and M. C. Richardson, Appl. Phys. Letters, 14, 145 (1969).

10. A. J. Alcock and M. C. Richardson, Phys. Rev. Letters, 21, 667 (1968).

11. M. Hercher, J. Opt. Soc. Am., 54, 563A (1964).

12. R. A. Miller and N. F. Borrelli, Appl. Optics, 6, 165 (1967).

13. B. S. Sharma, Laser Induced Dielectric Breakdown and Mechanical Damage in Silicate Glasses, Ph.D. Thesis, Simon Fraser University (1968). Unpublished.

14. B. S. Sharma and K. E. Rieckhoff, Can. J. Phys. 45, 3781 (1967).

15. R. G. Brewer and K. E. Rieckhoff, Phys. Rev. Letters, 13, 334 (1964).

16. C. E. Bell and J. A. Landt, Appl. Phys. Letters 10, 46 (1967).

17. E. F. Carome, C. E. Moeller, and N. A. Clark, J.A.S.A., 40, 1462 (1966).

18. E. F. Carome, E. M. Carreira and C. J. Prochaska, Appl. Phys. Letters 11, 64 (1967).

19. P. A. Barnes and K. E. Rieckhoff, Appl. Phys. Letters, 13 282 (1968).

20. J. D. Craggs and H. S. W. Massey, Handbuch der Physik, Band XXXVII/1, pp. 314-415, Springer-Verlag Berlin (1959).

21. H. Kogelnik and T. Li, Appl. Opt., 5, 1550 (1966).

22. A. G. Fox and T. Li, Bell. Sys. Tech. J., 40, 453 (1961).

23. G. D. Boyd and H. Kogelnik, Bell. Sys. Tech. J., 41, 1347 (1962).

24. M. Hercher, Appl. Phys. Letters, 7, 39 (1965).

25. J. E. Bjorkholm and R. H. Stolen, J. Appl. Phys., 39 4043 (1968)..

26. D. P. Bortfeld, R. S. Congleton, M. Geller, R. S. McComas, L. D. Riley, W. R. Sooy, M. L. Stitch, J. Appl. Phys. 35, 2267 (1964).

27. G. Lampis, C. A. Sacchi, O. Svelto, Appl. Opt., 3, 1467 (1964)..

28. W. R. Sooy, Appl. Phys. Letters, 7, 36 (1965).

29. F. J. McClung and D. Weiner, IEEE J. Quant. Electron, QE-1, 94 (1965).

30. M. Born and E. Wolf, Principles of Optics Third Ed. Pergamon Press, New York; 1964.

31. J. K. Watts, Appl. Opt., 7, 1621 (1968).

32. L. Rothrock and R. E. Wilder J. Appl. Phys., 39, 1918 (1968)..

33. T. G. Bergman and J. L. Thompson, Appl. Opt. 7, 923 (1968).

34. R. W. Waynant, J. H. Cullon, I. T. Basil, G. D. Baldwin, Appl. Opt., 4, 1648 (1965).

35. R. Y. Chiao, E. Garmire, and C. H. Townes, Phys. Rev. Letts., 13, 479 (1964).

36. P. A. Barnes and K. E. Rieckhoff, Bull. Am. Phys. Soc., 11, 898 (1966).

37. M. W. Dowley, K. B. Eisenthal, and W. L. Peticolas, Phys. Rev. Letts., 18, 531 (1967).

38. M. W. Dowley, W. L. Peticolas, I.B.M. Journal of Research and Development, 12, 188 (1968).

39. C. David, P. V. Avizonis, H. Weichel, C. Bruce, and K. K. Pyatt, IEEE J. Quant. Elec., QE-2, 493 (1966).

40. W. J. Fader, Phys. Fluids, 11, 2200 (1968).

41. R. V. Churchill, Operational Mathematics. McGraw-Hill Book Co., Toronto (1958).

42. Constants taken from, American Institute of Physics Handbook. Second Ed., D. E. Gray, Editor, McGraw-Hill Book Co., Inc., Toronto (1963).

43. M. Young, The Dynamics of Laser Induced Breakdown in Gases. Ph.D. Thesis, University of Rochester, Rochester, N.Y. (1968).

44. Th. Peters, Zeits, für Physik 135, 573 (1953).

45. P. A. Apanasevich and V. S. Aizenshtadt, Tables for the Energy and Photon Distribution in Equilibrium Radiation Spectra, The MacMillan Co., New York (1965).

46. R. W. Minck, J. Appl. Phys., 35, 252 (1964).

47. L. R. Evans and C. Grey Morgan, Phys. Rev. Letters, 22, 1099 (1969).

48. E. Garmire and C. H. Townes, Appl. Phys. Letters, 5, 84 (1964).

49. F. Hillenkamp, Appl. Optics, 8, 351 (1969).

50. M. J. Lubin and W. Leising, Rev. Sci. Instr., 38, 1157 (1967).

51. H. M. Musal, Jr., Proc. IEEE, 57, 98 (1969).

52. A. E. Siegman, An Introduction to Lasers and Masers, McGraw-Hill Book Co., Inc. (1968) - see ref. 51.

53. F. A. Jenkins and H. E. White, Fundamentals of Optics. Third Ed., McGraw-Hill Book Co., Inc. (1957).

54. M. Young, M. Hercher, and Chung-Yiu Wu, J. Appl. Phys., 37, 4938 (1966).

55. G. Benedek and T. Greytak, Proc. IEEE., 53, 1623 (1965).

56. V. V. Korobkin, S. L. Mandel'shtam, P. P. Pashinin, A. V. Prokhindeev, A. M. Prokhorov, N. K. Sudhodrev, M. Ya. Shchelev, Soviet Physics JETP, 26, 79 (1968).

57. N. G. Basov, V. A. Boiko, O. N. Krokhin, and G. V. Sklizkov, Soviet Phys. - Doklady, 12, 248 (1967).

58. L. R. Evans and C. Grey Morgan, Nature, 219, 712 (1968).

59. T. A. Wiggins, R. V. Wick, N. D. Foltz, C. W. Cho, D. H. Rank, J. Opt. Soc. Am., 57, 661 (1967).

60. M. Maier, W. Rother, and W. Kaiser, Phys. Letters, 23, 83 (1966).

61. G. M. Zverev and A. D. Martynov, Soviet Physics JETP Letters, 6, 351 (1967).

62. V. V. Korobkin and R. V. Serov, Soviet Physics JETP Letters, 6, 135 (1967).

63. T. Peters, Z. Physik, 135, 573 (1953).

64. M. H. Rice and J. M. Walsh, J. Chem. Phys., 26, 824 (1967).

65. E. A. Martin, The Underwater Spark: An Example of Gaseous Conduction at about 10,000 Atmospheres, Ph.D. Dissertation University of Michigan (1956).

66. J. W. T. Walsh, Photometry, Dover Publications, Inc., N.Y. (1965).

67. D. W. Gregg and S. J. Thomas, J. Appl. Phys. 38, 1729 (1967).

68. H. J. Kunze "The Laser as a Tool for Plasma Diagnostics", in Plasma Diagnostics, W. Lochte - Holtgreven, Editor North Holland Publishing Co., Amsterdam (1968).

69. E. E. Salpeter, Phys. Rev., 120, 1528 (1960).

70. J. A. Fejer, Can. J. Phys., 38, 114 (1960).

71. J. A. Dougherty and D. T. Farley, Proc. Roy. Soc., A259, 79 (1960).

72. M. N. Rosenbluth and N. Rostoker, Phys. Fluids, 5, 776 (1962).

73. S. A. Ramsden and W. E. R. Davies, Phys. Rev. Letters, 13, 227 (1964).

74. L. Spitzer, Physics of Fully Ionized Gases, Second Ed., Interscience Pubs., N.Y. (1962).

75. G. I. Taylor, Proc. Roy. Soc., A201, 159 (1960).

76. Ya. B. Zel'dovich and Yu. P. Raizer, Physics of Shock Waves and High Temperature Hydrodynamic Phenomena, Vol. I, Academic Press, N.Y. (1966).

77. Ya. B. Zel'dovich, S. B. Kormer, M. V. Sinitsyn and K. B. Yushko, Soviet Phys. Doklady, 6, 94 (1961).

78. A. J. Alcock, C. DeMichelis and K. Hamal, Appl. Phys. Letters, 12, 148 (1968).

79. E. Panarella and P. Savic, Can J. Phys. 46, 183 (1968).

80. R. N. Keeler, G. H. Bloom, and A. C. Mitchel, Phys. Rev. Letters, 16, 852 (1966).

81. A. J. Alcock and S. A. Ramsden, Appl. Phys. Letters, 8, 187 (1966).

82. A. J. Alcock and M. C. Richardson, Phys. Rev. Letters, 21, 667 (1968).

83. J. R. Novak and M. W. Windsor, J. Chem. Phys., 47, 3075 (1967).

84. W. D. Gill, R. E. MacDonald, and D. B. Greene, Rev. Sci. Instr., 39, 1114 (1968).

85. A. Yariv, Quantum Electronics, John Wiley and Sons Inc., New York (1967).

86. W. K. H. Panofsky and M. Philips, Classical Electricity and Magnetism, 2nd Ed., Addison-Wesley Publishing Co., Inc., Reading, Mass. (1962).

87. G. D. Boyd and J. P. Gordon, Bell. Sys. Tech. J., 40, 489 (1961).

88. H. Kogelnik "Modes in Optical Resonators" Chapter Five in Lasers, A. K. Levine, Ed., M. Debber, Inc., New York (1966).

89. H. Kogelnik and T. Li, Appl. Opt. 5, 1550 (1966).

90. E. H. Eberhardt, ITT Industrial Labls, Tech. Note 100 (1967)..

91. RCA Technical Manual PT-60 Phototubes and Photocells. 1963.

92. I. Langmuir and K. B. Blodgett, Phys. Rev., 22, 347 (1923).

93. W. R. Ferris, Proc. I.R.E., 24, 82 (1936).

94. E. H. Eberhardt, ITT Industrial Labs., Application Note E7 (1966).

95. ITT Biplaner photodiode type F4000 data sheet (1968).

96. M. J. Lubin and W. Leising, Rev. Sci. Instr. 38, 1157 (1967)..

97. Hewlett-Packard Associates, #4205 PIN photodiode data sheet (1966).

98. J. Sharpe, EMI Electronics Ltd., Document Ref. No. CP 5475 (1964).

99. R. Stair, W. E. Snieder, J. K. Jackson, Appl. Optics, 2, 1151 (1963).

100. K. R. Spangenberg, Vacuum Tubes. McGraw-Hill Book Co., Inc. (1948) - Chapter 8.

101. N. Ahmad, B. C. Gale, and M. H. Key, J. Phys. B. (Atom and Molec. Phys.) 2, ser. 2, pp. 403 (1969).

102. D. J. Innes, A. L. Bloom, Spectra Physics Laser Bulletin No. 5., Spectra-Physics, Incorporated, Mountain View, California (1966).